GRI-97/0361
SAND 97-2731

HYDRAULIC FRACTURE IMAGING USING INCLINOMETERS AT M-SITE: FINITE-ELEMENT ANALYSES OF THE B-SANDSTONE EXPERIMENTS

TOPICAL REPORT

Prepared by
B. P. Engler and N. R. Warpinski

Sandia National Laboratories
MS 0705
Division 6116
P.O. Box 5800
Albuquerque, New Mexico 87185

Prepared for:
GAS RESEARCH INSTITUTE
Contract No. 5089-211-2059

GRI Project Manager
Steve Wolhart
Drilling and Completions Team

December 1997

REPORT DOCUMENTATION PAGE

Form Approved
OMB No. 0704-0188

1. AGENCY USE ONLY (*Leave blank)*	2. REPORT DATE	3. REPORT TYPE AND DATES COVERED
	December 1997	Topical Report, December 1997

4. TITLE AND SUBTITLE

HYDRAULIC FRACTURE IMAGING USING INCLINOMETERS AT M-SITE: FINITE-ELEMENT ANALYSES OF THE B-SANDSTONE EXPERIMENTS

5. FUNDING NUMBERS

GRI contract no.
5089-211-2059

6. AUTHOR(S)

B.P. Engler and N.R. Warpinski

7. PERFORMING ORGANIZATION NAME(S) AND ADDRESS(ES)

Sandia National Laboratories
MS 0705
P.O. Box 5800
Albuquerque, New Mexico 87185

8. PERFORMING ORGANIZATION REPORT NUMBER

SAND97-2731

9. SPONSORING/MONITORING AGENCY NAME(S) AND ADDRESS(ES)

Gas Research Institute
8600 West Bryn Mawr Ave.
Chicago, IL 60631-3562

10. SPONSORING/MONITORING AGENCY REPORT NUMBER

GRI-97/0361

11. SUPPLEMENTARY NOTES

12a. DISTRIBUTION/AVAILABILITY STATEMENT

12b. DISTRIBUTION CODE

13. ABSTRACT (*Maximum 200 words)*

A series of experiments, in which hydraulic fractures were monitored with an inclinometer array (downhole tiltmeter array), have been analyzed using both 2-D and 3-D finite-element codes. JAC2D and JAC3D, two conjugate gradient method codes, were used to calculate the earth tilt in vicinities of hydraulic fractures for comparison with experimental results. These analyses showed that variations in Young's modulus (or alternatively shear modulus) had a sizable effect on the induced inclinations, whereas both Poisson's ratio and stress had smaller effects. 2-D models were adequate for cases where fracture heights were relatively constant, while 3-D analyses were needed for more complex geometries. Comparison with field-experiment data showed that the fracture sizes needed to induce the measured inclinations were essentially the same as the fracture sizes obtained through microseismic methods, thus validating the microseismic results. Analyses such as these are proving that an inclinometer array can be a valuable diagnostic tool for hydraulic fracturing, as well as other downhole processes.

14. SUBJECT TERMS

Tight gas sands, in situ stress, stress measurement, hydraulic fracturing, tiltmeters, inclinometers, in situ modulus

fracture diagnostics, fracture height, fracture containment, finite element analyses

15. NUMBER OF PAGES
96

16. PRICE CODE

17. SECURITY CLASSIFICATION OF REPORT	18. SECURITY CLASSIFICATION OF THIS PAGE	19. SECURITY CLASSIFICATION OF ABSTRACT	20. LIMITATION OF ABSTRACT
Unclassified	Unclassified	Unclassified	

GRI DISCLAIMER

Title Hydraulic Fracture Imaging Using Inclinometers At M-Site: Finite-Element Analyses Of The B-Sandstone Experiments

Contractor Sandia National Laboratories
GRI Contract Number: 5089-211-2059

Principal Investigators B. P. Engler
N. R. Warpinski

Report Period December 1997
Topical Report

Objective To develop, improve, and apply technology for imaging hydraulic fracture treatments conducted in gas reservoirs in order to provide information on fracture size and shape that can be used to optimize fracturing.

Technical Perspective Large quantities of natural gas exist in low permeability reservoirs throughout the US. Characteristics of these reservoirs, however, make production difficult and often uneconomic. Matrix rock permeabilities are often submicrodarcy, and natural fractures are commonly marginal, being anisotropic and easily damaged. Stimulation is required for these types of reservoirs, with hydraulic fracturing being the primary stimulation option. Understanding stimulation behavior is difficult, however, because of the complex nature of most of these reservoirs. Diagnostics that can map out the fracture length, height, and azimuth are the missing element in hydraulic-fracture analysis. Although microseismic mapping is considered the principle diagnostic for overall fracture shape, results from the M-Site experiments have shown that inclinometers, or down-hole tiltmeters, have significant potential for diagnosing some elements of fracture geometry, as well as other attributes not easily measurable with microseisms. The measurements from the tiltmeters, which essentially measure the mechanical response of the formation to the induced fracture, were used to prove the

accuracy of the microseismic results and validate that technology.

Results Seven fracture injections were conducted in the B sandstone at M-Site, of which six injections (not the initial breakdown) were monitored using microseisms and all seven were monitored with inclinometers. The inclinometer array, consisting of six vertically spaced bi-axial tiltmeters in an offset well, provided accurate information on fracture height and width, and second order accuracy on fracture length.

The tiltmeters data were analyzed using several analytic models, which worked reasonably well but left some mismatches with peak amplitudes and tilt distributions. To refine the analytic solutions, it was necessary to apply finite-element models . These models could accommodate the modulus variations and shape variations that analytic models can not provide.

Several suites of finite element analyses of the B sandstone inclinometer results were completed and gave the final validation of the microseismic data. In all cases, the tiltmeter-deduced fracture heights were within a few feet of the microseismic-deduced fracture heights. It was also found that modulus variations in the thin layers have a significant effect on the inclinometer response and must be accounted for in highly layered environments, thus accounting for the difficulty in using the analytic models.

ABSTRACT

A series of experiments, in which hydraulic fractures were monitored with an inclinometer array (downhole tiltmeter array), have been analyzed using both 2-D and 3-D finite-element codes. JAC2D and JAC3D, two conjugate gradient method codes, were used to calculate the earth tilt in vicinities of hydraulic fractures for comparison with experimental results. These analyses showed that variations in Young's modulus (or alternatively shear modulus) had a sizable effect on the induced inclinations, whereas both Poisson's ratio and stress had smaller effects. 2-D models were adequate for cases where fracture heights were relatively constant, while 3-D analyses were needed for more complex geometries. Comparison with field-experiment data showed that the fracture sizes needed to induce the measured inclinations were essentially the same as the fracture sizes obtained through microseismic methods, thus validating the microseismic results. Analyses such as these are proving that an inclinometer array can be a valuable diagnostic tool for hydraulic fracturing, as well as other downhole processes.

Table of Contents

Figures

Figures Continued-

Tables

1.0 INTRODUCTION

The Gas Research Institute (GRI) and the U.S. Department of Energy (DOE) are currently sponsoring research aimed at developing fracture diagnostics which can be commercially used to image hydraulic fracture treatments at depth. The primary technology being used is the microseismic technique, as it is the one technology which has the capability for imaging length, height, azimuth and asymmetry, as well as providing information on fracture development with time. However, at the time this research was initiated, there was still a question of validation of the microseismic technique to prove that the "seismic" image represented the "mechanical" image, that is, the true size and shape of the fracture.

One approach to validation was to use inclinometers, which are downhole tiltmeters, to measure the mechanical response of the formation and thus produce an image of the "mechanical" shape which could be related to the "seismic" shape. An array of six bi-axial tiltmeters were cemented in a wellbore across from two sandstone intervals (B sandstone and C sandstone) which were to be hydraulically fractured and used to monitor the resultant deformation. Such an array would be capable of producing an image of the height of the hydraulic fracture from the induced deformation. Details of the experiments and results are given in Branagan et al.[1] and Warpinski et al.[2,3]

Analysis of the inclinometer results consisted of two parts: analytical models and finite element models. This report is a compilation of the 2-D and 3-D finite-element analyses and describes the development of the layered reservoir which was modeled and many of the ancillary discoveries made during this study.

One of the main findings of these tests is that inclinometers, or downhole tiltmeters, provide an accurate diagnostic for hydraulic fracture height growth which could be used for fracturing, waste disposal or other processes. When combined with surface tiltmeters or microseismic diagnostics, the combined techniques yield much additional information.

1.1 M-Site Background

M-Site is a jointly co-funded experiment between GRI and the U.S. DOE for the purpose of developing a field fracturing laboratory for fracture diagnostic development.[4] This facility is located in the Piceance basin of western Colorado near the town of Rifle. The section of interest at M-Site is the Mesaverde formation, located at depths from 4000-8200 ft. Previous work at the site consisted of the Multiwell Experiment[5] and the Slant-Hole Completion Test (SHCT),[6] so considerable information has been obtained from prior testing. Multiwell experiments were conducted at depths from 5500-8200 ft and SHCT tests were performed from 7000-8200 ft. The current M-Site target depth range is 4000-5000 ft, in rocks which have been undisturbed by past experimentation.

A plan view of the M-Site facility is shown in Figure 1. The site consists of a treatment well (MWX-2), a cased well for wireline microseismic arrays (MWX-3), a monitor well with cemented accelerometer and inclinometer arrays, and two deviated lateral wellbores for intersecting the hydraulic fractures in each of the B and C sandstones. Of interest for this report is the treatment well where fracturing was conducted and the monitor well where the inclinometer array was situated.

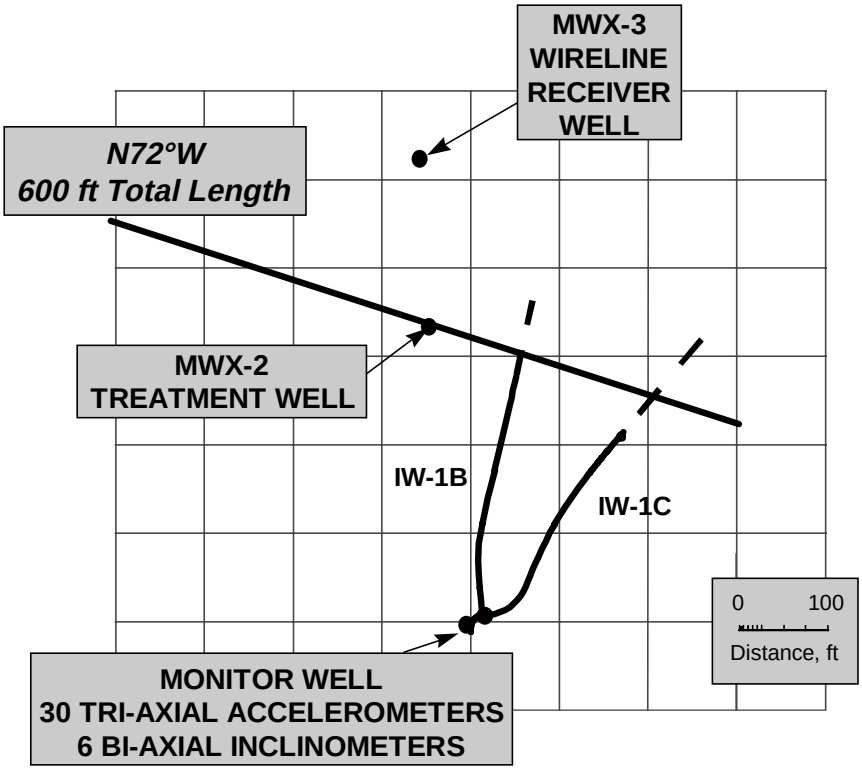

Figure 1. Plan view of M-Site layout.

Details of the monitor-well drilling, logging and instrumentation are given in Peterson et al.[7] As shown in Figure 2, the monitor well was designed to monitor fracture treatments in both the B and C sandstone, supplemented by wireline accelerometer arrays in MWX-3 and other instrumentation (primarily pressure) in the treatment well. The tiltmeters emplaced in the monitor well are Model 510 Geodetic Borehole Tiltmeters from Applied Geomechanics, Inc. They are bi-axial devices having resolution of 10 nanoradians or better. The tilt range is adjustable mechanically through ± 3°, with an actual operating range of ± 900 microradians. These devices were attached to cables, strapped to tubing, inserted in the monitor well and cemented in place during late 1994. The tiltmeters are situated so that the y axis of the tiltmeter is essentially orthogonal to the fractures created in MWX-2 and the x axes are parallel. Thus, no additional vector manipulation is required to extract these components. For this report, all of the results deal with the orthogonal, or y tilts. The normal distance from the fracture plane to the monitor well is approximately 300 ft, while the lateral offset distance is approximately 150 ft.

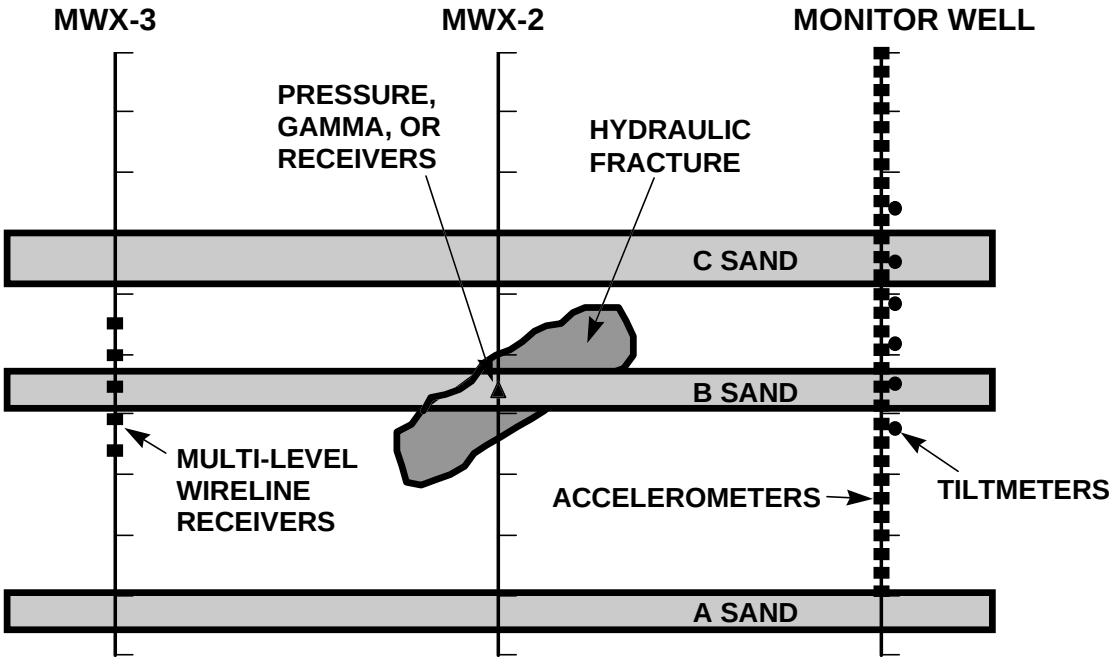

Figure 2. Side view of M-Site layout.

Additional information obtained in the treatment well, such as bottom-hole pressure, spectral gamma logs of radioactive tracer distributions, and seismic surveys, are used for detailed fracture modeling and additional diagnostic information. Detailed stress, rock property and reservoir property data are also available from previous testing at this site, as well as from current drilling, logging and testing. The B sandstone is a fluvial sandstone, but its lithology is somewhat complicated by a second sand lobe that lies below the main interval of the B sandstone.

1.2 B Sandstone Fracture Injections

During B-sand testing, seven different fracture injections using three different fluids were monitored. Important information on the injections is given in Table 1. The first injection (1B) is not given in the table nor is it analyzed as its size was too small to acceptably use inclinometers for detailed examination. Injection 2C-4C were small KCl fractures for calibration purposes. Injection 2C was a step-rate test with rates up to 3 bpm and a volume of 27 bbl. Injections 3C and 4C were both pumped at 10 bpm, with volumes of 100 and 210 bbl, respectively. Injections 5C and 6C were duplicate injections of 40# linear gel at rates of 22 bpm and total volumes of 400 bbl. Injection 7C was a propped stimulation using 670 bbl of fluid and 77,600 lb of sand. The sand was ramped in at concentrations of 1ppg to 8 ppg. This injection used a cross-linked gel at a 40#/1000 gal loading.

Table 1 Treatment Data

	FRACTURE	VOLUME (bbl)	FLUID	RATE (bpm)	SAND (LB)
2B	Step-Rate	27	KCl	0.5-3	
3B	Pump-In #1	100	KCl	10	
4B	Pump-In #2	210	KCl	10	
5B	Minifrac #1	400	40# Linear	22	
6B	Minifrac #2	400	40# Linear	22	
7B	Propped Frac	670	X-Link Gel	20	77,600

2.0 M-SITE TILTMETER OBJECTIVES

The principal objective of the inclinometer imaging of the B sandstone fractures was to validate fracture height of the microseismically derived images. The single vertical array of downhole tiltmeters produces a representation of the deformation surrounding the hydraulic fracture from which the fracture characteristics can be deduced. This deformation-deduced fracture height can then be compared with the microseismic height to prove or disprove the validity of the microseismic images. These inclinometers thus had a critical role in establishing the accuracy of microseismic fracture heights.

There were several secondary objectives as well, but these were not related to the finite-element modeling and are not covered here. These objectives included stress determination, measurement of proppant distribution, evaluation of proppant convection, measurement of long term changes around fracture stimulations, and others.

3.0 INCLINOMETER/TILTMETER BACKGROUND

Tiltmeters are well-known sensing devices for accurately determining the angular movement of a surface or mass. These sensors are typically bubble elements with an electrolytic fluid which displaces slightly as the device tilts. Electrodes sense changes in the resistance due to the fluid displacement and a voltage output proportional to the tilt is produced.

3.1 Surface Tiltmeters

Tiltmeters have successfully been employed for years as a surface monitoring technique for hydraulic fractures (Davis,[8] Palmer,[9] Wright and Conant[10]). These devices provide reliable information on fracture azimuth and, occasionally, can also provide other useful information about fracturing characteristics, particularly fracture volume. Surface tiltmeters are generally fielded in a variably circular array around the injection well, with the radial distance being appropriately spaced relative to the depth of the reservoir and the expected length of the fracture. For a vertical hydraulic fracture, the resultant surface tilt field is usually planar symmetric, with either side of the fracture having a tilt field pointing toward the fracture. From the axis of symmetry the azimuth can be estimated and from the tilt amplitudes and their distribution the volumetrics can be estimated.

The primary difficulties with performing surface tiltmeter studies are (1) depth limitations, (2) tidal noise, and (3) cultural noise. These three features tend to work together to make data acquisition complicated. Background data need to be taken for several days to record the tidal tilts and daily variations in the cultural noise (due to traffic, trains, irrigation, etc.) These background tilts are subtracted from the tilts taken during the fracturing to leave a residual signal which may range from a few tens of nanoradians to several hundred nanoradians for fractures at depths of a few thousand feet. However, for deeper fractures the signal continues to decrease and may fall below the range of resolution. When adequate signals are obtained, the data can then be inverted for results.

3.2 Inclinometers (Downhole Tiltmeters)

This report describes the use of tiltmeters in a new mode which is proving useful for extracting other valuable information about fracture dimensions and fracture mechanisms. The method of deployment is a vertical array of tiltmeters, now called an inclinometer array to distinguish it from surface tiltmeters, cemented in place in an offset well, at a depth directly across from the hydraulic fracture.[1] Being in a nearby offset well, the inclination amplitudes are several orders of magnitude greater than would be detected at the surface. Furthermore, since the inclination is a gradient of the strain, all of the crack models in the literature can be re-interpreted in terms of the inclination and exactly the same information can be obtained as if stress or strain measurements were made. In particular, a linear array of inclinometers in a vertical well adjacent to a hydraulic fracture

provides highly sensitive data on the fracture height and width and second order sensitivity on the length.

To obtain the maximum amount of information from this deployment, of vertical array of several inclinometers (at least 5) must be placed in an offset well above, in, and below the reservoir which is being fractured. The actual spacing depends on the distance away and the height of the fracture, as the resulting deformation scales as 2d/H, where d is the orthogonal distance from the fracture and H is the fracture height. The two tiltmeter axes should be oriented, but if the inclinometer array is directly normal to a symmetric fracture, vector sums can be used to determine the orthogonal inclinations (there would be no lateral inclination). In general, however, the device must be oriented to correctly extract information from an arbitrarily placed array.

Analysis of the tilt field around fractures shows that the inclination field has an S-shaped character to it, as shown in Figure 3. The S shape arises from the fact that the rock mass curves one direction above the fracture and the opposite sense below the fracture. Directly across from the fracture there is lateral displacement but no tilt. This field has the characteristic that the peaks of the inclination are located at positions which depend only on 2d/H (for a homogeneous medium). Thus, the height of the fracture should be deducible from the position of the peaks. The amplitude of the peaks is proportional to the width of the fracture, which for a homogeneous medium is given by

$$w = \frac{2\left(1-\nu^2\right)H\Delta P}{E},$$

where ν is Poisson's ratio, E is Young's modulus, and ΔP is the net fracturing pressure. If H is determined from the position of the peaks, the width of the fracture can be deduced, assuming the elastic moduli are known, or the elastic moduli can be inferred if the net pressure has been accurately measured.

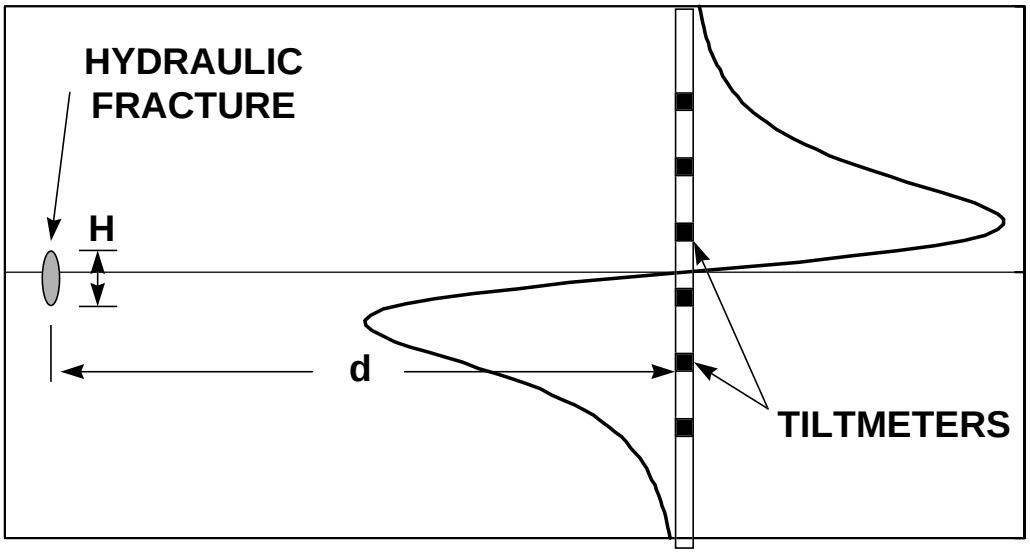

Figure 3. Schematic of inclinations orthogonal to a hydraulic fracture.

3.3 Analytic Models

There are several simple crack models which can be adapted for inclination calculations. These include the infinitely long 2-D crack,[11,12] the penny-shaped crack,[12] and a 3-D flat elliptic crack.[13] All of these models assume an infinite homogeneous medium and uniform pressure within the crack. In addition, there is a more complicated 2-D model based upon England and Green's formulation[14] which has been adapted and used for inclination modeling[15] for cases of non-uniform pressure or stress. The England and Green model is not included in this report as its tilt equations have already been published.

3.3.1 2-D Model

The simplest analytic solution for the tilt field around a fracture is that of an infinitely long 2-D crack, a solution that was developed by Westergaard[11] and Sneddon.[12] The geometry for this crack is shown in Figure 4. In their analysis, the crack half-height is c, and all locations are measured by the three distance parameters, r, r_1, and r_2, and the three angles θ, θ_1, and θ_2. The crack is uniformly pressurized at a level, P, in a material having a Young's modulus, E, and Poisson's ratio, ν.

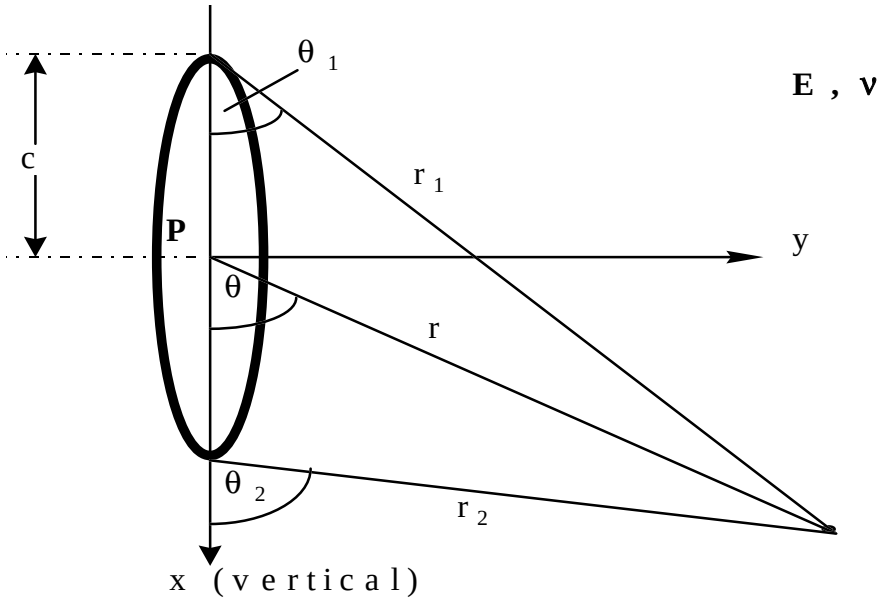

Figure 4. Geometry of a 2-D crack

Westergarrd gave his solution in terms of a stress function, Z, as

$$Z = P\left[\frac{z}{\sqrt{z^2 - c^2}} - 1\right],$$

where z is the complex variable, z = x + iy. The equations for the stress field around the crack are given by Sneddon as

$$\frac{1}{2}\left(\sigma_x+\sigma_y\right)=\mathrm{Re}[Z]=P\left\{\frac{r}{r_1 r_2}\cos\left(\theta-\frac{1}{2}\theta_1-\frac{1}{2}\theta_2\right)-1\right\}$$

$$\frac{1}{2}\left(\sigma_y-\sigma_x\right)=y\,\mathrm{Im}[Z]=P\left\{\frac{r\sin\theta}{c}\left[\frac{c^2}{r_1 r_2}\right]^{\frac{3}{2}}\sin\left(\frac{3}{2}\theta_1+\frac{3}{2}\theta_2\right)\right\}$$

$$\tau_{xy}=-y\,\mathrm{Re}[Z']=P\left\{\frac{r\sin\theta}{c}\left[\frac{c^2}{r_1 r_2}\right]^{\frac{3}{2}}\cos\left(\frac{3}{2}\theta_1+\frac{3}{2}\theta_2\right)\right\}$$

The tilt field around the fracture can similarly be deduced as

$$\frac{\partial u_y}{\partial x}=\frac{2(1+\nu)}{E}\left\{\mathrm{Im}[Z]-\frac{y}{2}\mathrm{Re}[Z']\right\},$$

which can be written as

$$\frac{\partial u_y}{\partial x}=\frac{2(1+\nu)}{E}\left\{(1-\nu)\frac{r}{r_1 r_2}\sin\left(\theta-\frac{1}{2}\theta_1-\frac{1}{2}\theta_2\right)+\frac{r\sin\theta}{2c}\left[\frac{c^2}{r_1 r_2}\right]^{\frac{3}{2}}\cos\left(\frac{3}{2}\theta_1+\frac{3}{2}\theta_2\right)\right\}.$$

The tilt normal to the vertical plane is the only tilt that exists in the 2-D model, since the crack is infinitely long.

3.3.2 Penny-Shaped Model

For a penny-shaped crack, the problem is tractable because of the axisymmetry, but is still considerably more complicated than the 2-D crack. Sneddon[12] found the solution in terms of Bessel-function arguments as

$$\sigma_z=\frac{2P}{\pi}\left\{C_1^0-S_0^0+\zeta C_2^0-\zeta S_1^0\right\}$$

$$\tau_{zr}=\frac{2P\zeta}{\pi}\left\{C_2^1-S_1^1\right\}$$

$$\sigma_r+\sigma_\beta+\sigma_z=\frac{4(1+\nu)P}{\pi}\left\{C_1^0-S_0^0\right\}$$

$$\sigma_\beta-\sigma_r=\frac{2(1-2\nu)P}{\pi}\left\{C_1^2-S_0^2-\zeta C_2^2-\zeta S_1^2\right\}$$

where ζ = z/c, given the geometry of Figure 5.

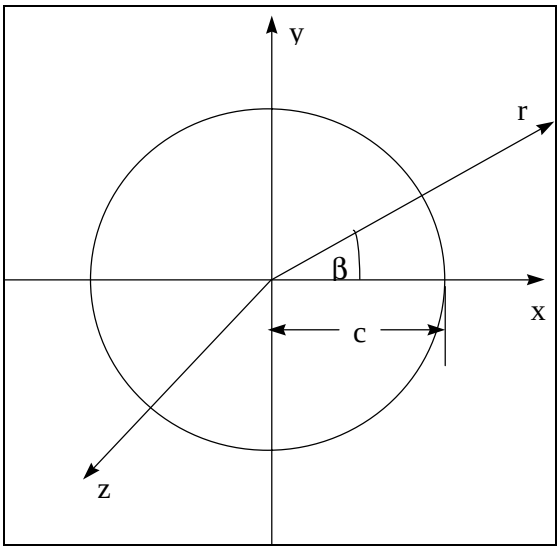

Figure 5. Geometry of a penny-shaped crack

Adopting the following notation,

$$\rho = r / c$$

$$r^2 = 1 + \zeta^2$$

$$R^2 = \left(\rho^2 + \zeta^2 - 1\right)^2 + 4\zeta^2$$

$$\zeta \tan\theta = 1$$

$$2\zeta \cot\phi = \rho^2 + \zeta^2 - 1$$

then the various S and C functions are given by

$$C_1^0 = \frac{1}{\sqrt{R}}\cos\left(\frac{\varphi}{2}\right) \qquad S_1^0 = \frac{1}{\sqrt{R}}\sin\left(\frac{\varphi}{2}\right)$$

$$C_2^0 = \frac{r}{R\sqrt{R}}\cos\left(\frac{3\varphi}{2} - \theta\right) \qquad S_2^0 = \frac{r}{R\sqrt{R}}\sin\left(\frac{3\varphi}{2} - \theta\right)$$

$$C_0^1 = \frac{1}{\rho}\left[\sqrt{R}\cos\left(\frac{\varphi}{2}\right) - \zeta\right] \qquad S_0^1 = \frac{1}{\rho}\left[1 - \sqrt{R}\sin\left(\frac{\varphi}{2}\right)\right]$$

$$C_1^1 = \frac{1}{\rho} - \frac{r}{\rho\sqrt{R}}\cos\left(\theta - \frac{\varphi}{2}\right) \qquad S_1^1 = \frac{r}{\rho\sqrt{R}}\sin\left(\theta - \frac{\varphi}{2}\right)$$

$$C_2^1 = \frac{\rho R}{\sqrt{R}}\cos\left(\frac{3\varphi}{2}\right) \qquad S_2^1 = \frac{\rho R}{\sqrt{R}}\sin\left(\frac{3\varphi}{2}\right)$$

$$C_1^2 = \frac{2}{\rho}C_0^1 - C_1^0 \qquad S_1^2 = \frac{2}{\rho}S_0^1 - S_1^0$$

$$C_2^2 = \frac{2}{\rho}C_1^1 - C_2^0$$

$$S_0^0 = \tan^{-1}\left[\frac{\sqrt{R}\sin\left(\frac{\theta}{2}\right)+r\sin\theta}{\sqrt{R}\cos\left(\frac{\theta}{2}\right)+r\cos\theta}\right], \quad \rho \neq 0$$

$$S_0^2 = \frac{1}{\rho}\left(C_0^1 - \zeta S_0^1\right)$$

To find the tilts, it is necessary to first obtain the strain and the gradients of the strains as

$$u_r = \frac{2Pc(1+\nu)}{\pi E}\left\{(1-2\nu)\left[C_0^1 - \frac{\rho}{2}\left(S_0^0 + S_0^2\right)\right] - \zeta\left[C_1^1 - S_0^1\right]\right\}$$

$$\frac{\partial u_r}{\partial r} = \frac{P(1+\nu)}{\pi E}\left\{(1-2\nu)\left[C_1^0 - C_1^2 - S_0^0 + S_0^2\right] - \zeta\left[C_2^0 - C_2^2 - S_1^0 + S_1^2\right]\right\}$$

$$\frac{\partial u_z}{\partial r} = \frac{4P(1-\nu^2)}{\pi E}\left\{C_1^1 - S_0^1 + \frac{\zeta}{2(1-\nu)}\left[C_2^1 - S_1^1\right]\right\}$$

From these terms, the tilts can be found as

$$\frac{\partial u_z}{\partial y} = \sin\beta\frac{\partial u_z}{\partial r}$$

$$\frac{\partial u_h}{\partial y} = \cos\beta\sin\beta\frac{\partial u_r}{\partial r} - \frac{\cos\beta\sin\beta}{r}u_r$$

where β is the angle from the center of the crack to the x,y position of the point of interest and r is the distance from the center of the crack to the point of interest.

3.3.3 Green and Sneddon's Elliptic Model

Considering a 3-dimensional flat elliptic crack opened by internal pressure and having the geometry shown in Figure 6, Green and Sneddon[13] found an analytical solution using the complex variable approach. The displacements and stresses can be given by

$$D = 8\frac{\partial}{\partial\bar{z}}\left\{(1+2\eta)\phi + Z\frac{\partial\phi}{\partial Z}\right\},$$

$$w = -8(1-\eta)\frac{\partial\phi}{\partial Z} + 4Z\frac{\partial^2\phi}{\partial Z^2},$$

$$\Theta = -8G\left\{(1-2\eta)\frac{\partial^2\phi}{\partial Z^2} + Z\frac{\partial^3\phi}{\partial Z^3}\right\},$$

$$\Phi = 32G\frac{\partial^2}{\partial\bar{z}^2}\left\{(1-2\eta)\phi + Z\frac{\partial\phi}{\partial Z}\right\},$$

$$\sigma_Z = -8G\frac{\partial^2\phi}{\partial Z^2} + 8GZ\frac{\partial^3\phi}{\partial Z^3} \text{ , and}$$

$$\Psi = 16GZ\frac{\partial^3\phi}{\partial\bar{z}\partial Z^2} \text{ ,}$$

with

$$D = \tilde{u} + iv \text{ ,}$$
$$\Theta = \sigma_x + \sigma_y \text{ ,}$$
$$\Phi = \sigma_x - \sigma_y + 2i\tau_{xy} \text{ ,and}$$
$$\Psi = \tau_{xz} + i\tau_{yz} \text{ .}$$

In these equations, G is the shear modulus of the material and η is Poisson's ratio. Additionally, Z is the third coordinate while $\bar{z}$ is the complex variable given by $\bar{z} = x + iy$.

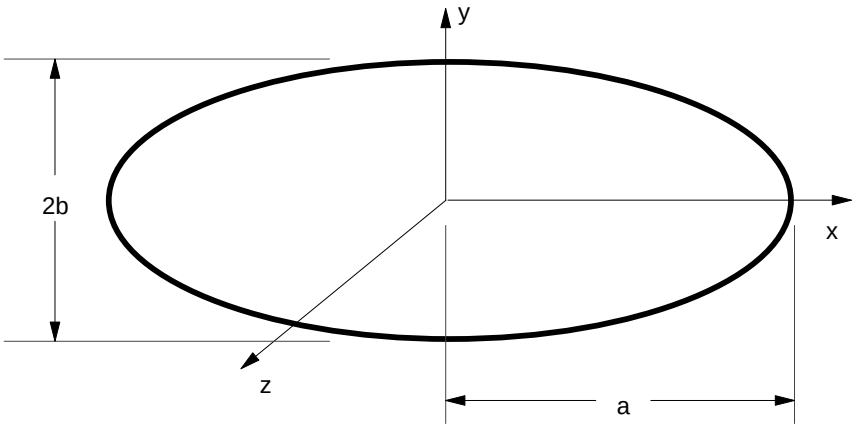

Figure 6. Geometry of fracture for tilt and stress calculations

Given such forms of the equations, Green and Sneddon found a solution of the problem by converting to an ellipsoidal coordinate system, λ, μ, ν, given by

$$a^2\left(a^2 - b^2\right)x^2 = \left(a^2 + \lambda\right)\left(a^2 + \mu\right)\left(a^2 + \nu\right)$$
$$b^2\left(b^2 - a^2\right)y^2 = \left(b^2 + \lambda\right)\left(b^2 + \mu\right)\left(b^2 + \nu\right)$$
$$a^2b^2Z^2 = \lambda\mu\nu$$

where

$$\infty > \lambda \geq 0 \geq \mu \geq -b^2 \geq \nu \geq -a^2 \text{ .}$$

In this coordinate system, the solution can be found as an integration of combined coordinates as

$$\phi = \frac{ab^2 p}{32GE(k)} \int_\lambda^\infty \left\{ \frac{x^2}{a^2+s} + \frac{y^2}{b^2+s} + \frac{Z^2}{s} - 1 \right\} \frac{ds}{\sqrt{s\left(a^2+s\right)\left(b^2+s\right)}} \ ,$$

where *E(k)* is an elliptic integral of modulus *k*, with

$$k = \frac{\sqrt{a^2-b^2}}{a} \ .$$

The tilts normal to the fracture can be found as

$$\begin{aligned}
\frac{\partial w}{\partial y} = \frac{-8(1-\eta)}{ab^2} \Bigg[& 2AZ \left\{ -k^2 \operatorname{sn}^2 u + \frac{\operatorname{sn}^2 u \operatorname{dn}^2 u}{\operatorname{cn}^2 u} \right\} \frac{du}{d\lambda} \frac{\partial \lambda}{\partial y} \\
& + 4Z \Bigg[\frac{2A}{ab^2} \left\{ -k^2 \operatorname{sn}^2 u + \frac{\operatorname{sn}^2 u \operatorname{dn}^2 u}{\operatorname{cn}^2 u} \right\} \frac{du}{d\lambda} \frac{\partial \lambda}{\partial y} \\
& + \frac{2AZ}{ab^2} \left\{ 2 \operatorname{sn} u \left(-k^2 \operatorname{cn} u \operatorname{dn} u + \frac{\operatorname{dn}^3 u}{\operatorname{cn} u} - k^2 \frac{\operatorname{sn}^2 u \operatorname{dn} u}{\operatorname{cn} u} + \frac{\operatorname{sn}^2 u \operatorname{dn}^3 u}{\operatorname{cn}^3 u} \right) \right\} \left(\frac{du}{d\lambda} \right)^2 \frac{\partial \lambda}{\partial y} \frac{\partial \lambda}{\partial Z} \\
& + \frac{2AZ}{ab^2} \left\{ -k^2 \operatorname{sn}^2 u + \frac{\operatorname{sn}^2 u \operatorname{dn}^2 u}{\operatorname{cn}^2 u} \right\} \left(\frac{d^2 u}{d\lambda^2} \frac{\partial \lambda}{\partial y} \frac{\partial \lambda}{\partial Z} + \frac{du}{d\lambda} \frac{\partial \lambda}{\partial y \partial Z} \right) \Bigg] \Bigg] \ ,
\end{aligned}$$

where sn, dn and cn are Jacobian elliptic functions, *A* is given by

$$A = -\frac{ab^2 p}{16G\,E(k)} \ ,$$

and *u* is defined as

$$\lambda = a^2 \frac{\operatorname{cn} u}{\operatorname{sn} u} \ .$$

The additional derivatives are found from

$$\frac{du}{d\lambda} = \frac{-\operatorname{sn}^3 u}{2a^2 \operatorname{cn} u \operatorname{dn} u} \ ,$$

$$\frac{d^2 u}{d\lambda^2} = \frac{-\operatorname{sn}^2 u}{2a^2} \left[3 + \frac{\operatorname{sn}^2 u}{\operatorname{cn}^2 u} + k^2 \frac{\operatorname{sn}^2 u}{\operatorname{dn}^2 u} \right] \frac{du}{d\lambda} \ ,$$

$$\frac{\partial \lambda}{\partial y} = \frac{2y\lambda\left(a^2+\lambda\right)}{(\lambda-\mu)(\lambda-\nu)} \ ,$$

$$\frac{\partial \lambda}{\partial Z} = \frac{2Z\left(a^2+\lambda\right)\left(b^2+\lambda\right)}{(\lambda-\mu)(\lambda-\nu)} \ ,$$

$$\frac{\partial^2 \lambda}{\partial y \partial Z} = \frac{yZ}{4\left(h_1^2\right)^2 \lambda\left(b^2+\lambda\right)} \left[-\frac{1}{\lambda} - \frac{1}{b^2+\lambda} + \frac{1}{2h_1^2} \left\{ \frac{x^2}{\left(a^2+\lambda\right)^3} + \frac{y^2}{\left(b^2+\lambda\right)^3} + \frac{Z^2}{\lambda^3} \right\} \right] ,$$

and

$$h_1^2 = \frac{(\lambda-\mu)(\lambda-\nu)}{4\lambda\left(a^2+\lambda\right)\left(b^2+\lambda\right)} \ .$$

Similarly, the tilts parallel to the fracture face are found from

$$\frac{\partial \tilde{u}}{\partial y} = \frac{8(1-2\eta)Ax}{a^3}\left\{-\frac{\mathrm{dn}^2 u}{k^2}+\frac{1}{k^2}\right\}\frac{du}{d\lambda}\frac{\partial\lambda}{\partial y}$$
$$+\frac{8AZ^2}{ab^2}\left[\mathrm{sn}\,u\,\mathrm{dn}\,u\left\{-2k^2\,\mathrm{cn}\,u+\frac{2\,\mathrm{dn}^2 u}{\mathrm{cn}\,u}-\frac{2k^2\,\mathrm{sn}^2 u}{\mathrm{cn}\,u}+\frac{2\,\mathrm{sn}^2 u\,\mathrm{dn}^2 u}{\mathrm{cn}^3 u}\right\}\left(\frac{du}{d\lambda}\right)^2\frac{\partial\lambda}{\partial x}\frac{\partial\lambda}{\partial y}\right.$$
$$\left.+\left\{-k^2\,\mathrm{sn}^2 u+\frac{\mathrm{sn}^2 u\,\mathrm{dn}^2 u}{\mathrm{cn}^2 u}\right\}\left\{\frac{d^2u}{d\lambda^2}\frac{\partial\lambda}{\partial x}\frac{\partial\lambda}{\partial y}+\frac{du}{d\lambda}\frac{\partial^2\lambda}{\partial x\partial y}\right\}\right]$$

where the additional derivatives are given by

$$\frac{\partial\lambda}{\partial x} = \frac{2x\lambda\left(b^2+\lambda\right)}{(\lambda-\mu)(\lambda-\nu)}$$

and

$$\frac{\partial^2\lambda}{\partial x\partial y} = \frac{xy}{4\left(h_1^2\right)^2\left(a^2+\lambda\right)\left(b^2+\lambda\right)}\left[-\frac{a^2+b^2+2\lambda}{\left(a^2+\lambda\right)\left(b^2+\lambda\right)}+\frac{1}{2h_1^2}\left\{\frac{x^2}{\left(a^2+\lambda\right)^3}+\frac{y^2}{\left(b^2+\lambda\right)^3}+\frac{Z^2}{\lambda^3}\right\}\right]$$

.

The procedure for using these equations is as follows:

1. Select point *x,y,Z* for which the calculation is to be made
2. Determine the appropriate λ,μ,ν for this point
3. Determine value of *u*
4. Obtain solutions

One confusing point is that *u* is used both for the displacement in the x direction as well as for a transformed function. However, this nomenclature was used in the Green and Sneddon paper and it has been kept here to facilitate referrals to the paper, except that $\tilde{u}$ has been used to denote the displacement. The only place the displacement enters is through the original complex equations and in the definition of the tilt.

4.0 M-SITE RESULTS FOR THE B SANDSTONE

4.1 Inclination Results

During the fracture injections conducted in the B sandstone, inclinometer measurements were made at relatively fast sample rates. Analytic models were used to provide initial estimates of fracture growth as given by Branagan[1] and these are not repeated here. Data were also stored for later use in more advanced analyses.

Figure 7 shows the time history of the inclination during injection 1B, the small cross-linked gel breakdown injection. This injection had a maximum response of about 700 nanoradians, which is about the maximum response ever seen on surface tiltmeters for these depths. The injection period was very short (2-3 min) and is represented by the section where the magnitude is increasing rapidly. The falloff period is very flat because of the low leakoff of the fluid and the continued length extension (which adds deformation). This fracture was so small, however, that no attempt was made to perform finite-element analyses.

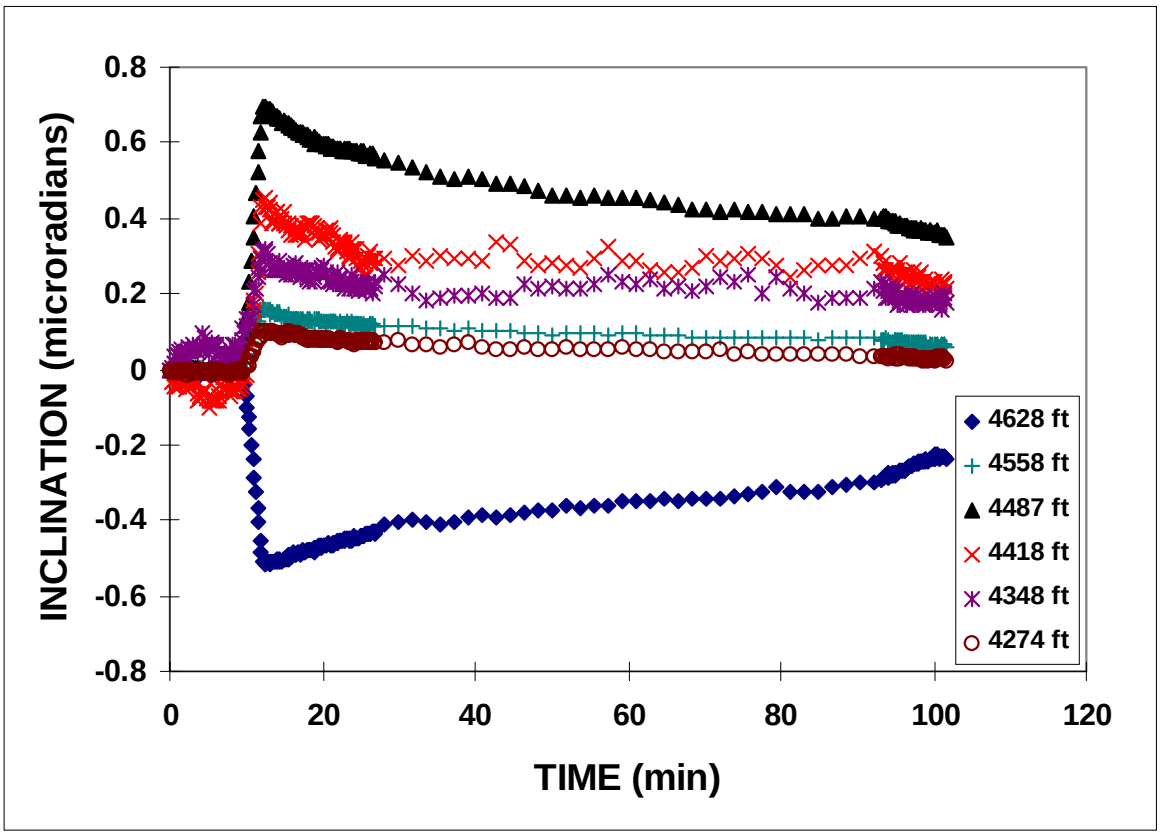

Figure 7. Inclination data for injection 1B.

The inclination data for injection 2B, the small step-rate test, are shown in Figure 8. In this case, the maximum amplitude is about 900 nanoradians and shows a slowly developing fracture for the first 15 minutes of the injection. In this case the falloff is also relatively fast.

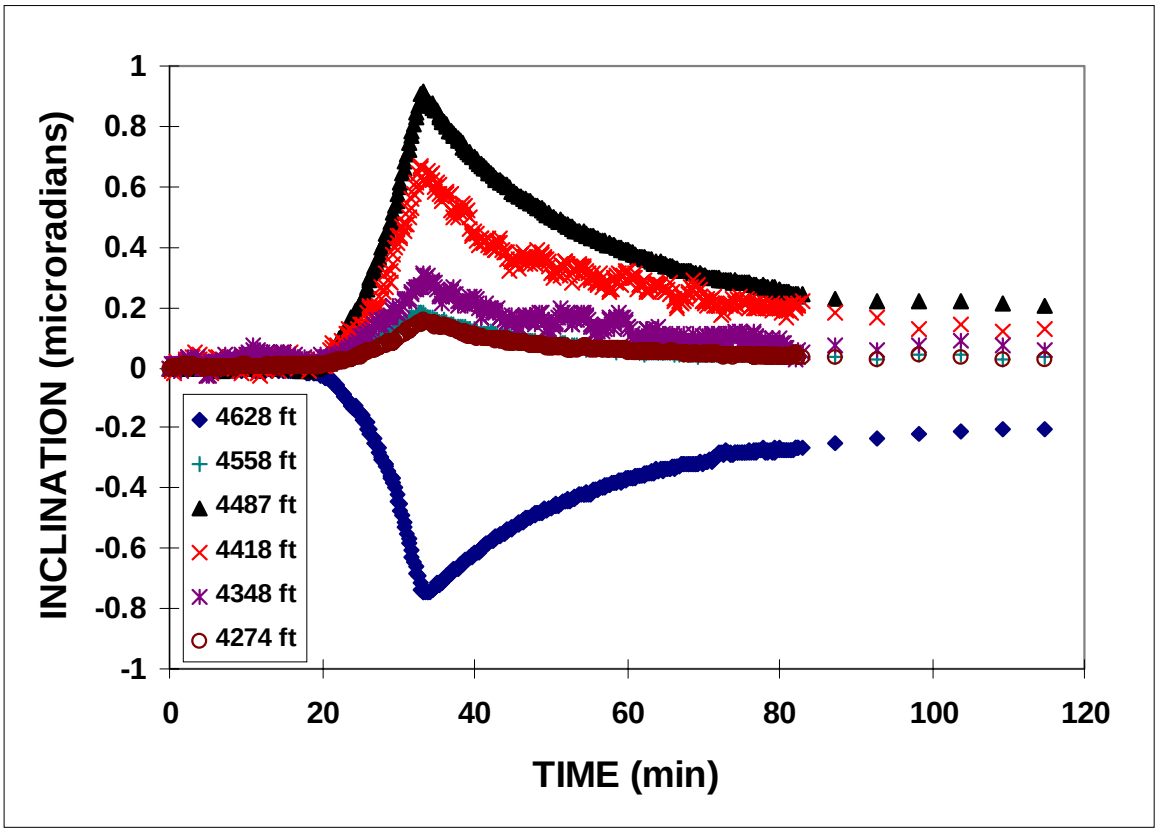

Figure 8. Inclination data for injection 2B.

The inclination results for injection 3B, the 100 bbl KCl treatment, are shown in Figure 9. The maximum response is almost 4,000 nanoradians, with the same rapid falloff as seen in the step-rate test. The only unusual feature is the "tear" in the data seen in the tiltmeter situated at 4558 ft. These sudden breaks in the data, which only seem to occur during fracturing, are probably slight rearrangements in the tiltmeter or its housing in response to the additional stress induced by the hydraulic fracture. The general procedure for handling these features is to remove the tear by shifting the post-tear magnitude to match the pre-tear value.

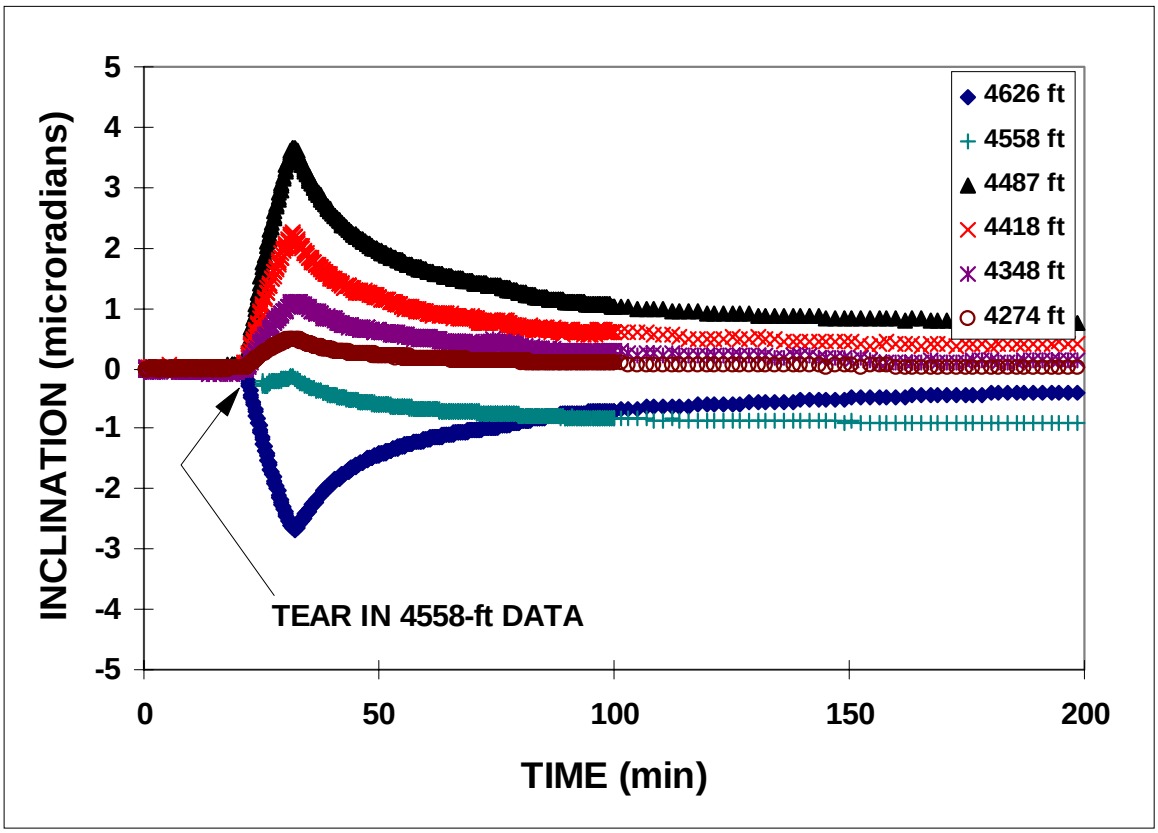

Figure 9. Inclination data for injection 3B

Similar data for injection 4B are shown in Figure 10. This injection was a 200-bbl KCl treatment pumped at the same rate as 3B. This test had a leak midway through the injection, which forced a 7 minute shut down and the resultant drop in inclination magnitudes. Otherwise, the data are similar to injection 3B but with a somewhat larger amplitude (about 4,500 nanoradians).

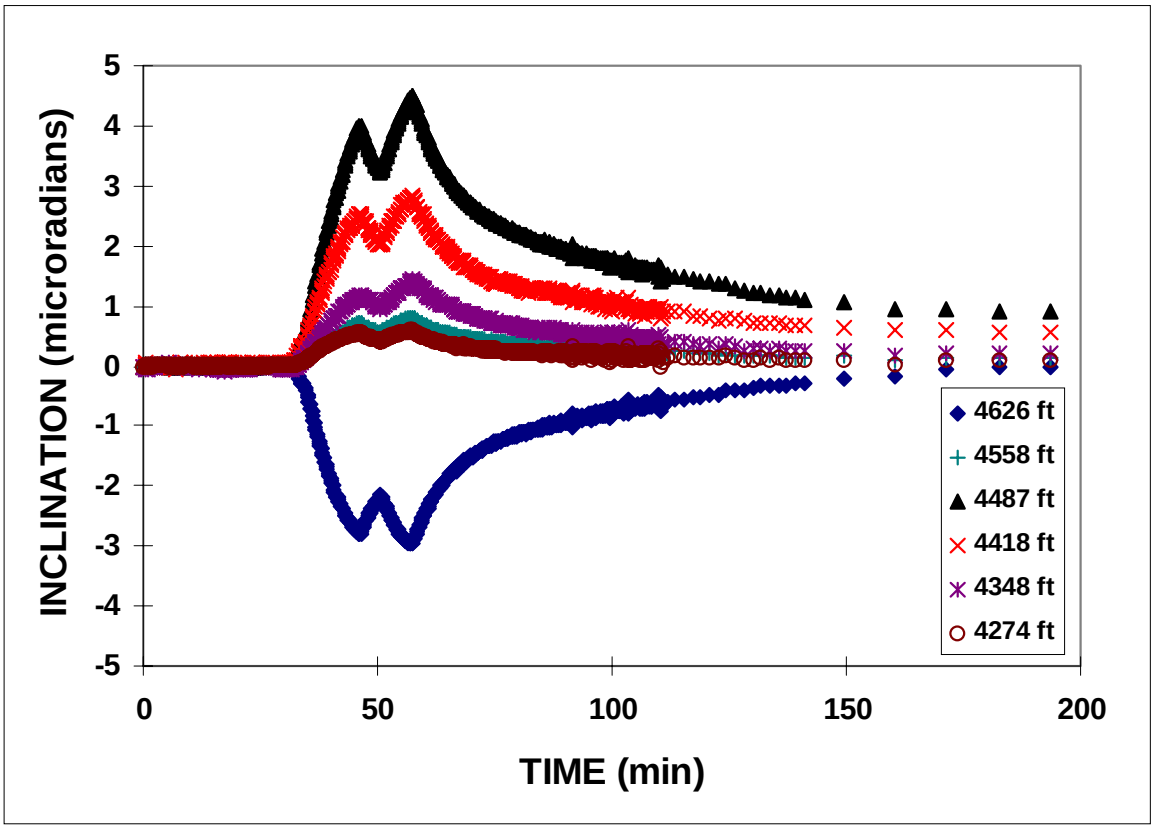

Figure 10. Inclination data for injection 4B.

Figure 11 shows the inclination data for the first linear-gel minifrac. This treatment resulted in a maximum amplitude of about 9,000 nanoradians and considerable asymmetry in the amplitude above the fracture compared to below the fracture. This behavior is likely due to asymmetric height growth.

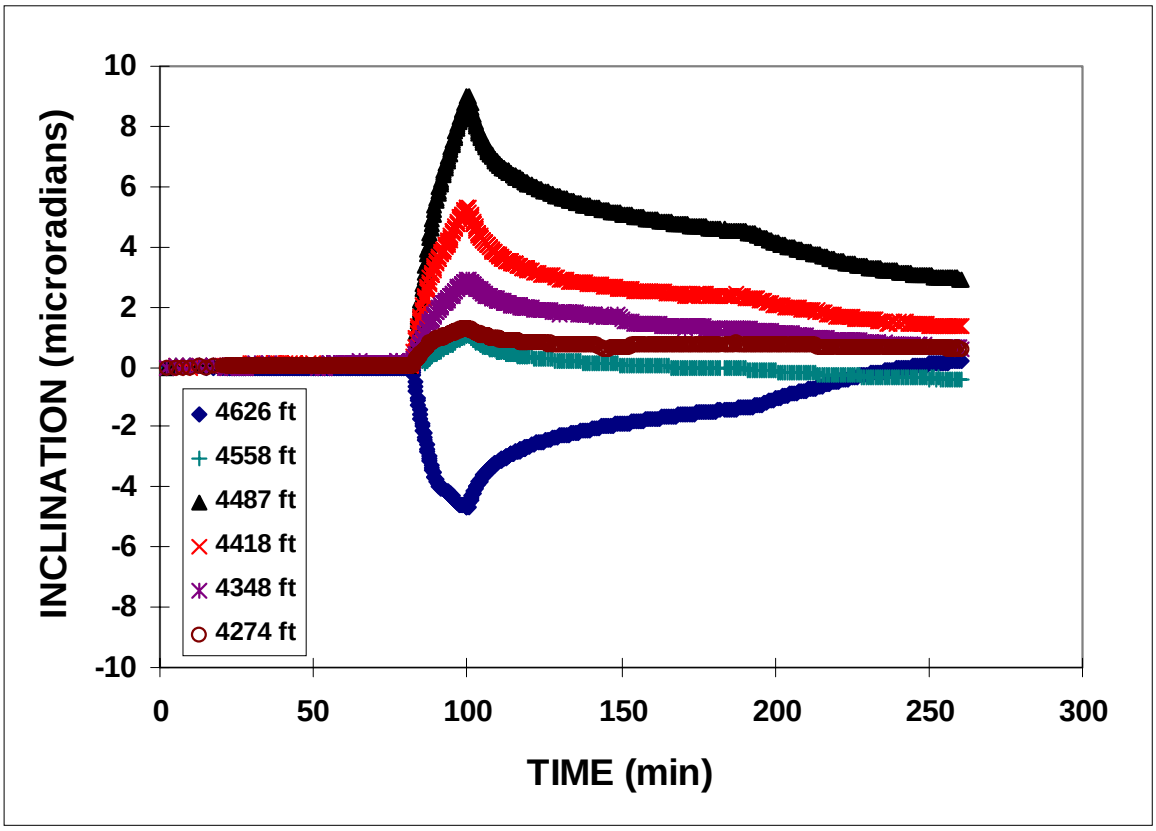

Figure 11. Inclination data for injection 5B.

Injection 6B, which was identical to injection 5B, had a very similar response, as shown in Figure 12. However, the maximum amplitude for injection 6B was about 500 nanoradians smaller than that of injection 5B.

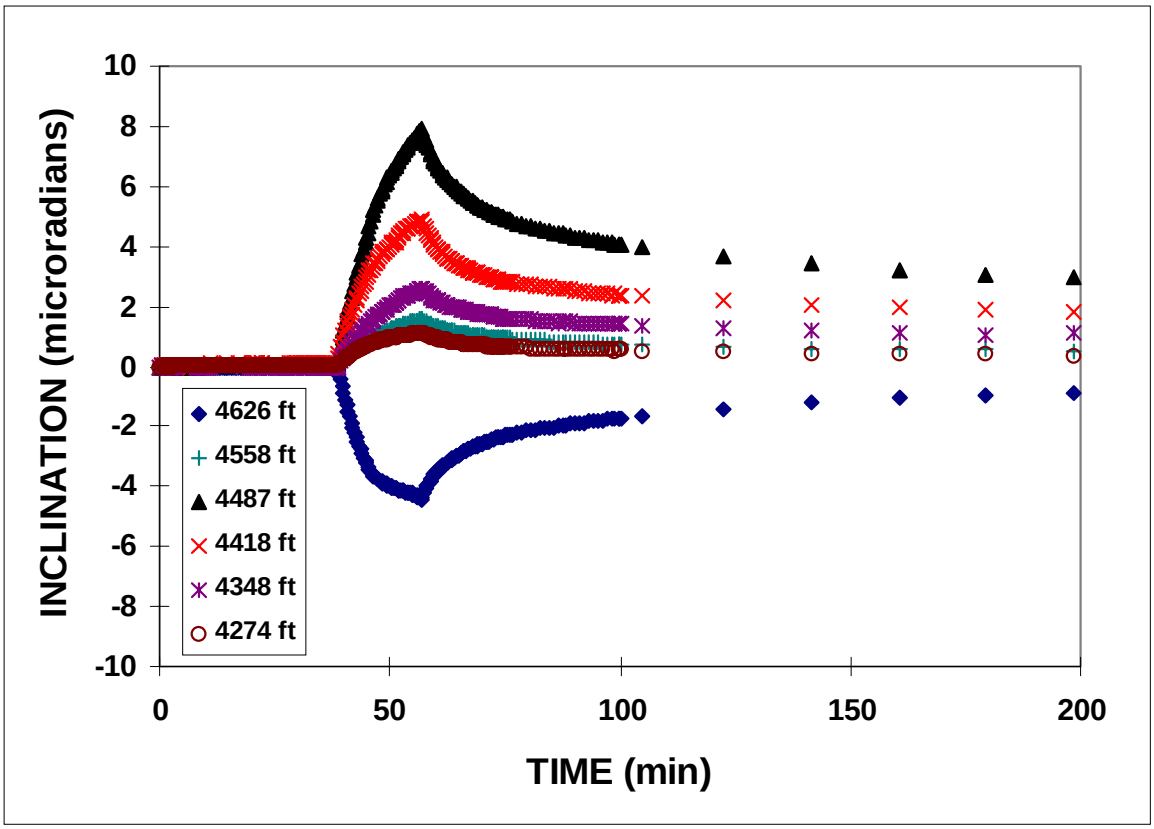

Figure 12. Inclination data for injection 6B.

The final fracture treatment in the B sandstone, injection 7B, had the inclination response shown in Figure 13. This injection induced a maximum inclination response of over 14,000 nanoradians. There were also some slope changes during the treatment that may have been caused by changes in height growth patterns.

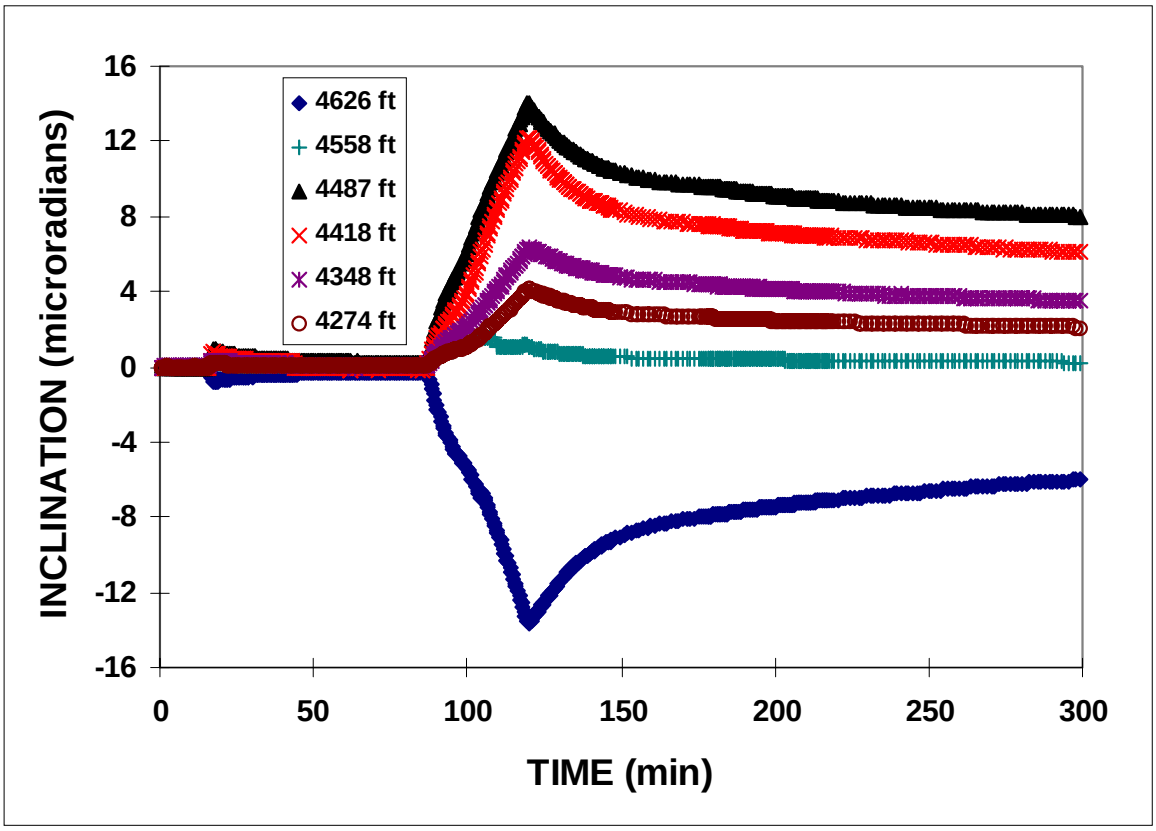

Figure 13. Inclination data for injection 7B.

For finite-element modeling, the primary interest is the maximum value of the inclinations at the end of the treatment, as this time represents the maximum crack height. Figure 14 shows the maximum inclinations values compared to the depth at which they were measured. All finite-element calculations are made to match these measured results as close as possible.

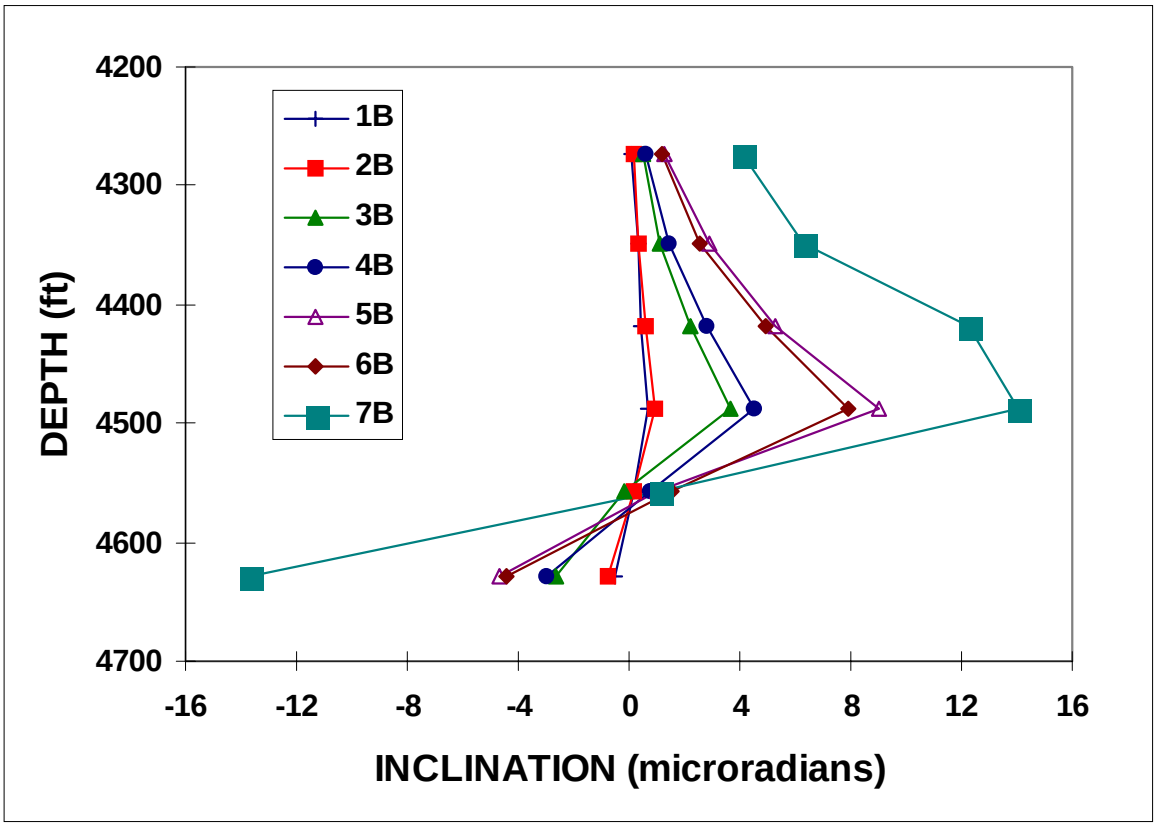

Figure 14. Maximum inclinations for each B sandstone injection.

4.2 Microseismic Results.

As noted previously, the major purpose of the inclinometers was to validate fracture parameters, particularly the height of the fracture. Microseismic measurements were made during all injections, but acceptable maps could only be generated for injections 2B-7B, as only a few microseisms were detected during the 1B breakdown. Details of the microseismic method and the results from the B sandstone are given in Warpinski et al.[2] but only the final map for each injection is given here for comparison with tiltmeter data.

A side view of the microseisms detected during the 2B injection is shown in Figure 15. This injection appears to have resulted in an asymmetric well-contained fracture. The average height for this treatment based on a statistical evaluation of the data is 40 ft. The fracture is also insufficiently long to accurately use a 2-D fracture model for inclination analyses.

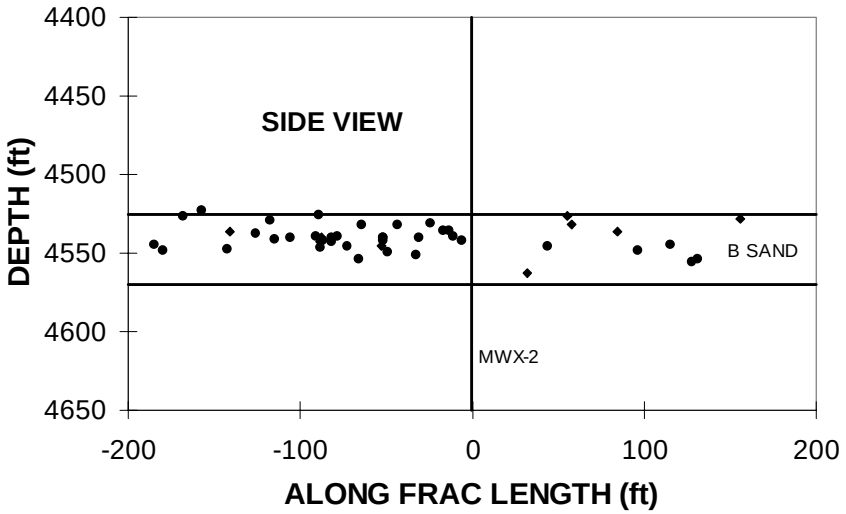

Figure 15. Microseismic side view for injection 2B.

A side-view plot of the microseisms are given in Figure 16. The average height for this fracture is about 55 ft. The length of about 350 ft on the east (right) wing is long enough for a 2-D model to give reasonable accuracy (15%).

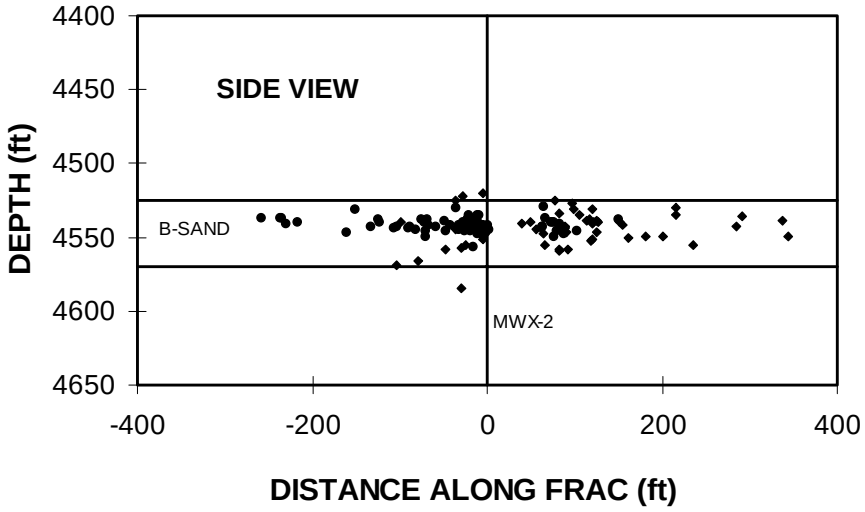

Figure 16. Microseismic side view for injection 3B.

Similar data for injection 4B are shown in Figure 17. The microseismic height is about 55 ft while the east wing length of nearly 450 ft and the nearly constant height on this wing are well suited for analysis with a 2-D model.

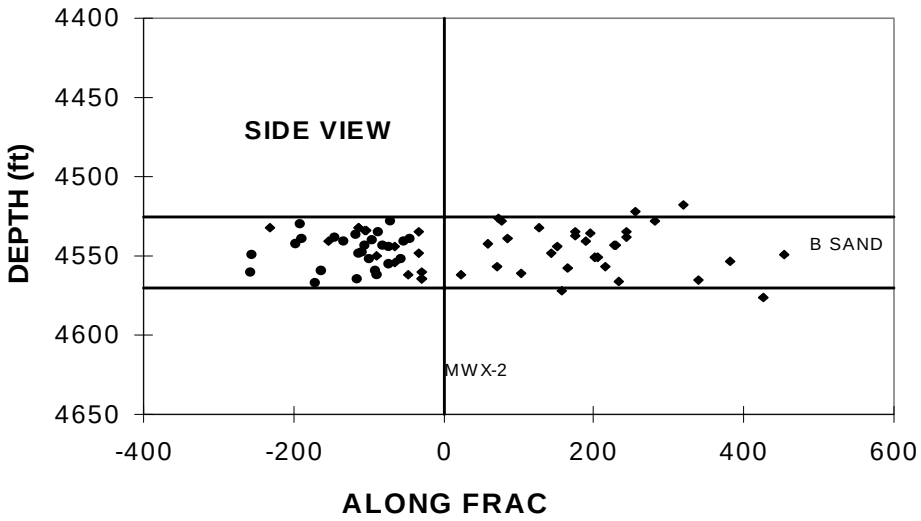

Figure 17. Microseismic side view for injection 4B.

The microseismic data for injection 5B are shown in Figure 18. This fracture shows some upward out-of-zone fracturing on the east (right) wing and a length of at least 400 ft on the east wing. The average fracture height is about 80 ft.

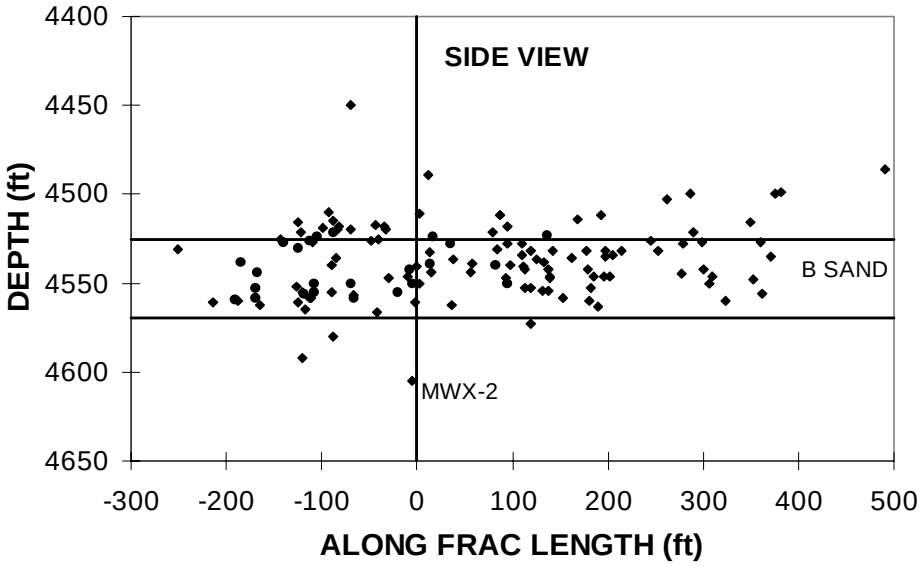

Figure 18. Microseismic side view for injection 5B.

The microseismic results for injection 6B are shown in Figure 19. This fracture is similar to injection 5B having an average height of 75 ft and an east (right) wing length of over 400 ft.

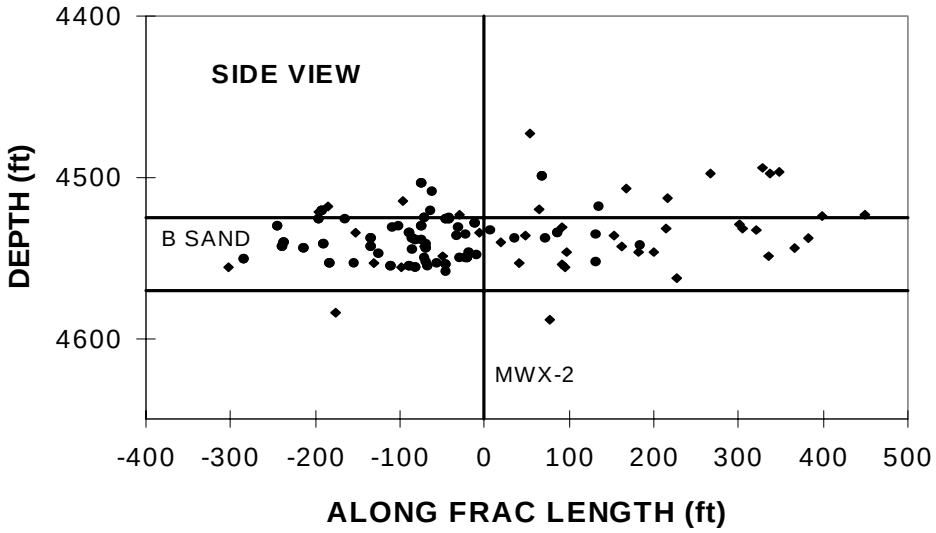

Figure 19. Microseismic side view for injection 6B.

The results for injection 7B are shown in Figure 20. This fracture shows considerable height growth with a total height of about 135 ft near the wellbore and on the order of 80 ft on the extremities. The east (right) wing length is on the order of 400-425 ft.

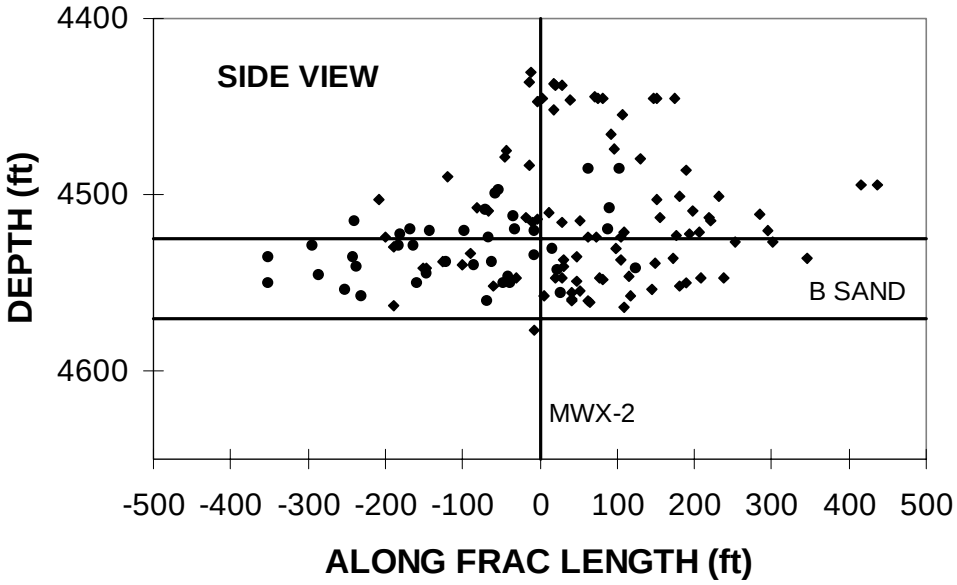

Figure 20. Microseismic side view for injection 7B.

Given these fracture dimensions from microseismic measurements, the fracture dimensions were interpreted initially using analytic inclination models. These models gave reasonably good agreement, but there were some features of the data that the analytic models could not match. Figure 21 shows one such example for the 6B injection where a 2-D model was used to match the results. The upper peak of the inclination distribution is much sharper than the analytic models predict. The actual peak in this case can be matched with a 90 ft tall fracture, but the fall off far overshoots the measured data. On the other hand, the falloff can be matched with a 60 ft fracture, but the peak is then ignored. It was felt that finite-element analyses incorporating modulus changes and stress variations could explain much of this behavior. The following sections describe the finite-element analyses that were performed to improve these comparisons.

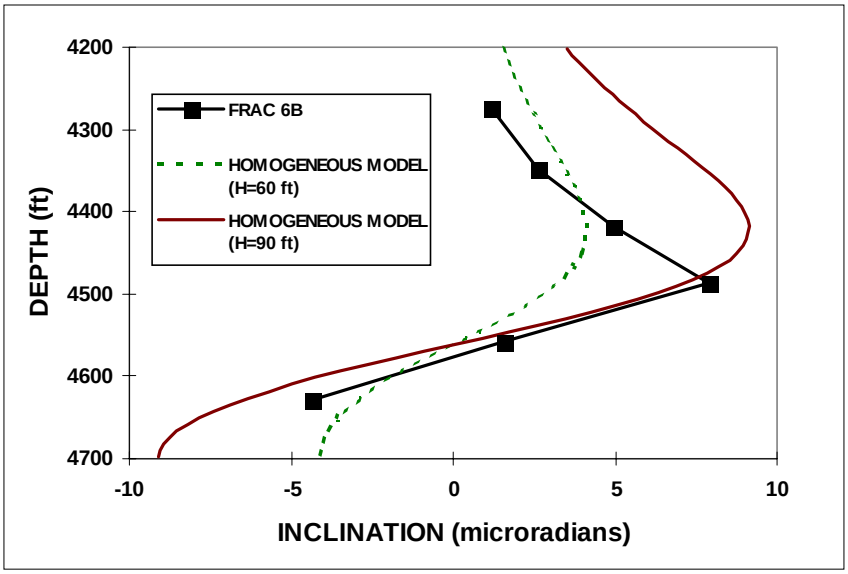

Figure 21. Example analytic matches illustrating discrepancies.

5.0 FINITE ELEMENT ANALYSIS CODE DESCRIPTION

Because of the discrepancies between the analytic solutions and measured results, it was suspected that modulus contrasts were responsible for the acceptable, but nonetheless imperfect inclination matches. It was also possible that stress contrasts had some role in altering the inclination field, although these were less important since they only had an effect where the fracture actually contacted a layer with different stress. Given the limited height in most of these injections, stress contrasts were considered to be a secondary factor.

Moduli contrasts, although pervasive in nature, cannot be accommodated using any known analytic crack models. To evaluate the possibility that these features were responsible for the discrepancies observed between analytic models and measured data, a series of finite element calculations were performed. These calculations used the JAC2D and JAC3D codes available at Sandia National Labs.

5.1 JAC2D and JAC3D

JAC2D[16] and JAC3D[17] are finite element analysis programs that are used for solving large deformation, temperature-dependent quasi-static mechanics problems in two and three dimensions respectively. A nonlinear conjugate gradient technique is used to solve the governing nonlinear equations. The method is implemented in a two or three dimensional setting with various methods for accelerating convergence. Zero-energy modes are controlled through the use of a four-node Lagrangian uniform strain element with hourglass stiffness.

JAC2D and JAC3D are written in modular form thus allowing the use of any one of seven continuum material models presently developed to be incorporated within the analysis. When combined with these and other ancillary capabilities, these versatile programs allow for the solution to linear or nonlinear problems that involve time-dependent and/or time-constant loads, kinematic boundary constraints, element birth and death, thermal history and fixed and/or sliding contacting surfaces.

The JAC2D and JAC3D codes were the algorithms from which all finite element calculations were derived. These codes output the stresses and strains as a function of nodal or element position within the body.

5.2 TILTDERV Code

TILTDERV is a flexible program that through the use of a high-order polynomial spline function will produce a curve, fit to the appropriate displacement data output by JAC2D or JAC3D. This code allows fits up to 20th order and the derivative of this fit data can then be calculated thus producing the associated tilt. For this study, a 12^{th} order fit was nominally used upon the displacement data.

6.0 FINITE ELEMENT ANALYSIS - 2D

6.1 Homogeneous Base Case

In order to verify the proper implementation and operation of the software code, two initial models were constructed that consisted of three homogeneous regions each, where region #1 consists of the material below the reservoir, region #2 consists of the reservoir region, and region #3 consists of the material above the reservoir (Figure 22).

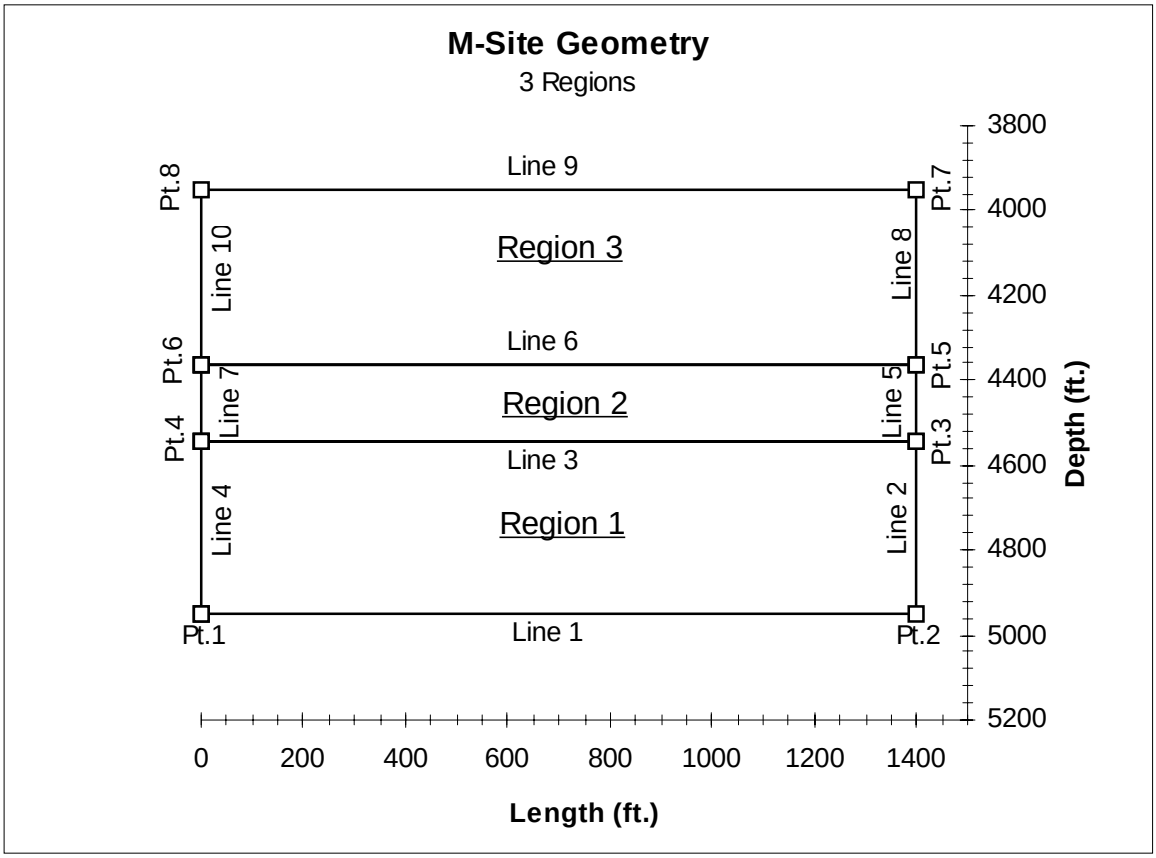

Figure 22. Finite Element Geometry - 3 Regions.

The geometry of the model is defined by using a number of wire frame type entities and description parameters. These entities are defined and related in a manner appropriate to describe the boundaries of the regions to be meshed utilizing four node quadrilateral element types. Quadrilateral elements are generated from geometric regions which are a closed set of lines with opposing sides of equal interval assignment. Identifier flags are attached to the mesh to define the appropriate boundary conditions, loading conditions, and material properties. The actual loads and material properties are indicated within the input file to the analysis code and are associated to the generated mesh through the use of these identifier flags. An example of the meshed model is shown in Figure 23 which consists of 434 quadrilateral elements and 480 nodes.

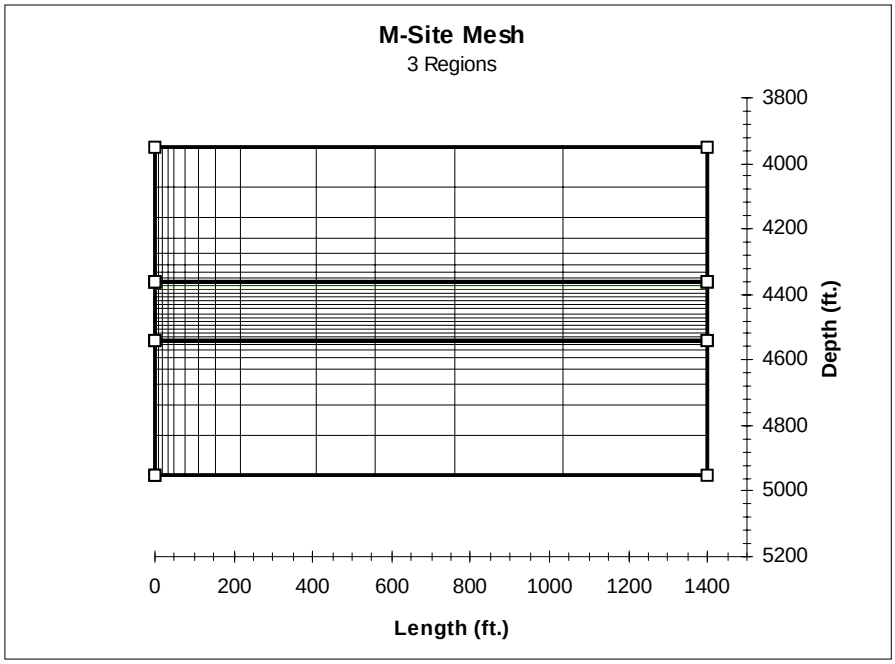

Figure 23. Finite Element Mesh - 3 Regions.

The sole difference between the two models generated was the introduction of in-situ stress into the analysis in model number two. The material properties utilized for these regions are listed in Table 2.

Table 2 Material properties for homogeneous base-case calculations

	Young's Modulus	Poisson's Ratio	In-Situ Stress
	(million psi)		(psi)
Model #1			
Region #1	5.0	0.2	0
Region #2	5.0	0.2	0
Region #3	5.0	0.2	0
Model #2			
Region #1	5.0	0.2	1200
Region #2	5.0	0.2	0
Region #3	5.0	0.2	800

The values chosen are representative of actual material properties for the fracture site except for the in-situ stress values which merely provide contrast. The fracture modeled in this case was produced by a pressure of 1000 psi applied over a total height of 220 feet (4341-4561 feet). This included all of Region #2 (4361-4541 feet) and 20 feet of both Region #1 and Region #3.

Several variations of the modeled mesh were constructed in order to determine the appropriate nodal spacing at the boundaries of the fracture and regional interfaces. This is critical if sufficient accuracy and resolution in the resulting analysis is to be obtained. The crack width produced at the borehole for the homogeneous model #1 is shown in Figure 24 along with the fracture parameters used. As anticipated, the width produced is symmetrical in shape about the horizontal plane, confined within the boundaries of the fracture, and the height is fully supported by the fracture pressure. The tilt produced by this fracture is therefore symmetrical and centered about Region #2, as seen in Figure 25.

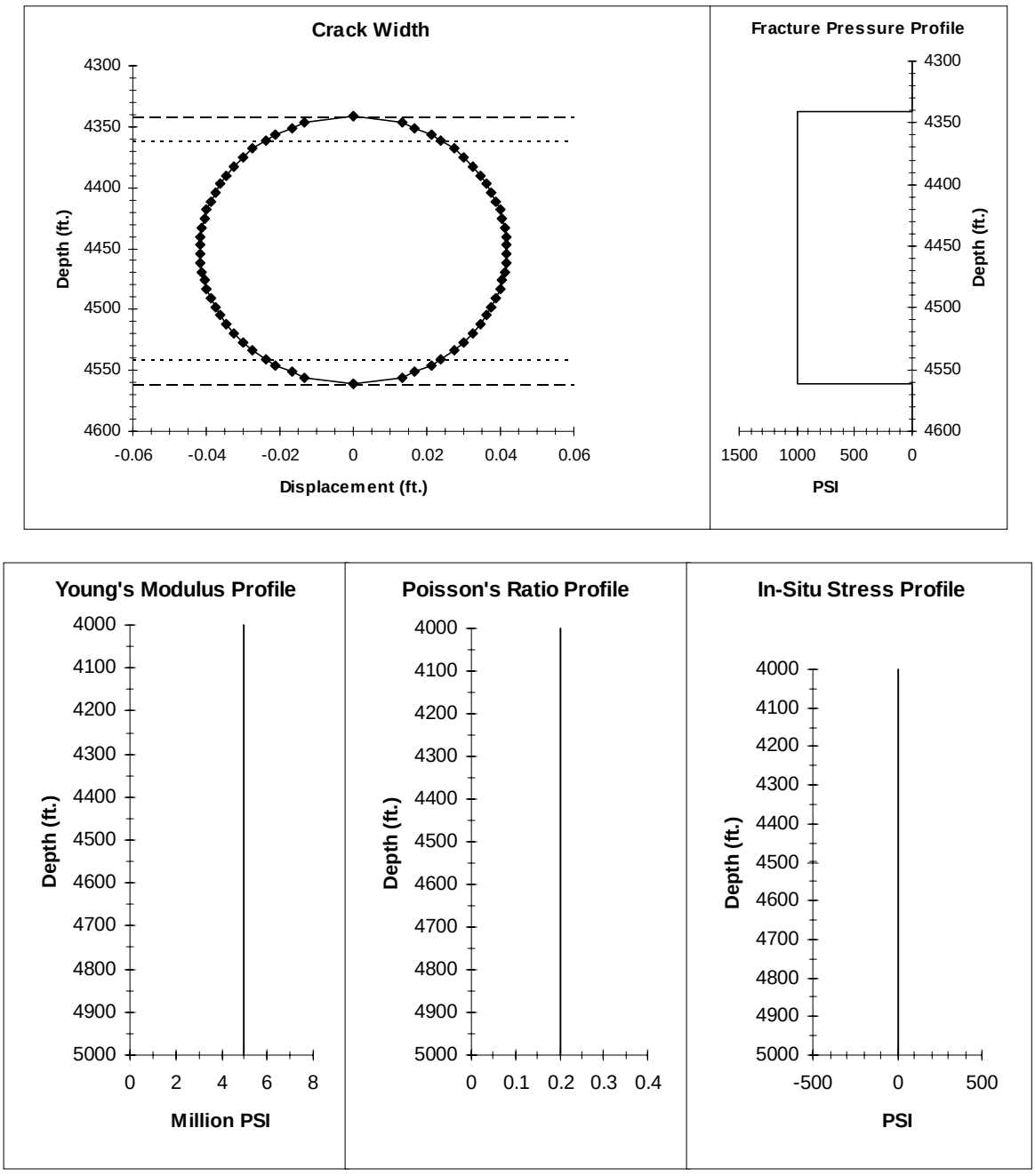

Figure 24. Homogeneous base case #1.

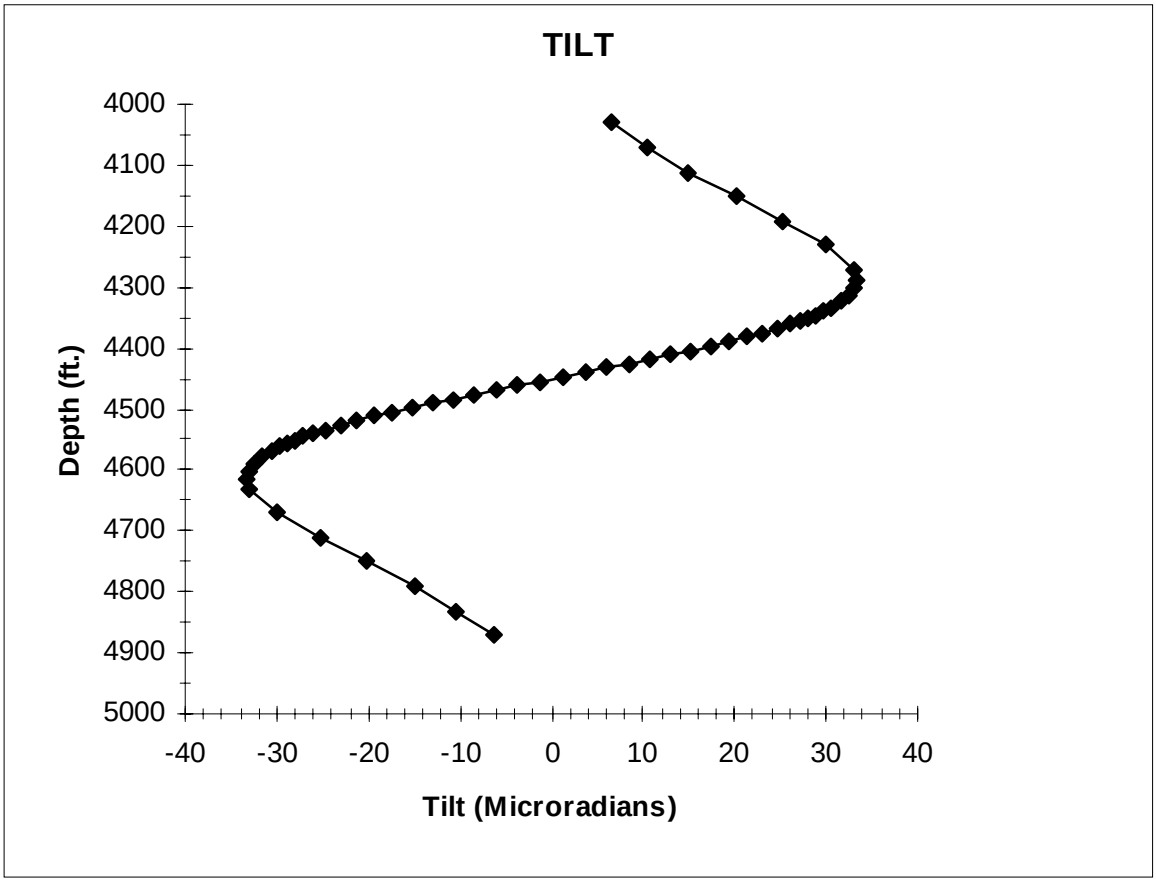

Figure 25. Homogeneous base case #1.

In model #2, the in-situ stress was introduced for the appropriate region and the analysis was rerun. As seen in Figure 26, the crack width produced is no longer symmetrical in shape about the horizontal plane but instead has minor differences in the displacement produced within Region #2 and Region #3 due to the difference in in-situ stress values applied. The resulting tilt, in Figure 27, shows this difference more clearly in that even though the tilt is still centered about Region #2, the peak magnitude of the tilt in the adjoining regions is different.

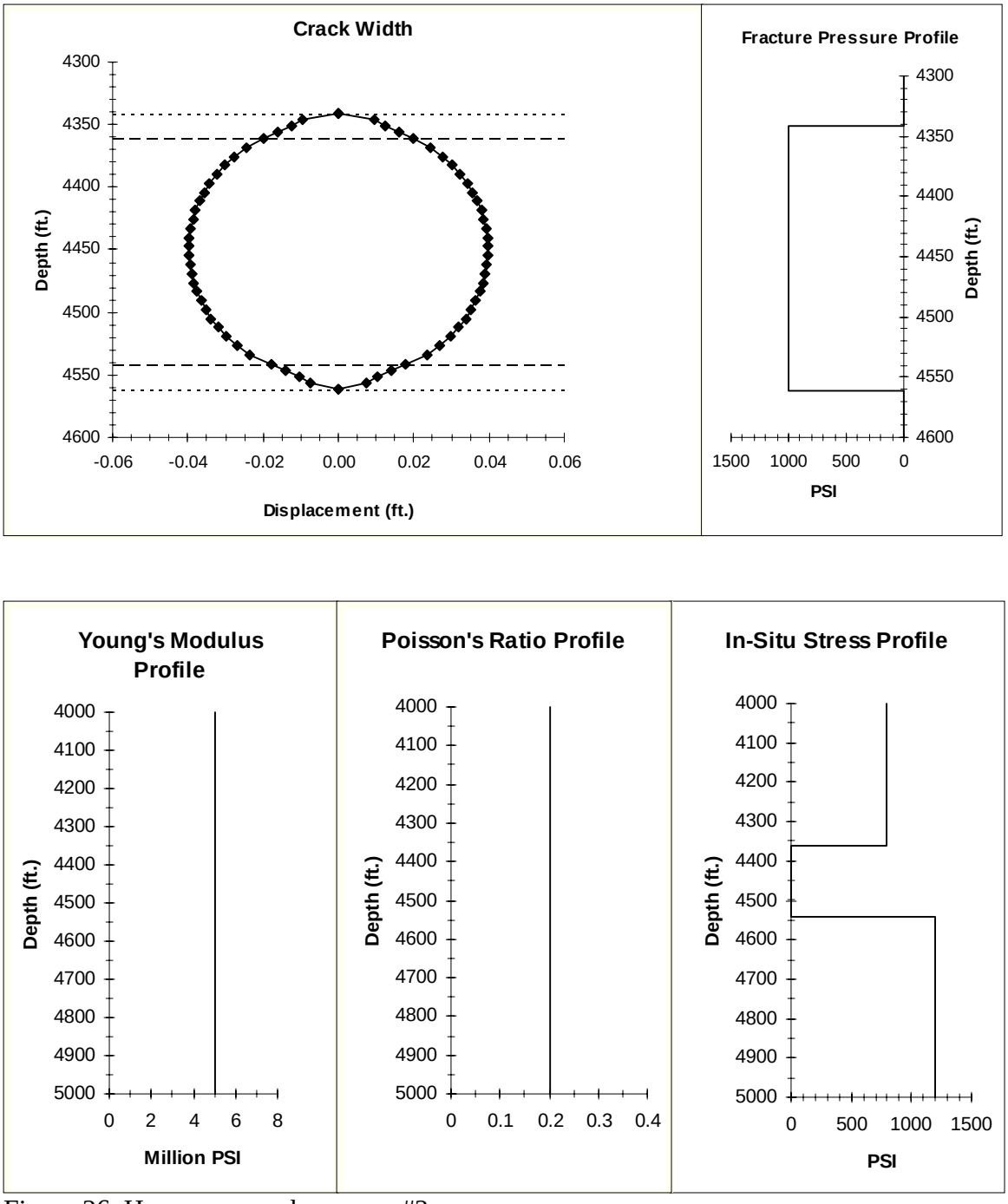

Figure 26 Homogeneous base case #2.

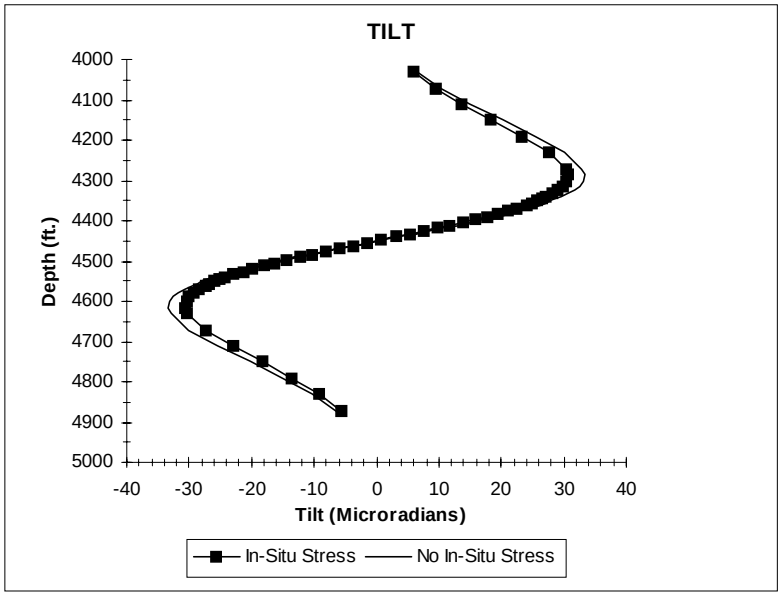

Figure 27. Comparison of in-situ stress effect upon homogeneous base case.

The results of the two homogeneous cases analyzed indicate that the code has been implemented and utilized properly, resulting in data with appropriate resolution. Through the use of a high order polynomial function, the data can then be fit to an acceptable curve and the first derivative or the tilt calculated. A simple homogeneous analytic model was also used to analyze this data, applying the England and Green solution[14] to the stress contrasts used for base case #1. The results of this separate test, shown in Figure 28, agreed with base case #1 analyzed here. The next step was to create a model of the B-sand fracture zone consisting of geologic layers derived from a typical gamma log.

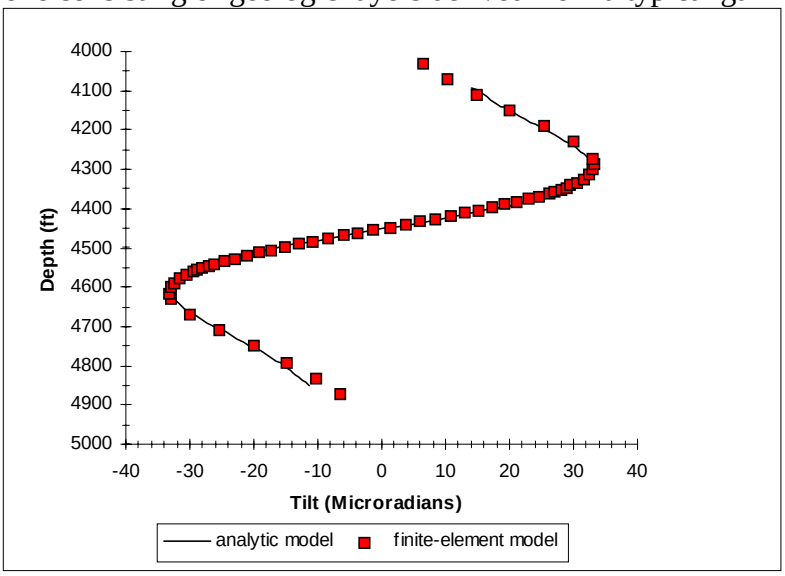

Figure 28. Comparison of finite-element and analytic base case solutions.

6.2 B-Sand Base Case

Initially the gamma log, as shown in Figure 29, was interpreted to support the creation of seven predominant layers within the model. These layers were assigned a thickness and material properties consistent with the gamma log and laboratory core analysis. The values assigned are listed in Table 3. The fracture height modeled was the entire B-sand or 63 feet. The crack width produced is shown in Figure 30 along with the fracture parameters used.

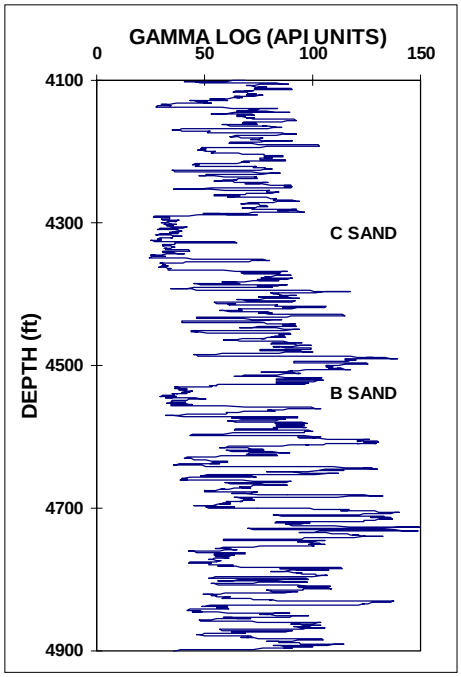

Figure 29. Gamma log of MWX-2 well (treatment well)

Table 3 Rock properties and stress for initial model

		Thickness	Young's Modulus	Poisson's Ratio	In-Situ Stress
		(feet)	(million psi)		(psi)
Region 7	Shale	352	3.0	0.22	4300
Region 6	C-Sand	87	5.25	0.18	2800
Region 5	Shale	80	3.0	0.22	4500
Region 4	Siltstone	39	3.5	0.13	3950
Region 3	Shale	28	2.0	0.28	4500
Region 2	B-Sand	63	4.57	0.20	3000
Region 1	Shale	351	2.4	0.25	4600

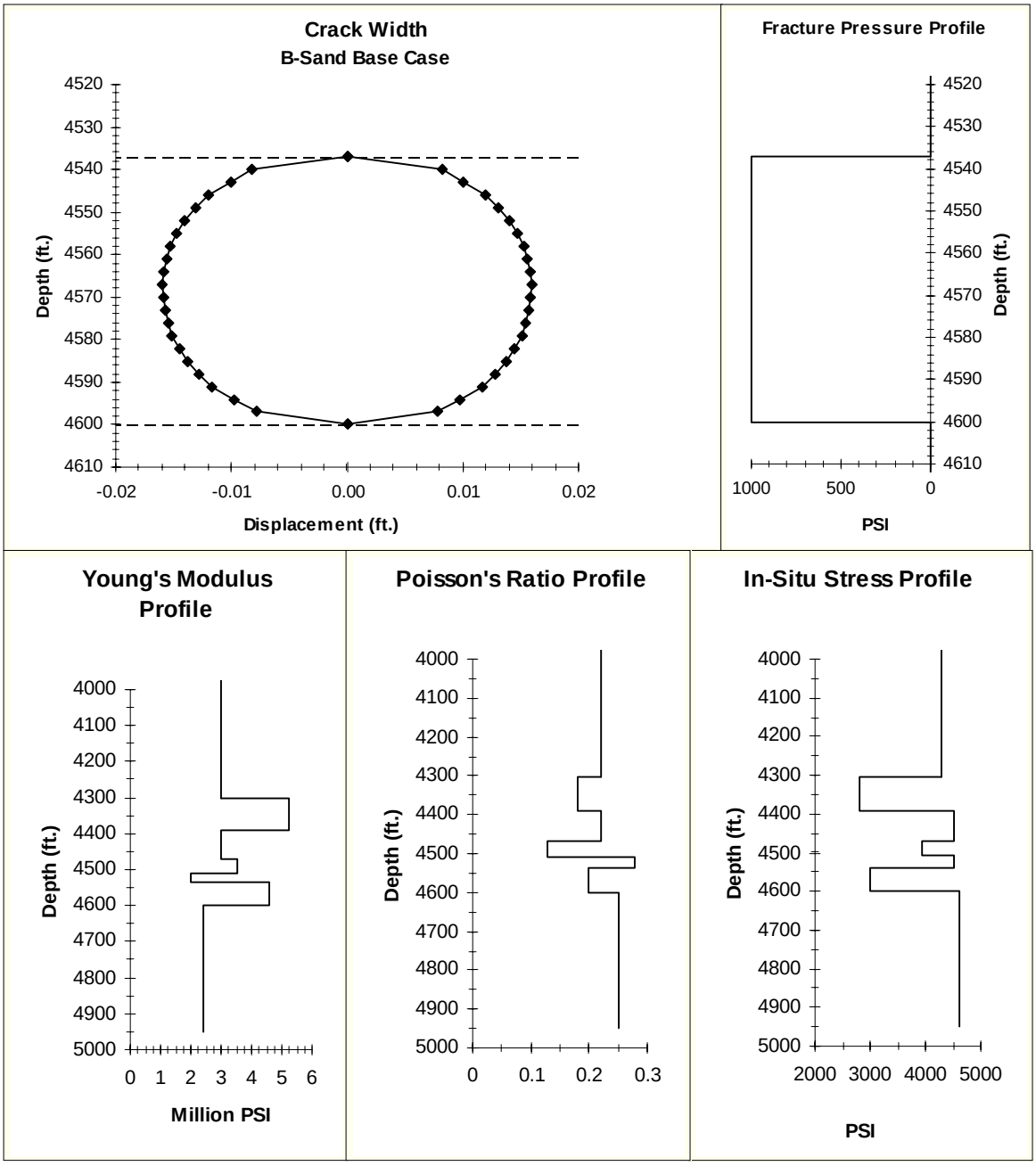

Figure 30. B-sand base case.

Utilizing a fracture pressure of 1000 psi, the tilt produced for this model is shown in Figure 31. When compared to the tilt produced in the homogeneous case, this case provides more character in the tilt field at shallower depths, asymmetric peak amplitudes and a slight shift in the zero crossover point from the center of the B-sand (4568.5 ft.) to approximately 16 feet deeper (4585 ft.).

When the modeled results are compared to the downhole tiltmeter data (also shown in Figure 31), the position and the magnitude of the tilt compares well with the downhole

data, however the character evident in the tilt in the layers above the B-sand does not compare as well. The field data shown are from fracture experiments 5B and 6B which included the use of a linear gel at a fracture pressure of 1700 and 2000 psi respectively. One reason for this discrepancy could be a lack of resolution in the field data due to only six downhole tiltmeters being employed.

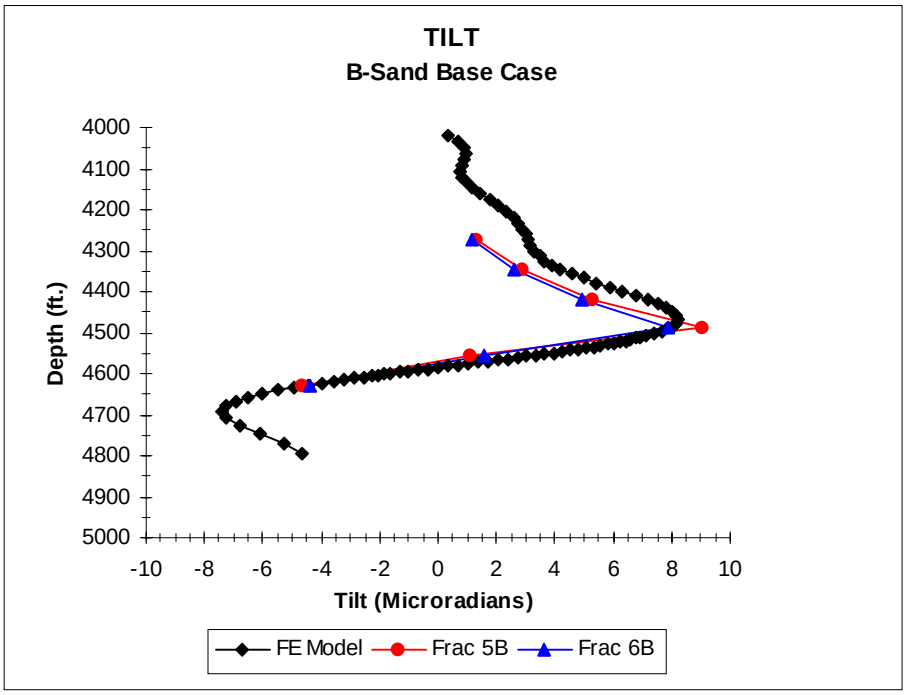

Figure 31. B-sand base case.

Another factor could be that the code itself is a linear isothermal elastic plastic material model which although reasonable for this study may not be the most accurate of rheological models. Real earth materials do not display ideal elastic behavior, although some may approximate to it over a limited range of conditions. The generalized stress-strain relationship for a rock is more likely to take a curvilinear form. Only after the pores and the interstices of the material are closed by the applied pressure will the rock display an approximate linear elastic response which will continue until the onset of internal slip, dislocation and fracture. Therefore some discrepancies may occur due to this application of a linear elastic earth model.

Finally the use of material property values that are not true representations of the in-situ conditions and circumstances could contribute to this discrepancy. The modulus values utilized here were obtained from extensive laboratory studies performed upon core samples taken from the M-Site location and are considered accurate values.[18] However these laboratory static tests do not include the natural fractures found in-situ and may therefore be less compliant than the actual in situ reservoir rocks. The dynamic in-situ measurements are obtained by performing a sonic log which uses a high frequency bandwidth, typically in the 10 to 20 KHz range. These measurements usually provide a

much greater modulus value, typically by a factor of two. Ultrasonic laboratory tests also yield higher values than the statically derived values and are on the same order as the sonic log values. This difference between dynamically and statically derived modulus will be investigated and is discussed in Section 6.4

Also, the shales above the B-sand in Region's 3 and 5 are considered to be very fragile and difficult to analyze. Some adjustment of their properties would be reasonable and could account for this loss of character. As a result of these uncertainties, the effect of varying Poisson's ratio and Young's modulus upon the induced tilt was investigated.

6.3 Poisson's Ratio Effect

Poisson's ratio is a measurement of a material's ability to conduct axial strain to the transverse direction. In an elastic body, if the applied load generates an axial compressive strain then the lateral strain is an elongation. However if the material is constrained, and the element of the material is confined by other elements so that it is not free to deform laterally, then an axial compressive stress will generate lateral compressive stresses. The magnitude of which will depend upon Poisson's ratio for the material and the degree of constraint.

In order to account for the loss of character in the layers above the B-sand, the Poisson's ratio for the three layers directly above the B-sand were arbitrarily increased. The value for Region 4, which is the siltstone like layer was doubled from 0.13 to 0.26. The values for Region's 3 and 5 were not doubled but instead were increased to 0.4. Since water has a Poisson's ratio of 0.5 this upper limit seemed reasonable. The idea tested here is that with an increase in the ability of these layers to transmit the axial stress laterally, a decrease in the magnitude and character of the associated tilt may result.

All other parameters were identical to the B-sand base case previously run, except for this increase in Poisson's ratio in Regions 3-5. The fracture profiles and the resulting crack width are shown in Figure 32.

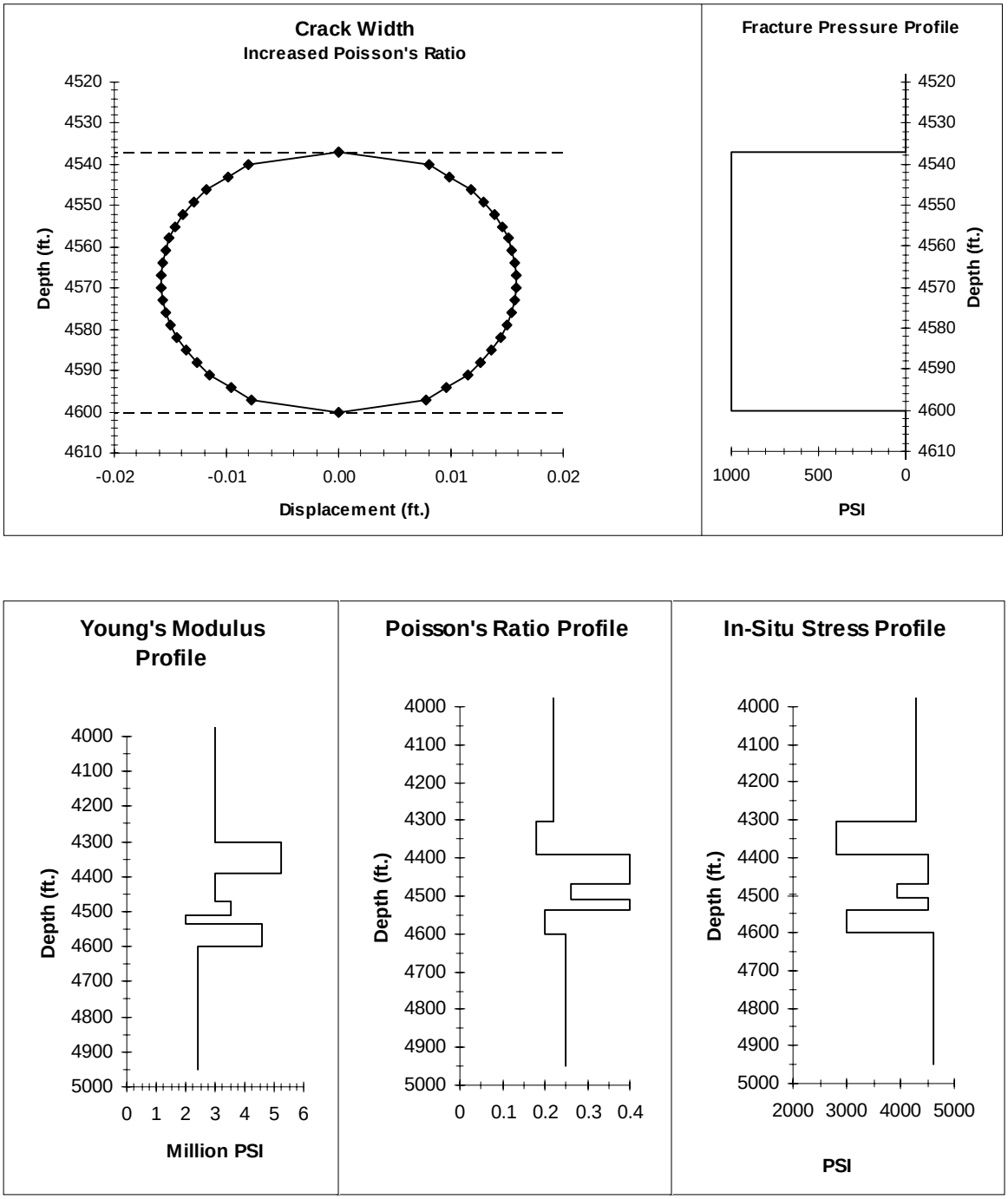

Figure 32. Increased Poisson's ratio.

When the crack width for the two cases are compared, it is evident that no apparent differences occur, as can be seen in Figure 33. More importantly when the tilt produced approximately 300 feet away are compared, only slight differences are evident. There is an increase in the positive peak amplitude from approximately 8.0 to 8.5 microradians and a slight decrease in the amplitude (character) around 4250 feet. The substantial

increase in Poisson's ratio for the three layers above the B-sand does not have any significant effect upon the tilt produced.

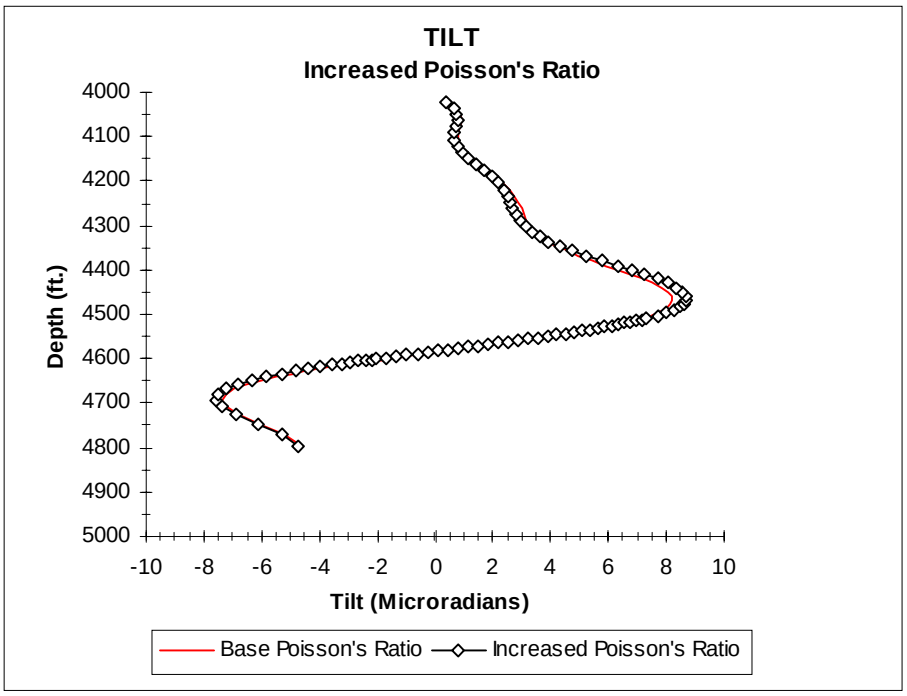

Figure 33. Increased Poisson's ratio.

6.4 Young's Modulus Effect

In a perfectly elastic material, there is an immediate response to an applied load that results in an instantaneous change in dimension directly proportional to the stress generated by that load. In such a material the stress/strain relationship is constant and the ratio of the two is termed "Young's modulus of elasticity". The greater the value for a material, the less will be the deformation produced by a given value of stress and the stronger the material.

For this case, only the moduli in Regions 3 through 5, which are atop the B-sand, were reduced by a factor of 2. All other fracture parameters were set to the values utilized in the B-sand base case. The results of this case are shown in Figures 34 and 35. The crack width has increased in size and become asymmetrical in nature about the center line of the B-sand, as would be expected. In response to this increased width, the tilt has changed significantly in that the positive peak amplitude has increased by about a factor of 2 and the negative (deeper) peak amplitude has also increased by about a factor of 1.5. However the character associated with the layers above the B-sand appears to have remained unchanged. Thus for the present model configuration, the amplitude of the peaks may be adjusted by slightly modifying the modulus of the layers.

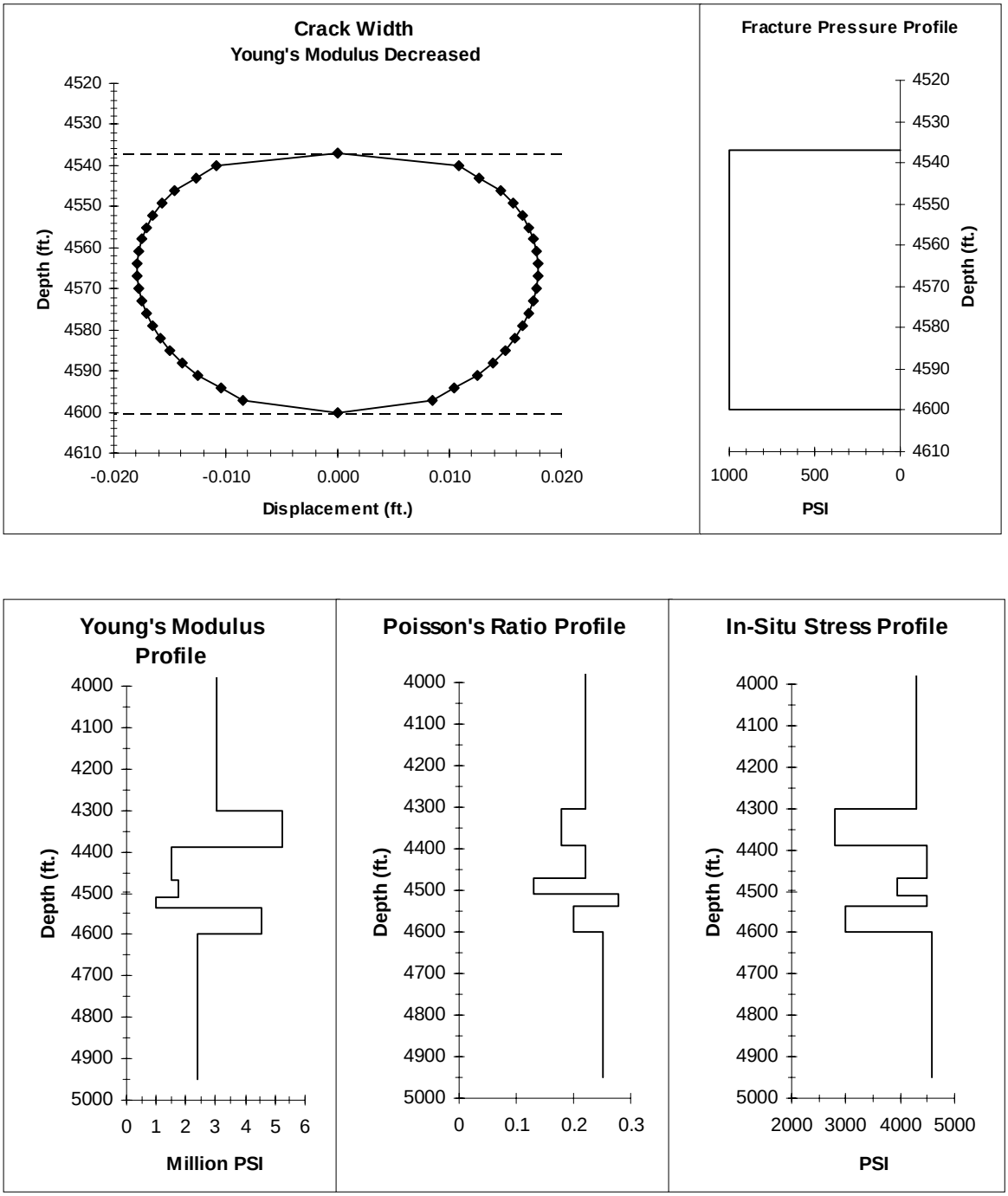

Figure 34. Young's modulus decreased.

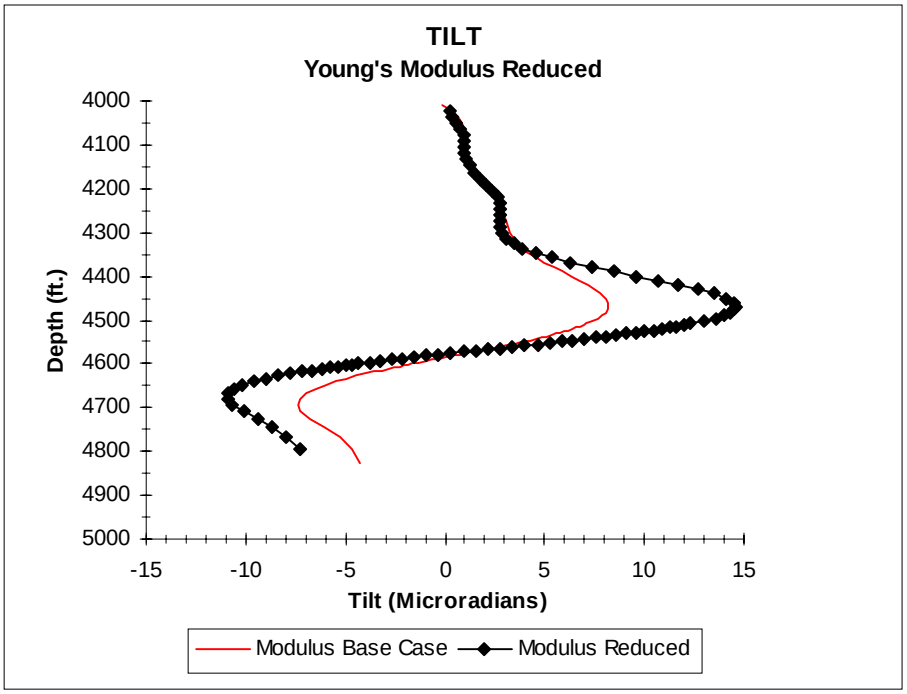

Figure 35. Young's modulus reduced.

In contrast to Poisson's ratio, Young's modulus has a significant effect, at least upon the tilt amplitude produced. As will be seen from comparisons with actual M-Site inclinometer data, this large modulus effect also indicates that the values derived from the laboratory studies are likely accurate and well within the range of the actual in-situ values. If these static values are treated as high by as much as a factor of 2 and subsequently reduced (to account for fractures or other compliant features), then artificially large tilt peak amplitudes will be produced.

An alternate method of determining the modulus is to measure the compressional and shear wave velocities and the rock density, from which elastic constants can be derived. Dynamic moduli determined in this manner from ultrasonic logs are generally a factor of 2 greater than the static moduli and would result in extremely small tilts. However, the method for measuring the velocity structure is important, at least at M-Site, since the modulus values calculated appear to be frequency dependent.

As a result, using a typical crosswell velocity survey which uses a lower frequency bandwidth than logs to determine the velocity structure and a density log as input to an appropriate inversion code, the in-situ Young's modulus can be calculated. From the velocity equations for elastic waves,[19] the following equations yield the Young's modulus based on the compressional (P-wave) or the shear (S-wave) wave velocity.

$$E = \frac{\rho v_s^2 \left(3v_p^2 - 4v_s^2\right)}{v_p^2 - v_s^2} \quad (1)$$

$$G = \rho\, v_s^2 \quad (2)$$

where E is the dynamic modulus of elasticity, G is the shear modulus, v_p is the compressional wave velocity, v_s is the shear wave velocity, and ρ is the density of the material. Poisson's ratio, ν, is similarly given by

$$\nu = \frac{v_p^2 - 2v_s^2}{2\left(v_p^2 - v_s^2\right)} \quad (3)$$

Presently, the modulus calculated by this method is based upon the average velocity and density for a given layer. However since the tomogram can indicate velocity changes within a layer, finer modulus detail could be derived if the inversion code with appropriate constraints interpolated the associated density data. Although the tomogram survey data taken at M-Site indicates lithologic changes within the layers between the wells, only averaged density data is available.

The moduli calculated in the above manner using the crosswell-survey tomogram data were examined and found to be separable into nine discrete layers, which were then used for trial calculations. These low frequency dynamic data are compared to the laboratory measured static data for the layers indicated in Table 4.

Table 4. Tomogram Based Moduli

		Thickness (ft)	Laboratory Young's Modulus (million psi)	Thickness (ft)	Tomogram Young's Modulus (million psi)
Region 9	Shale	352	3.0	315	3.12
Region 8	C-Sand	87	5.25	80	4.02
Region 7	Shale	80	3.0	60	2.92
Region 6	Siltstone	39	3.5	40	3.38
Region 5	Shale	28	2.0	50	2.68
Region 4	B-Sand	63	4.57	50	3.78
Region 3	Shale	65	2.4	100	2.77
Region 2	X-Sand	60	4.5	30	3.79
Region 1	Shale	226	2.4	275	3.13

These data compare very well and indicate that indeed the methodology used to measure the velocity structure is important, at least at M-Site. Using the velocity Tomogram data and the calculated moduli, a nine layer model was constructed and analyzed for

comparison to mini-frac's 5-6B. The fracture parameters indicated in Table 4 for mini-frac's 5-6B were used for both cases except for the modulus and the fracture height as shown in Table 3. The tilt produced as a result of this analysis is shown in Figure 36 and is compared to the measured tilt from the field tests as well as calculated tilt produced from the mini-frac's 5-6B analysis.

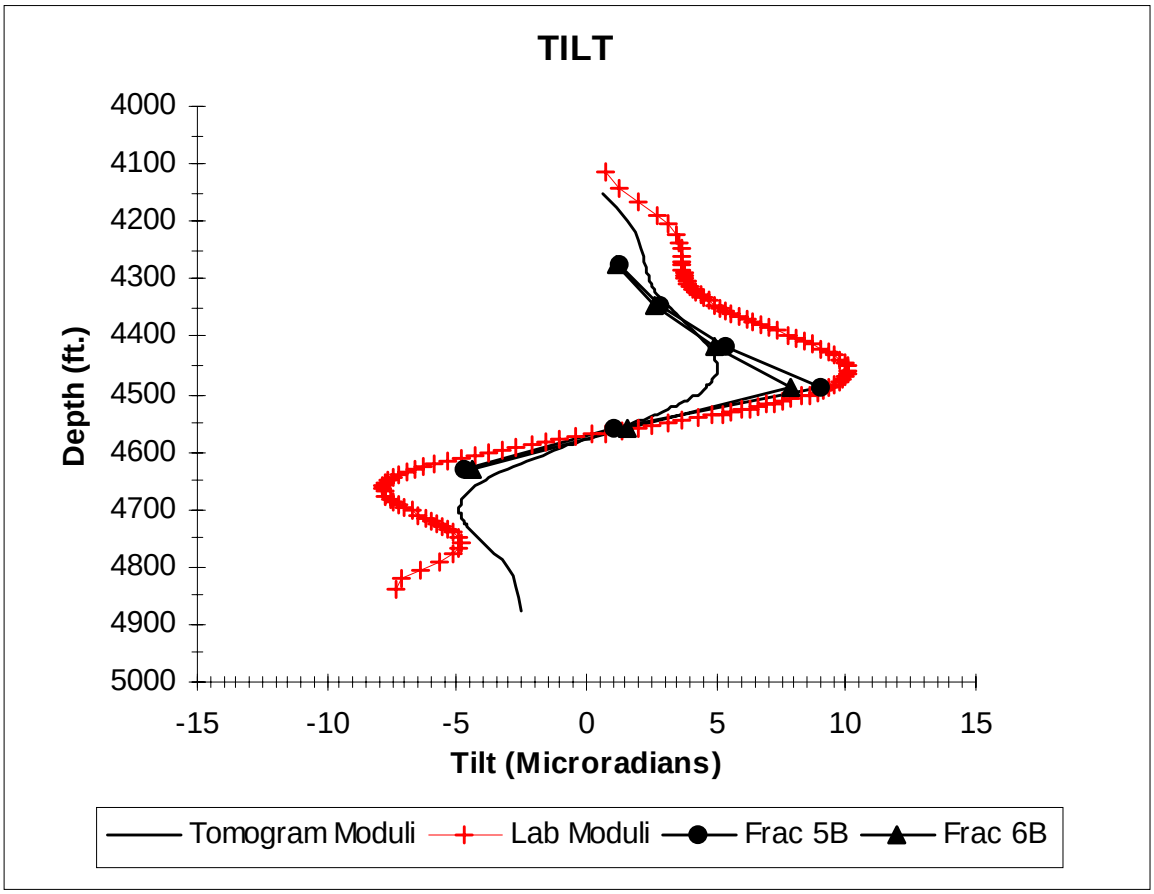

Figure 36. Dynamic Tomogram Moduli versus Static Laboratory Moduli

The curves defined by the triangular symbols are the measured results from the six inclinometers installed at M-Site for mini-frac's 5-6B. The curve showing a maximum positive tilt of approximately 10 microradians comes from the nine layer analysis based on the gamma logs and the laboratory derived moduli. The lower curve shows the results of the analysis based on the Tomogram velocity structure and the calculated moduli. Although this curve does not provide as good a match to the field data as the static based curve, it does show some promise.

The loss of character and smearing that is evident can be attributed to the modulus calculation that is based upon average density and velocity data. The typical inversion procedure performed on the crosswell tomographic dataset applies a zeroth derivative function to the near borehole cell velocity which is then used as a reference. This cell velocity can be weighted thus supplying primarily borehole model constraints. The cells

between the boreholes are then allowed to float and their velocities are calculated based upon raypath traveltime within the established constraints. An improved modulus calculation could be obtained if more accurate velocity and density data were incorporated. For the velocity data this may be possible by using an iterative tomographic procedure that includes finite-difference traveltimes and constraint information in the form of horizontal and vertical first-difference regularization[20].

Unfortunately only average density data were available, however a borehole gravity meter log would potentially provide a more detailed density dataset. With the inclusion of both of these datasets, a more accurate modulus could be calculated and therefore a better match to the field data obtained.

Because of the smeared nature of these modulus results, it was decided that using the gamma log to define lithology and the core-based static moduli for properties was the more appropriate methodology.

6.5 Fracture Height and Pressure Effect

So far the cases that have been analyzed, which agree with the field data better than the analytic model, have only utilized a fracture pressure of 1000 psi and a fracture height equal to the B-sand (63 feet). The next set of experiments varied these two parameters as shown in Table 5, in order to compare the results from several field mini-frac's with the results from the finite element model.

Table 5. Variations in pressure and fracture height

	Fracture Pressure (psi)	Fracture Height (ft)
KCl Water 3-4B	1000	45
	1000	55
	1000	63
	1000	100
Mini-Frac 5-6B	1300	45
Linear Gel	1300	55
	1300	63
	1300	100
Mini-Frac 7B	2000	45
CrossLinked Gel	2000	55
	2000	63
	2000	100

The values used for the in-situ stress, Poisson's ratio and Young's modulus are the same values as previously used (Table 3). The values for the fracture pressure and the fracture height were chosen to bracket the values measured in the field. The fracture pressure was measured real-time with a downhole pressure tool and the fracture height was measured microseismically with an advanced 5-level borehole tool. Table 6 indicates the results of these measurements.

Table 6. Measured fracture pressure and height

	Fracture Pressure (psi)	Fracture Height (ft)
KCl Water Fracs 3-4B	1000	55
Mini-Fracs 5-6B (Linear Gel)	1300	75-80
Mini-Frac 7B (Cross-Linked Gel)	2000	135

Figure 37 compares the modeled results to the data gathered for the KCl water injection. In this case the fracture height was varied as indicated above while using a fracture pressure of 1000 psi. Figure 38 compares the modeled results to the linear gel mini-frac 5B and 6B. Here the fracture pressure of 1300 psi was used as the fracture height was varied. The crosslinked gel mini-frac 7B is compared to the modeled results in Figure 39. The fracture pressure for this case was 2000 psi as the fracture height was varied accordingly. The results of these cases show the ability of the finite element analysis to model the experimental field data.

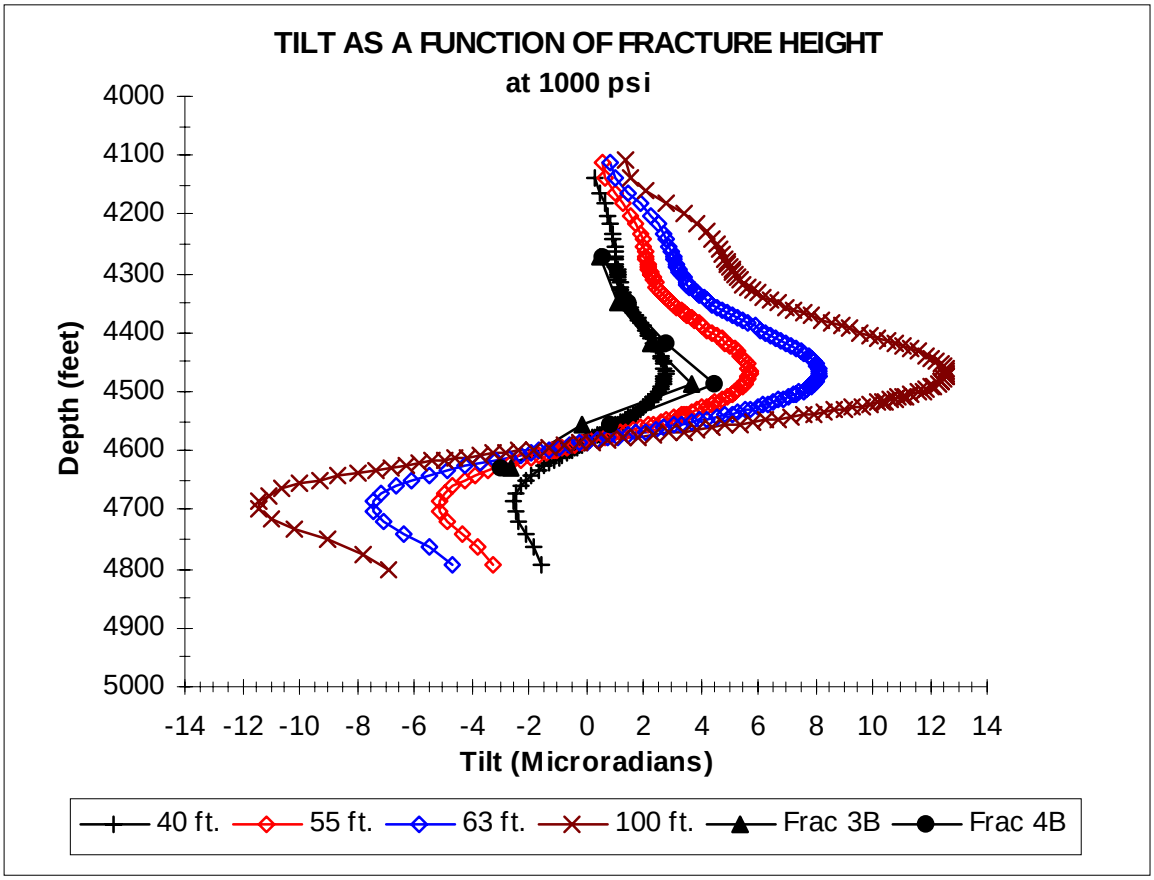

Figure 37. Tilt as a function of fracture height at 1000 psi.

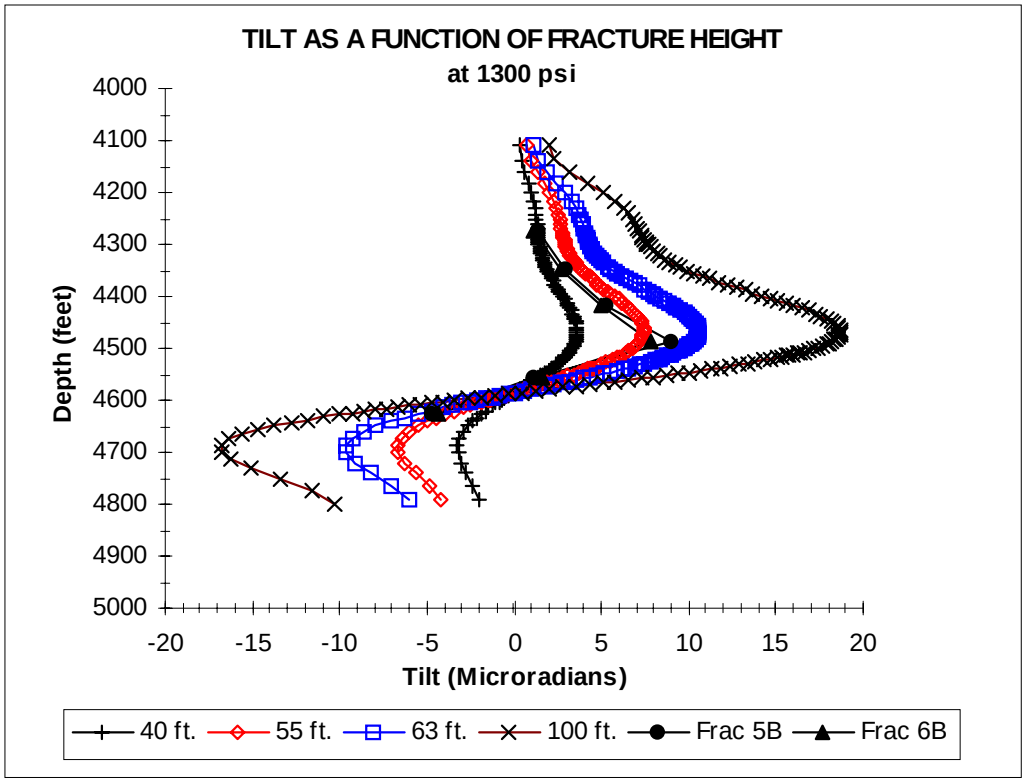

Figure 38. Tilt as a function of fracture height at 1300 psi.

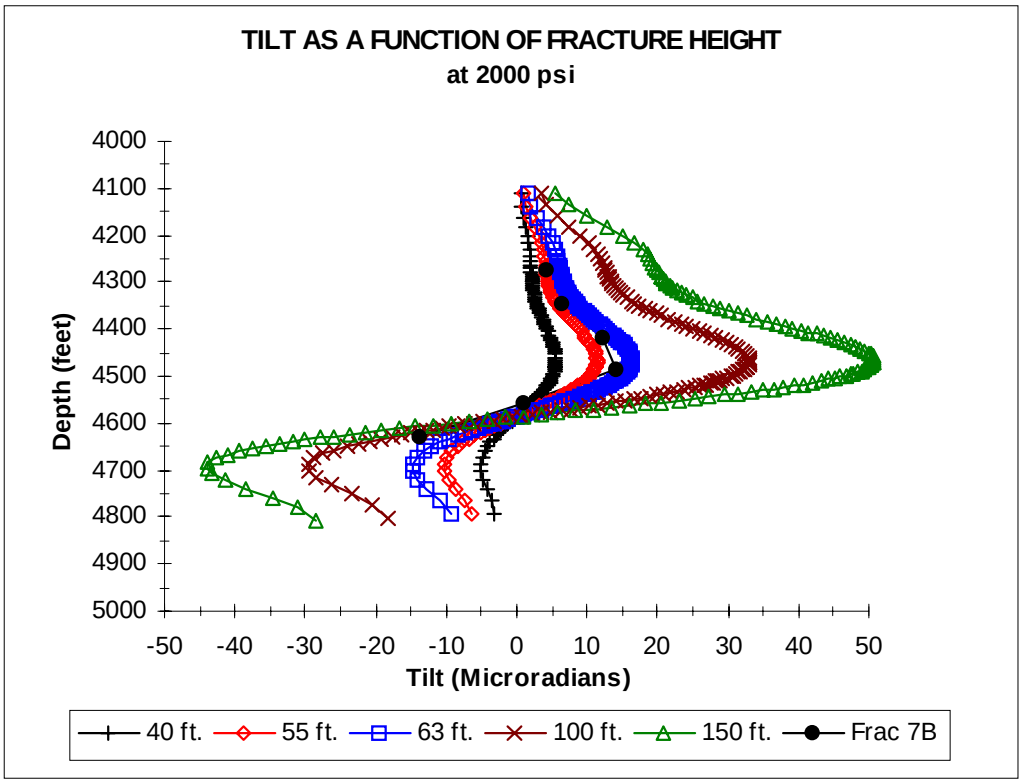

Figure 39. Tilt as a function of fracture height at 2000 psi.

The tilt produced as a function of fracture height for several fracture pressures bracket the field tiltmeter data nicely and are considered to be in good agreement between the field and modeled data. These results are consistent with the results from the earlier base cases run, in specific peak positions, general peak amplitudes and the character observed. However, several important differences are evident; 1) The modeled zero crossover point is approximately 16 to 18 feet deeper than in the field data. 2) When the fracture pressure is increased to 2000 psi, the agreement between what fracture height is needed to produce the appropriate tilt decreases. The field data indicates that a fracture height of 135 feet produced a measured tilt of around 15 microradians while the model suggests that only 63 foot fracture height is needed. However Fracture 7B utilized a crosslinked gel producing an asymmetric wing height profile of 100 - 150 feet high by 150 feet long followed by a section 80 - 63 feet high and 250 feet long. There may also have been a significant near field pressure drop produced in this particular fracture experiment due to the use of a crosslinked gel and a 2000 psi fracture pressure. The present analysis assumes that the defined fracture height is uniform for the length of the fracture and the pressure is applied in a linear fashion along the plane of the fracture. Another possibility is that the tiltmeter responds to an average fracture height in this complex configuration. If the input varies as a function of cosine squared then the calculated average height that the tiltmeter responds to is 79 feet. Although the character in the tilt produced at the shallower depths is evident in the field data, the model tends to over estimate the magnitude. A model that includes finer layering detail, along with the appropriate material properties may account for this over estimation. Since the elastic moduli are interdependent and the tilt produced is dependent not only upon these moduli but also upon the fracture height and pressure, a large number of possible combinations could exist that would provide a closer fit. This is beyond the scope of this study, so measured and laboratory values will be used.

6.6 Zero Crossover Shift

The shift in the depth at which there is zero tilt could be explained by; 1) inappropriate modulus values or combinations, 2) placing the fracture itself in the wrong location within the model, 3) the layering of the B-sand or the areas surrounding it are not detailed enough. A few different combinations were run in which the Young's modulus of the layers adjacent to the B-sand were varied. Again the tilt amplitude changed proportionally with modulus variation and only a slight change in the slope at the crossover point was apparent. While some minor correction is possible with the technique, it is not the sole answer.

The center line of the fracture as it is presently modeled coincides with the center line of the B-sand. The center line of the fracture was then shifted upwards by 18 feet within the B-sand. The overall height of the fracture was maintained resulting in the fracture also involving Region 3 which is above the B-sand. Due to the inclusion of this higher in-situ stressed region, the overall amplitudes decreased and the peak position changes accordingly. No significant change in the zero crossover point occurred. Finally the effect of layering detail was investigated.

6.7 Building the Final 2D Mesh

6.71 B-Sand Separation

After close examination of the gamma log in the area of the B-sand and the surrounding regions, support was present for the separation of the B-sand into additional layers. Instead of a continuous 63 foot sand layer, the new configuration would be two sand layers with a six foot shale layer in between. The properties assigned to this layer arrangement are given in Table 7.

Table 7. Nine Layer Model

		Thickness (ft)	Young's Modulus (million psi)	Poisson's Ratio	In-Situ Stress (psi)
Region 9	Shale	352	3.0	0.22	4300
Region 8	C-Sand	87	5.25	0.18	2800
Region 7	Shale	80	3.0	0.22	4500
Region 6	Siltstone	39	3.5	0.13	3950
Region 5	Shale	28	2.0	0.28	4500
Region 4	B-Sand	39	4.57	0.20	3000
Region 3	Shale	6	3.0	0.25	4200
Region 2	B-Sand	18	4.57	0.20	3000
Region 1	Shale	351	2.4	0.25	4600

Since the primary objective of this study is to model the minifracs, the decision was made to change the focus to Fracture 5B and 6B in which a linear gel was used and a simpler wing configuration was produced. Utilizing the fracture parameters stated above in Table 7, along with a pressure of 1300 psi and a 63 foot height a new case was analyzed. The results of this analysis are shown in Figures 40 and 41.

The crack width indicates the change in deformation due to the inclusion of a new layer at a higher in-situ stress value. The tilt produced when the B-sand is separated has a decreased peak amplitude resulting in a better match with the peak measured during fracture 5B. However the shift in the zero crossover point has remained unchanged. Also while the character produced has decreased slightly in overall amplitude, it still contains the appropriate slope characteristics of the field data.

These trends are in the correct direction for producing a better fit to the field data and as such the B-sand separation will be incorporated into the model. However the shift in the zero crossover point cannot be accounted for and re-examination of the geology was conducted to determine if additional lithologic complexity was needed.

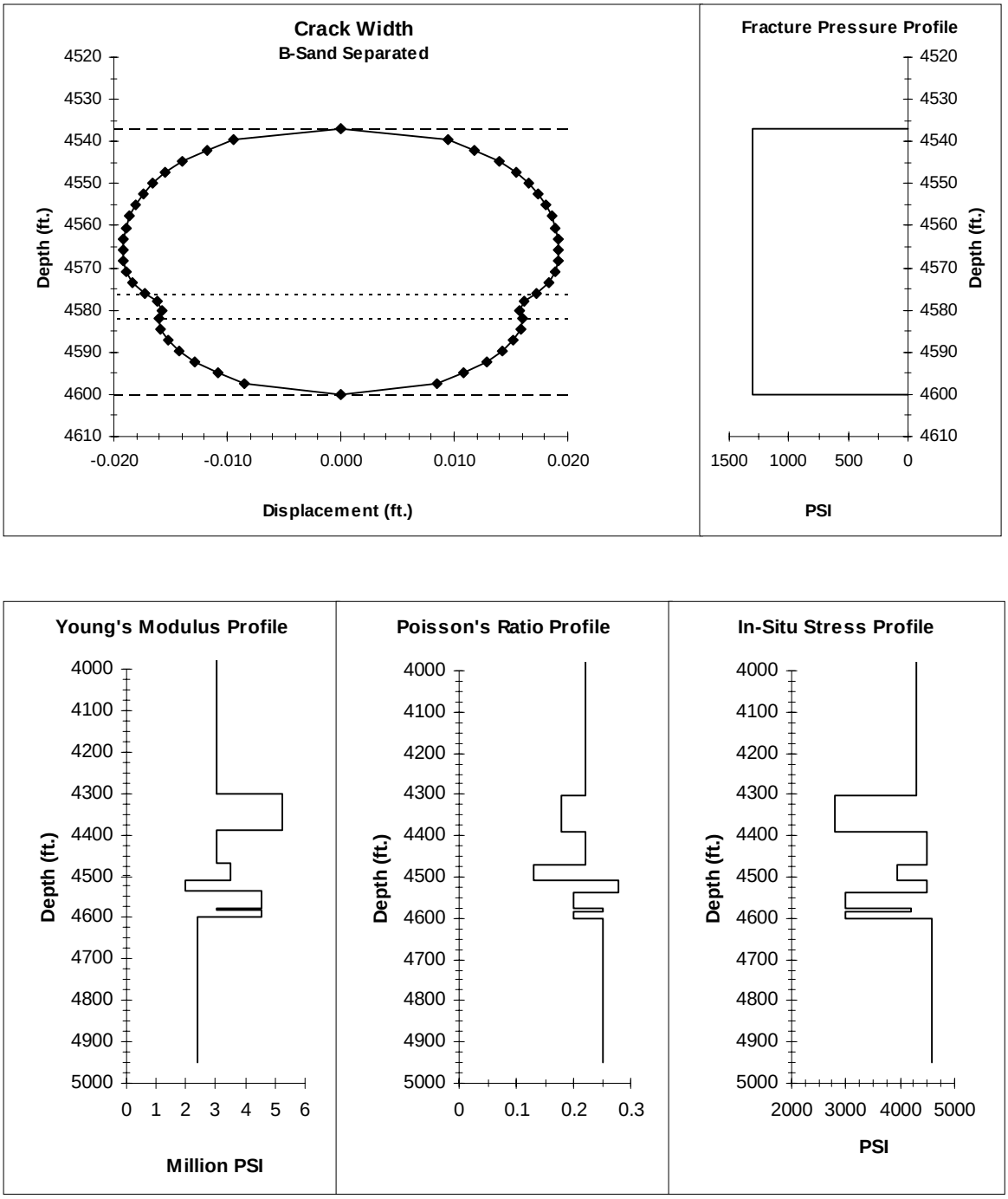

Figure 40. B-sand separation.

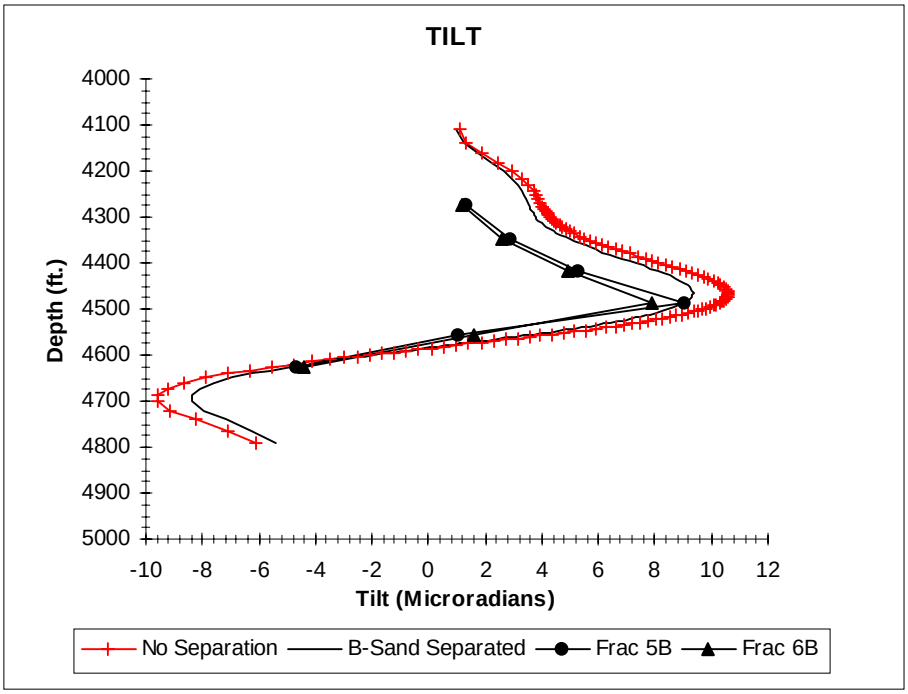

Figure 41. B-sand separation.

6.72 X-Sand Addition

The present model has treated the area below the B-Sand as one uniform shale region. The material properties assigned are typical of the shale properties used in this analysis. However the gamma log clearly supports the separation of this area to include an additional sand-like region that will be referred to as the X-Sand. Initially the separation of the B-Sand was eliminated and only the addition of the X-Sand was incorporated into the model. This was done to isolate the effect that this addition would have on the model. The properties used in this nine layer model are given in Table 8.

Table 8. Layer parameters for X-sand addition

		Thickness (ft)	Young's Modulus (million psi)	Poisson's Ratio	In-Situ Stress (psi)
Region 9	Shale	352	3.0	0.22	4300
Region 8	C-Sand	87	5.25	0.18	2800
Region 7	Shale	80	3.0	0.22	4500
Region 6	Siltstone	39	3.5	0.13	3950
Region 5	Shale	28	2.0	0.28	4500
Region 4	B-Sand	63	4.57	0.20	3000
Region 3	Shale	65	2.4	0.25	4600
Region 2	X-Sand	60	4.5	0.20	3200
Region 1	Shale	226	2.4	0.25	4600

The results of the crack width produced and the fracture parameters used are shown in Figure 42.

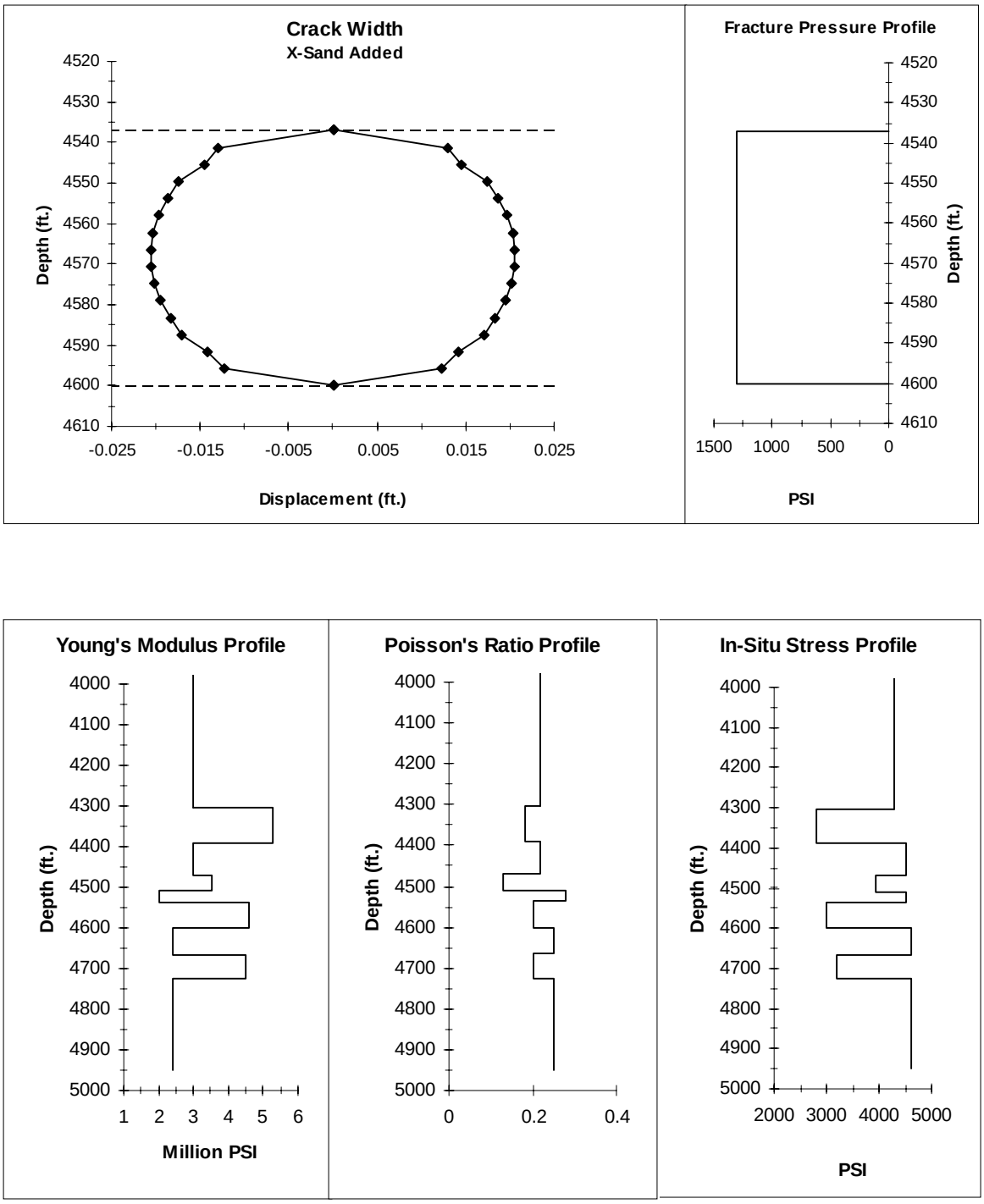

Figure 42. X-Sand addition.

The resultant tilt produced in this case is shown in Figure 43. The significant factor of this case is that the zero crossover point has been shifted to the same point found in the field data. There is also a slight shift of the positive tilt peak and a more pronounced shift of the negative peak to shallower depths. The positive peak has decreased in amplitude from the base case shown in the figure but is higher in amplitude than the peak produced by the separation of the B-Sand alone (Figure 41). Additionally the character has become more pronounced at the shallower depths (4200-4300 feet) and no longer appears to contain the appropriate slope characteristics. The next case to be analyzed would include the combination of the separation of the B-Sand with the addition of the X-Sand.

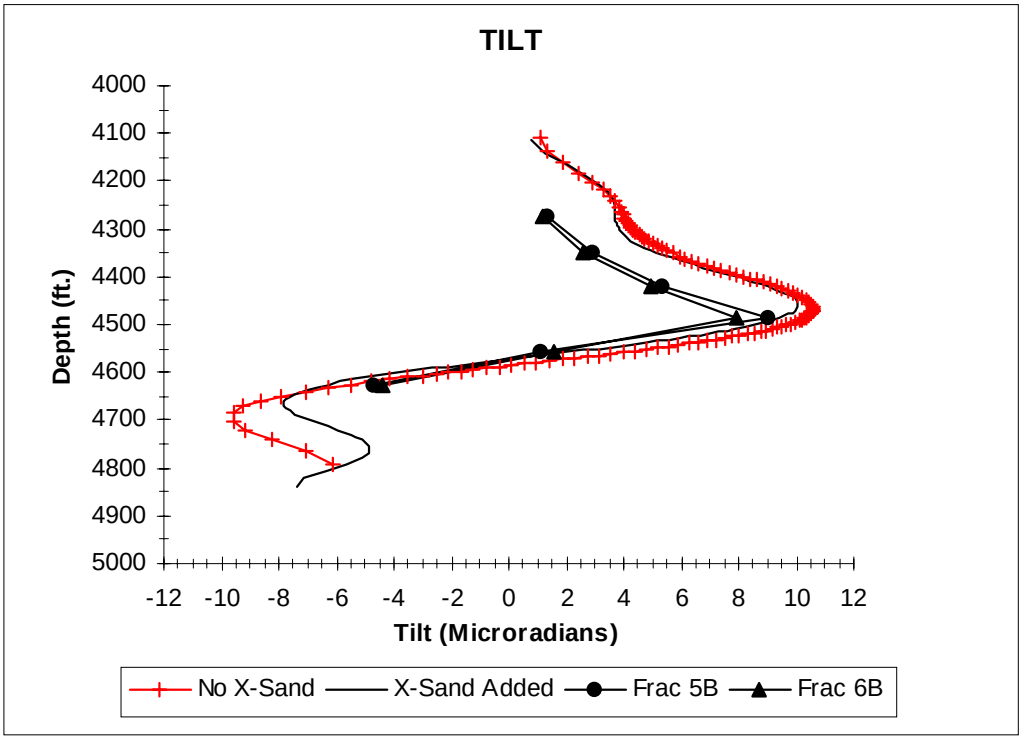

Figure 43. X-Sand addition.

6.73 B-Sand Separation and X-Sand Addition

The model now incorporates eleven layers. The material property values utilized for these layers are given in Table 9.

Table 9. Eleven-layer model

		Thickness (ft)	Young's Modulus (million psi)	Poisson's Ratio	In-Situ Stress (psi)
Region 11	Shale	352	3.0	0.22	4300
Region 10	C-Sand	87	5.25	0.18	2800
Region 9	Shale	80	3.0	0.22	4500
Region 8	Siltstone	39	3.5	0.13	3950
Region 7	Shale	28	2.0	0.28	4500
Region 6	B-Sand	39	4.57	0.20	3000
Region 5	Shale	6	3.0	0.25	4200
Region 4	B-Sand	18	4.57	0.20	3000
Region 3	Shale	65	2.4	0.25	4600
Region 2	X-Sand	60	4.5	0.20	3200
Region 1	Shale	226	2.4	0.25	4600

As expected with the B-sand separated and the X-sand added, the crack width produced resembles the crack width produced by the separation of the B-sand alone (Figure 42). These results are shown in Figure 44.

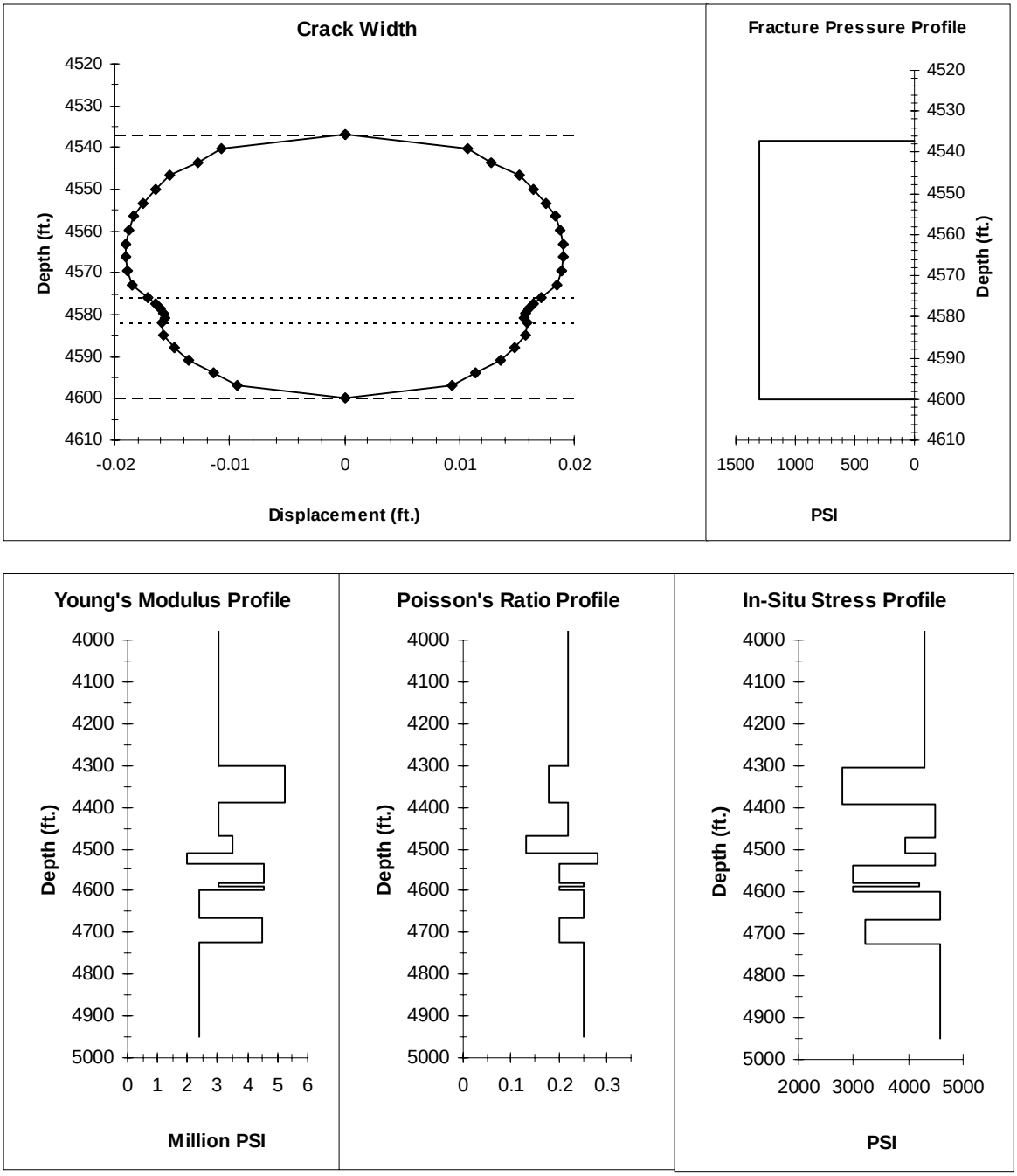

Figure 44. B-sand separation and X-sand addition.

The tilt produced, as shown in Figure 45, is now a combination of the two previous tilts. The zero crossover point has been shifted to the correct position due to the inclusion of the X-sand and the peak amplitude has been reduced due to the B-sand separation. The character of the tilt at the shallower depths has changed again, producing an improvement over the previous case but yielding an area of concern around 4275 feet. The difference in this zone may be explained by the lack of resolution in the field data

due to the limited number of tiltmeters in this region or the lack of detail in the model within this area.

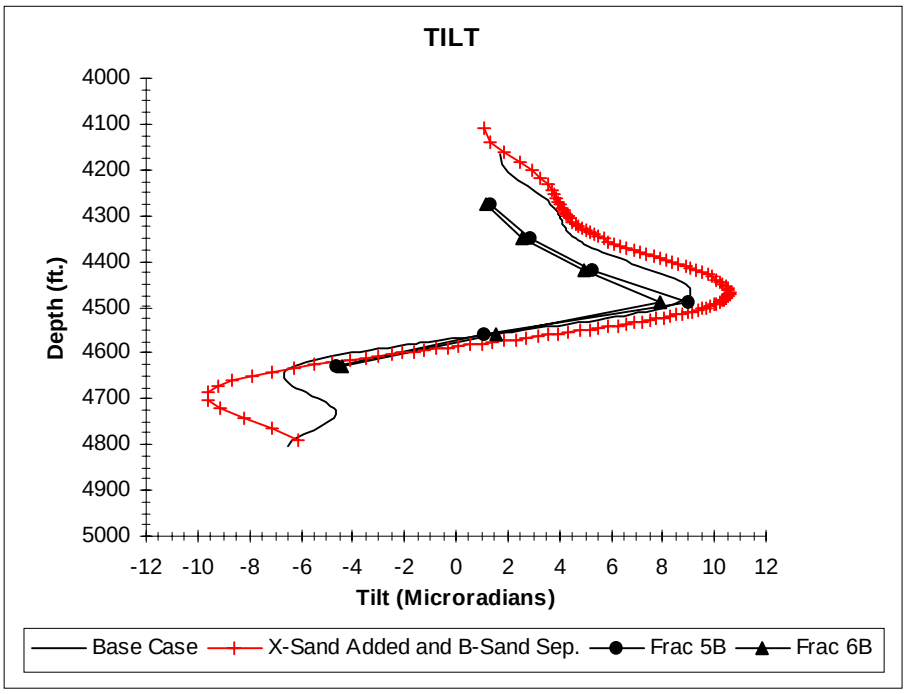

Figure 45. B-sand separation and X-sand addition.

In order to obtain the best fit to the tiltmeter data, several additional cases were run in which the moduli for different layer combinations were adjusted either up or down, the fracture height was decreased from 63 feet to 55 feet, and the thickness of the B-sand/shale separation was modified. The results of the moduli adjustment tests remained consistent with earlier cases in which the modulus was changed. The change in the peak amplitude was inversely proportional to the change in the modulus. However the factor with which the amplitude changed could be controlled to a fashion by increasing a layer(s) while decreasing another layer(s). Another effect of this combined variation but to a much smaller degree, is that the peak position can be shifted on the order of approximately 10 feet.

By decreasing the fracture height, the overall amplitude of the tilt decreases as seen before This effect can be used in conjunction with the variation of the moduli to achieve a better fit. However a great deal of time and effort can be spent attempting to determine what acceptable modulus values should be used together with what layers and at what fracture height. An inversion code that would automate this process would be very useful but this code is not available at this time. For this study the static-modulus values presently used are acceptable and produce a reasonable fit to the field data.

Next the thickness of the layers produced by the B-sand separation were changed slightly. The values chosen still maintain a total thickness of 63 feet but are now;

Region 4 B-Sand 12 feet
Region 5 Shale 8 feet
Region 6 B-Sand 43 feet

The results of this adjustment were minor but considered to be an improvement. The peak amplitude, width and position appear to match better. Again the gamma log was examined for any additional layers that could be included.

6.74 Z-Sand Addition

The search of the gamma log was confined to the area around the C-sand and above. Region 11 in the model which was also treated as one continuous shale zone, was found to contain a sand layer approximately 20 feet thick. This new layer was called the Z-sand. The reasoning for the incorporation of this layer into the model is: 1) this layer may improve the tilt character match in the above mentioned 4275 foot range and 2) any modeling done for the C-Sand fracture experiments would certainly include this layer. Thus the model now contains 13 layers and the properties for these layers are given in Table 10.

Table 10. Thirteen-layer model

		Thickness (ft)	Young's Modulus (million psi)	Poisson's Ratio	In-Situ Stress (psi)
Region 13	Shale	189	3.0	0.22	4300
Region 12	Z-Sand	20	4.5	0.20	2800
Region 11	Shale	143	3.0	0.22	4300
Region 10	C-Sand	87	5.25	0.18	2800
Region 9	Shale	80	3.0	0.22	4500
Region 8	Siltstone	39	3.5	0.13	3950
Region 7	Shale	28	2.0	0.28	4500
Region 6	B-Sand	43	4.57	0.20	3000
Region 5	Shale	8	3.0	0.25	4200
Region 4	B-Sand	12	4.57	0.20	3000
Region 3	Shale	65	2.4	0.25	4600
Region 2	X-Sand	60	4.5	0.20	3200
Region 1	Shale	226	2.4	0.25	4600

The addition of the Z-sand proved to be the last step in the finalization of the 2-D model. The properties given in Table 10 were determined to be reasonable values that formed the basis for any further analysis. The results of the crack width and the tilt produced for a 63 foot fracture at 1300 psi are shown in Figures 46 and 47.

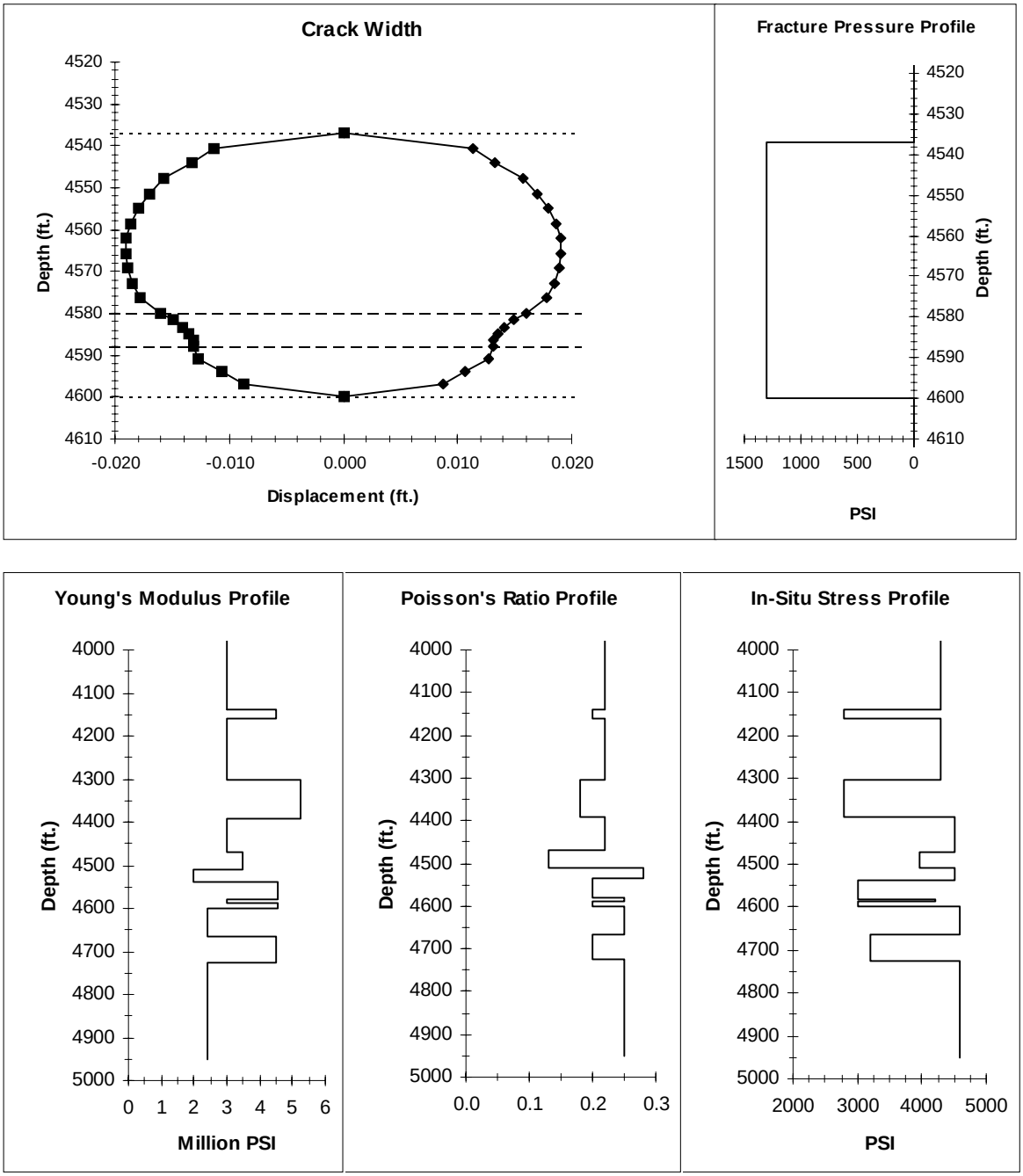

Figure 46. Z-sand addition.

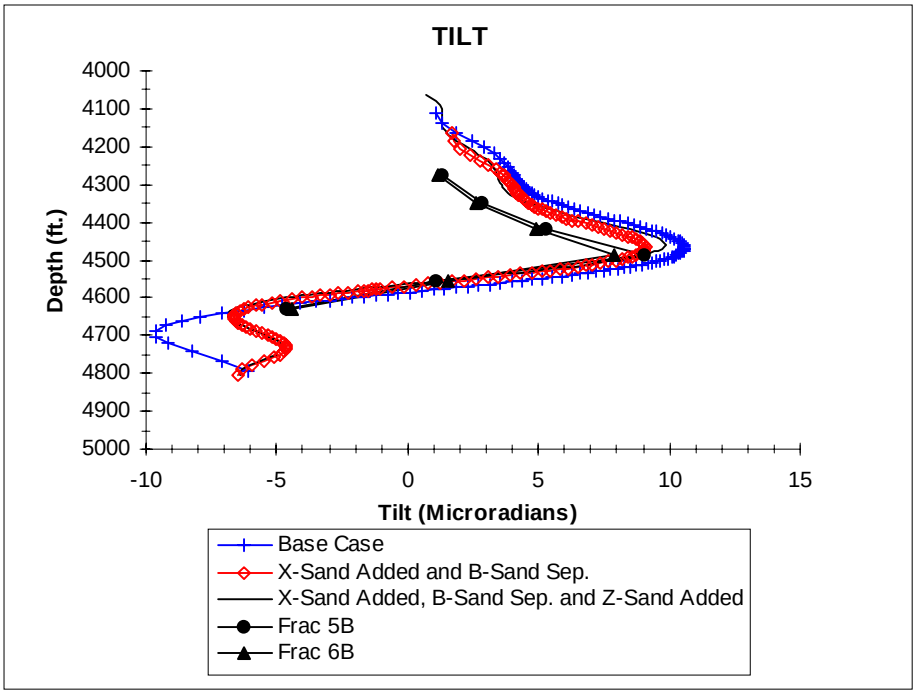

Figure 47. Z-sand addition.

As shown in Figure 47, the final tilt produced is a reasonable representation of the tiltmeter field data. Several factors are evident: 1) with the Z-sand added the positive peak amplitude has increased from the maximum obtained in the previous case, 2) the peak width has been narrowed slightly resulting in the slope characteristics of the peak better approximating the field data, 3) an improvement in the tilt detail at the 4275 foot range, 4) the overall breadth of the positive tilt is still too large resulting in apparently high values at the shallower depths (4250-4450 ft.). Although further improvements upon the tilt produced can potentially be made by analyzing different combinations of layer thickness and modulus values, for the purpose of this study the present model clearly verifies the correlation of the tiltmeter data and the seismic data.

With the 2-D model finalized, a few additional cases were conducted in which the fracture height alone was varied for a fracture pressure of 1300 psi. The results of these analyses, shown in Figures 48-51, bracket the Fracture 5B and 6B field data and by interpolation yield the best possible fracture height scenario for this given pressure, as seen in Figure 52.

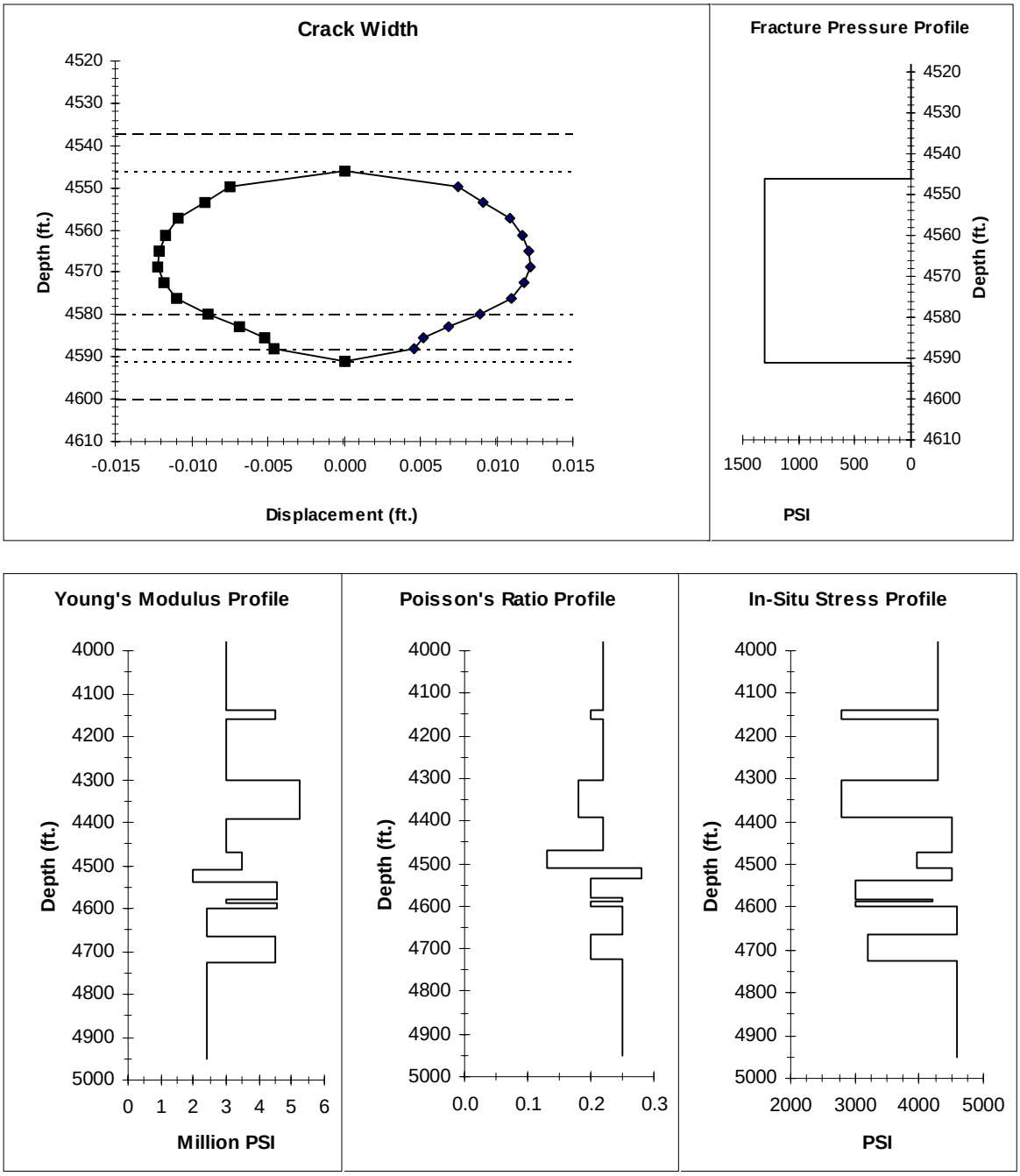

Figure 48. 45-foot fracture height.

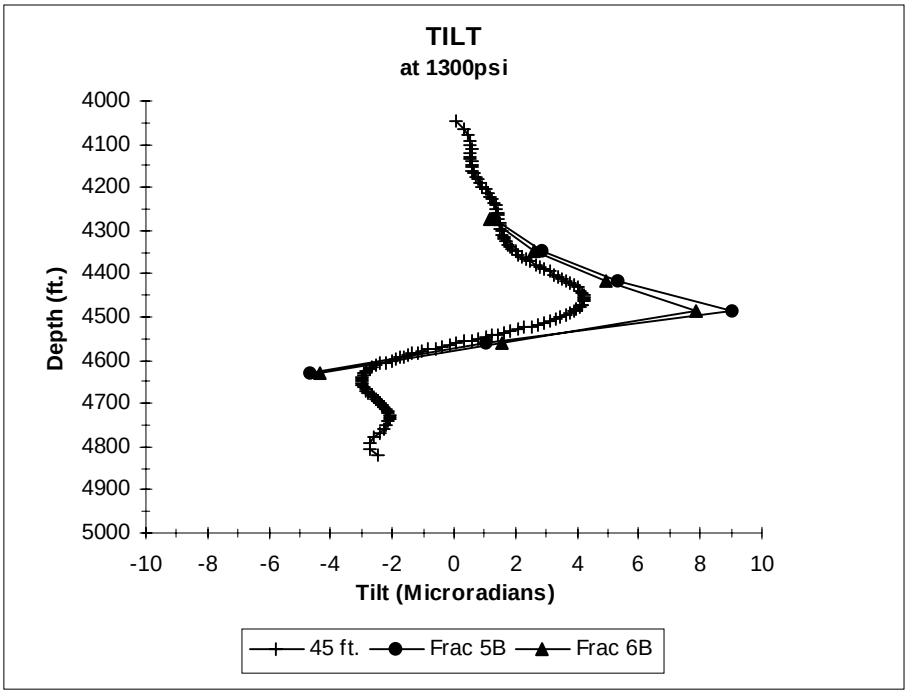

Figure 49. 45-foot fracture height.

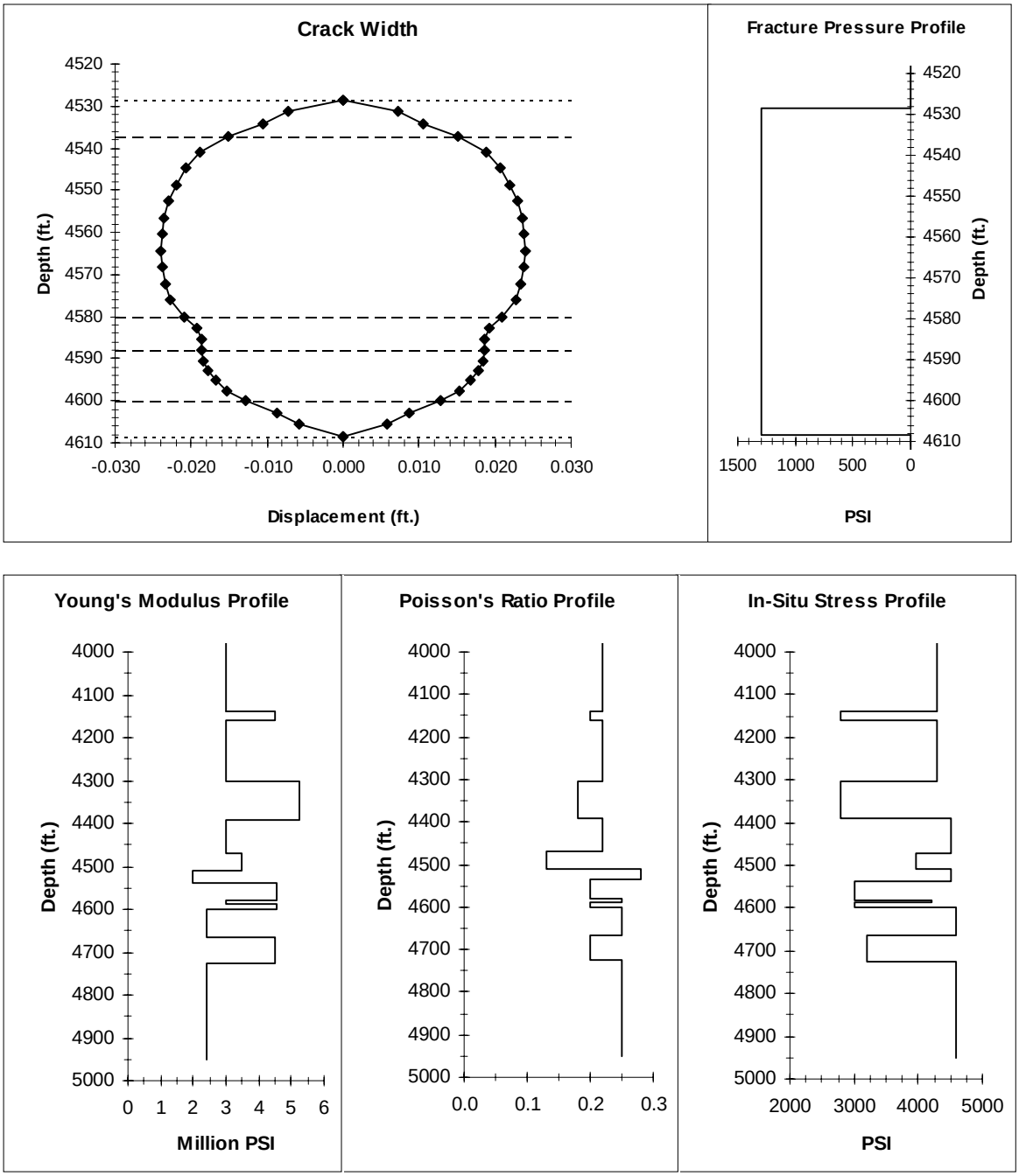

Figure 50. 80-foot fracture height

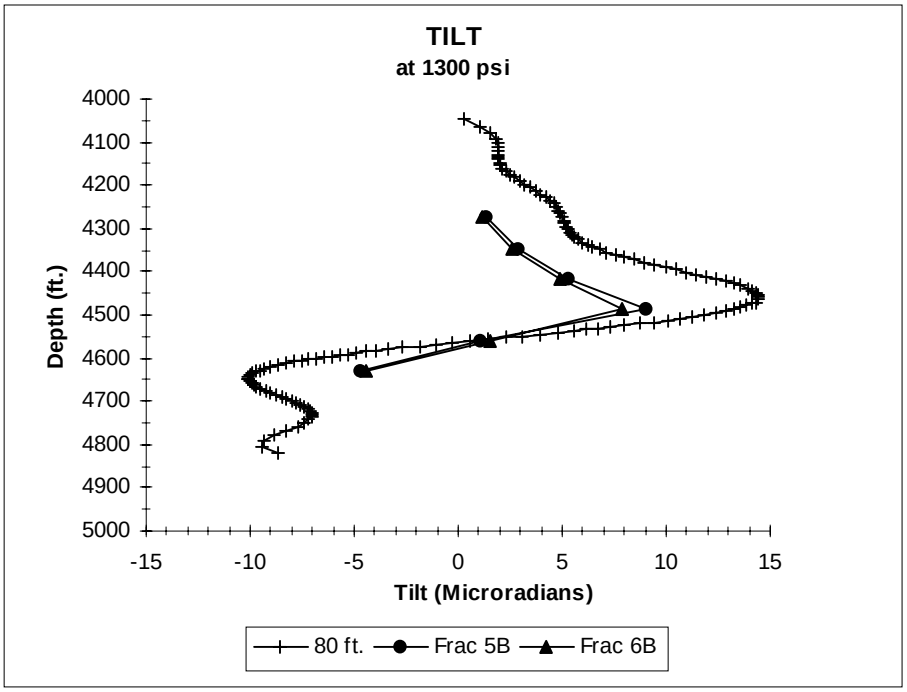

Figure 51. 80-foot fracture height.

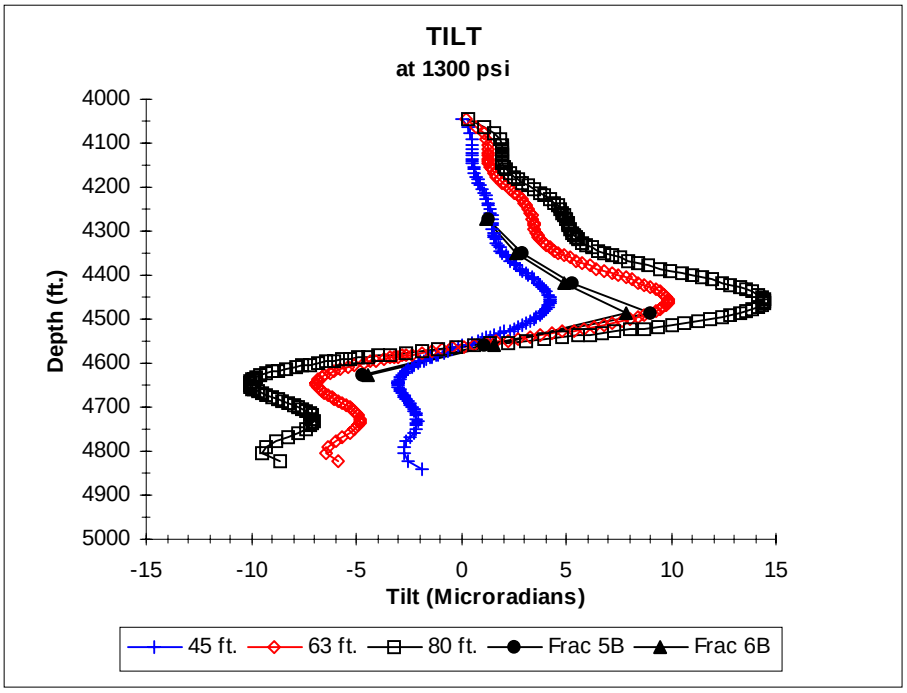

Figure 52. Fracture height variation at 1300 psi

6.8 Fracture Height Versus Tilt Versus Fracture Pressure

Within the B-sand, several minifracs were conducted using different fluids, rates and volumes, resulting in significantly different fracture pressures. Fractures 3B and 4B were KCl water calibration injection tests injected at 1000 psi, fractures 5B and 6B were linear gel minifracs achieving 1300 psi, and fracture 7B was a crosslinked-gel/sand fracture treatment performed at 2000 psi. Utilizing the final 2-D model, numerous cases were analyzed in which the fracture height was set at 45, 63 and 80 feet for each of the following fracture pressures: 1000 psi, 1300psi, 1700 psi and 2000 psi. For each of these fracture pressures, the modeled tilt produced at the depth corresponding to tiltmeter #4 (4487 feet) was plotted as a function of the fracture height, as given in Figure 53. For each of the field experiments, the tilt measured at this same depth is indicated by a vertical line and labeled with the fluid used.

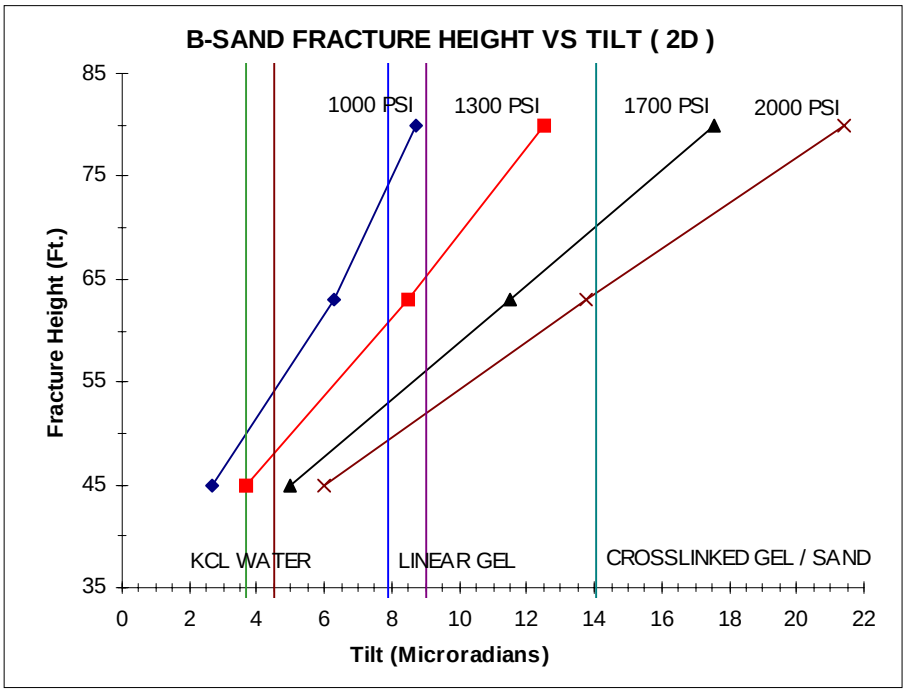

Figure 53. Fracture height vs. tilt vs. fracture pressure.

This plot supplies several pieces of information. Most importantly, for a given tilt and fracture pressure measured during the fracture process of the B-sand, the fracture height necessary to produce such tilt can be derived. For example, a tilt of 4 microradians at 4487 feet in conjunction with a fracture pressure of 1000 psi would require a fracture height of approximately 53 feet. For the purpose of this study, one use of this number would be to compare this value with the value generated by the microseismic diagnostic systems in order to independently verify the microseismic results and thereby develop confidence in the field system. Another use would be to reanalyze the fracture using this number as the fracture height in the model in order to improve the comparative match between the measured and modeled tilt.

Next, with the development of a downhole tiltmeter tool that can be deployed in an offset well during the fracture experiment, another method for monitoring the fracture height produced can be developed. In this method the model would indicate what tilt would be produced and at what depth for a given fracture pressure and height. This information could be used to simply confirm the fracture height growth during a production fracture or in the case where fracture height is critical such as waste injection, serve as a limitation value. Here, in order to insure that the fracture height does not grow into excluded layers, a tilt value would be generated by the model that would serve as a value not to be exceeded. The downhole tiltmeter tools would measure the real-time tilt and by using the modeled tilt as a control, provide feedback to the operation.

It is important to remember that for a given fracture pressure relative to the stress conditions there is a limitation to the fracture height that it can support. In general the higher the stress, the higher the fracture pressure required to produce any given height. This can be seen in Figure 53 where an enormous fracture height (>>85 feet) would be required to produce 20 microradians of tilt for a fracture pressure of 1000 psi.

6.9 3D Model

6.91 Wing Length Effects

In the two dimensional model the fracture or wing length is treated as potentially infinite and it is left to the analyst to insure that no boundary effects occur. For the three dimensional model the wing length is specified and constructed in the model itself. In this study the values used for the wing length come from the microseismic diagnostic systems which monitor this component of the fracture process.

In order to determine what effect if any the addition of wing length has on the results of the B-sand analysis, a few cases were run in which the wing length was varied for a fracture height of 63 feet and a fracture pressure of 1300 psi. The wing lengths of 250 feet, 350 feet and 450 feet were selected to bracket the microseismically measured wing length of minifracs 5B and 6B (approximately 350-375 feet). The resultant tilt could then be compared to the final results of the 2-D model and measured field results from injections 5B and 6B.

The first case analyzed utilized a wing length of 250 feet. The crack width produced and the fracture parameters used are shown in Figure 54 and the tilt produced is shown in Figure 55.

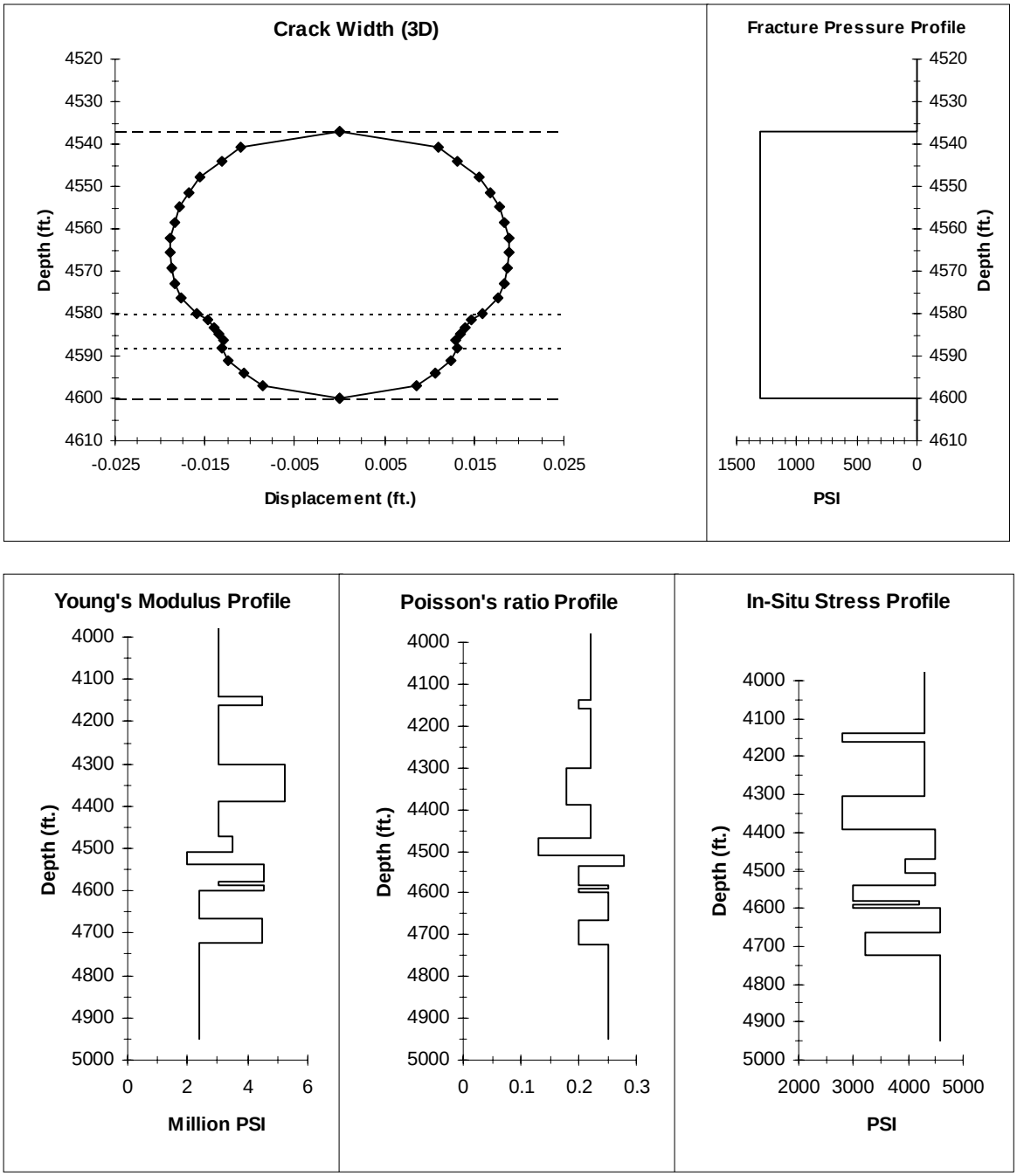

Figure 54. 250-foot wing length (3D).

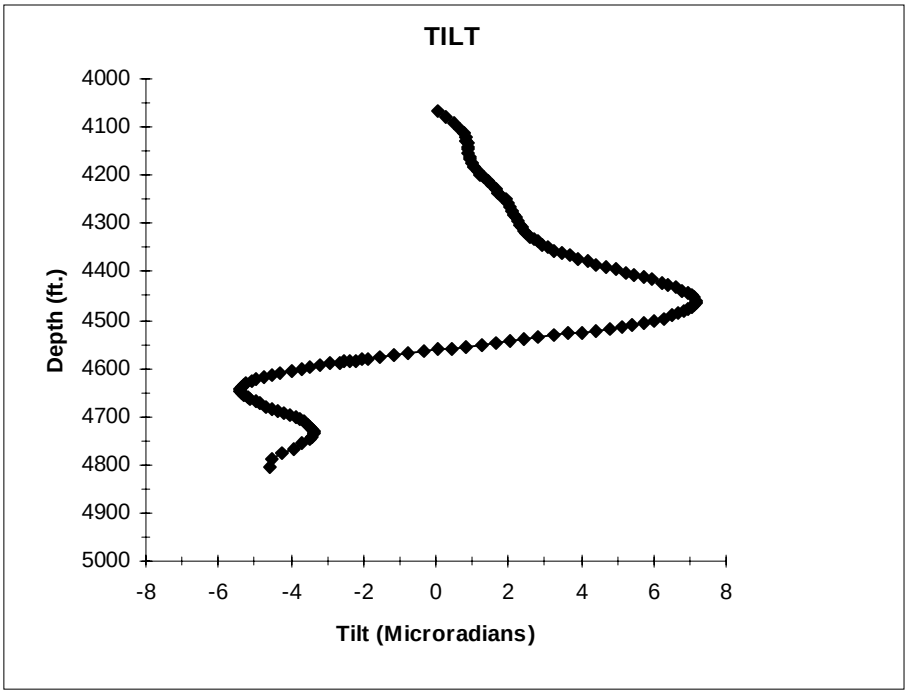

Figure 55. 250-foot wing length (3D).

The subsequent crack width and fracture parameters for the 350 foot wing length are shown in Figure 56, and Figure 57 contains the resultant tilt.

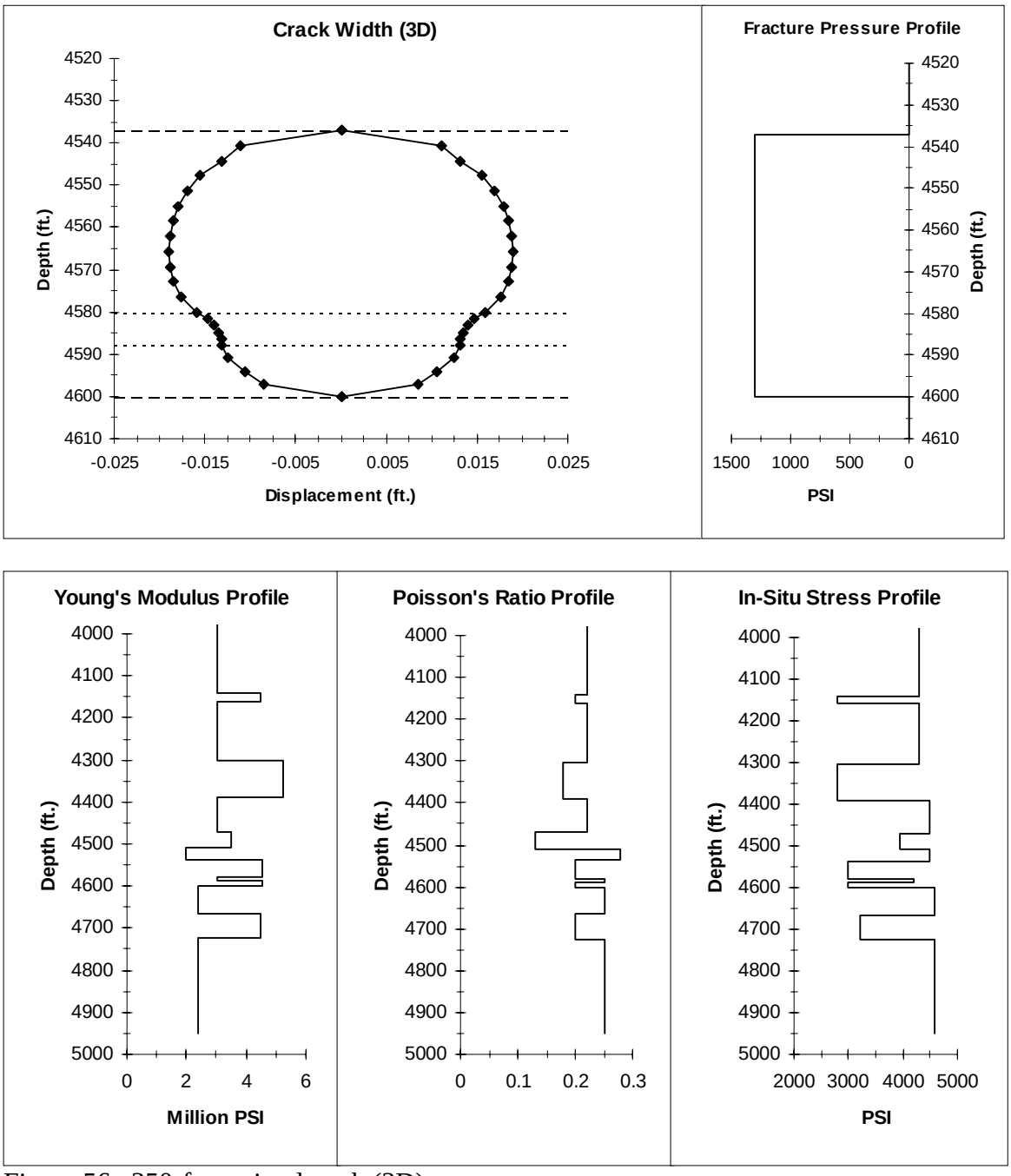

Figure 56. 350-foot wing length (3D).

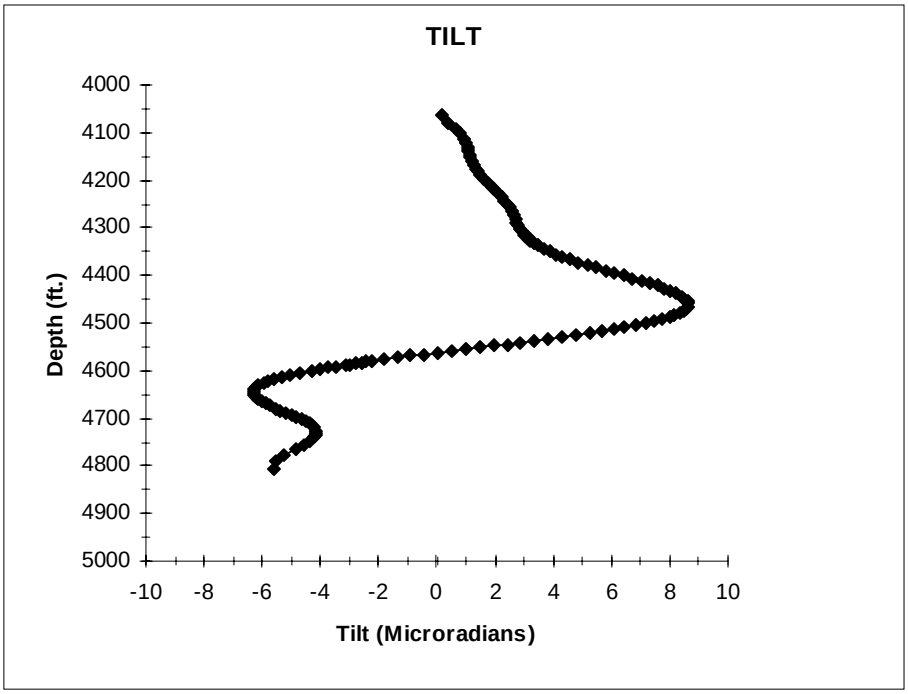

Figure 57. 350-foot wing length (3D).

Finally Figure 58 shows the crack width and fracture parameters used for the 450 foot wing length and the tilt for this case is shown in Figure 59.

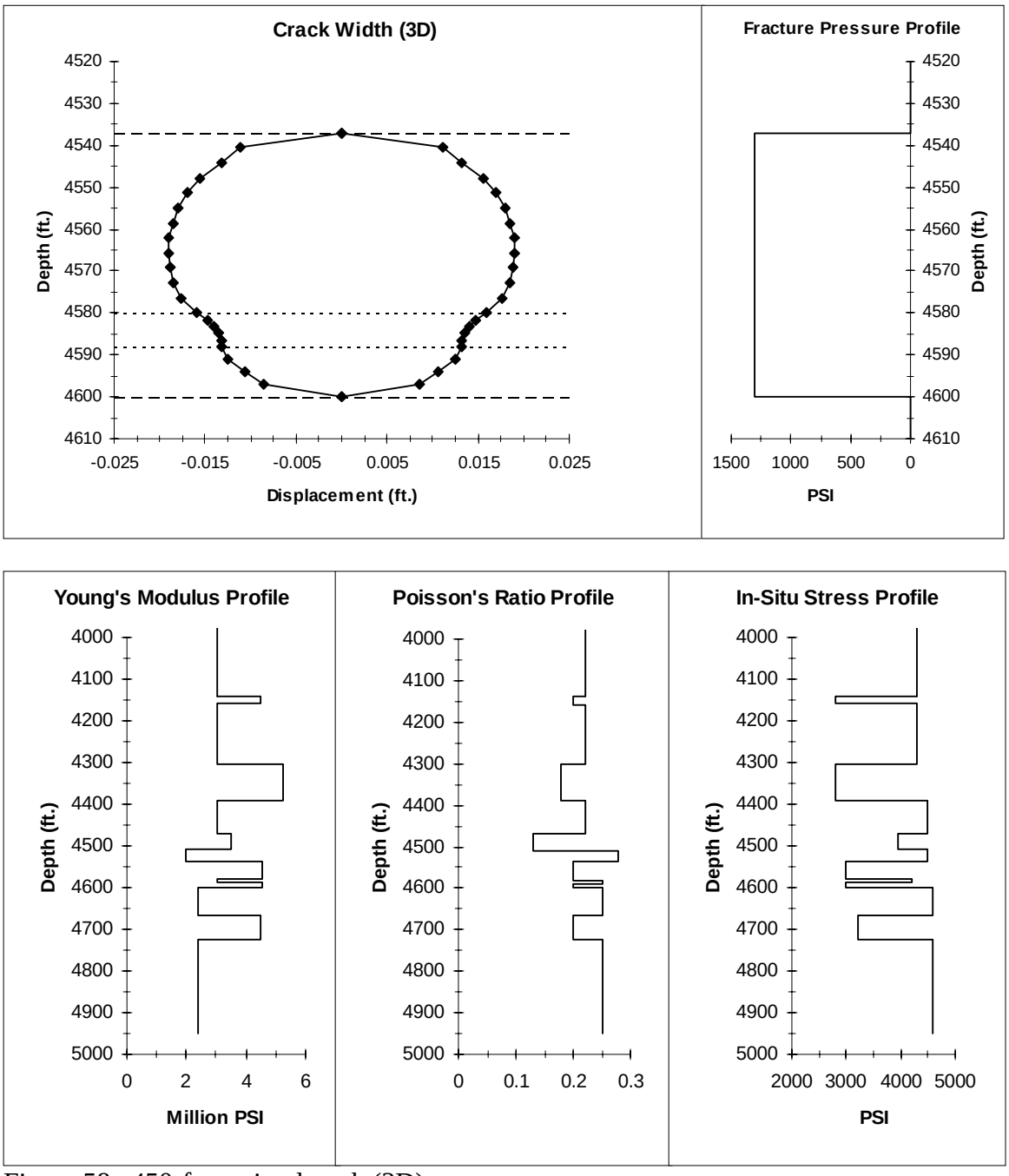

Figure 58. 450-foot wing length (3D).

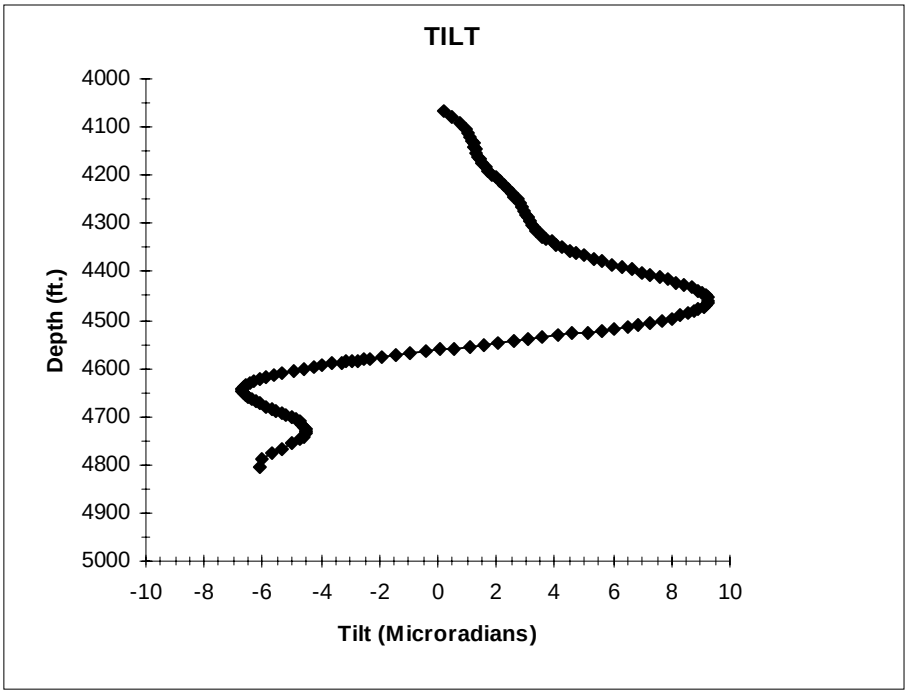

Figure 59. 450-foot wing length (3D).

Figure 60 is the comparison of tilts produced for all of the wing lengths analyzed, the final results from the 2-D model and the mini-frac's 5B and 6B. In this figure the curve with the largest peak amplitude comes from the final 2-D results and the remaining three curves are associated with the three wing lengths analyzed. As the peak amplitude decreases so does the respective wing length. The measured results from mini-frac's 5B and 6B are also indicated. Upon comparing the results, a three dimensional effect is indicated in that for a given fracture height and pressure the three dimensional model yields less peak tilt amplitude for the wing lengths used than the two dimensional model. This loss of amplitude can be countered however by increasing the fracture height. This effect was investigated next.

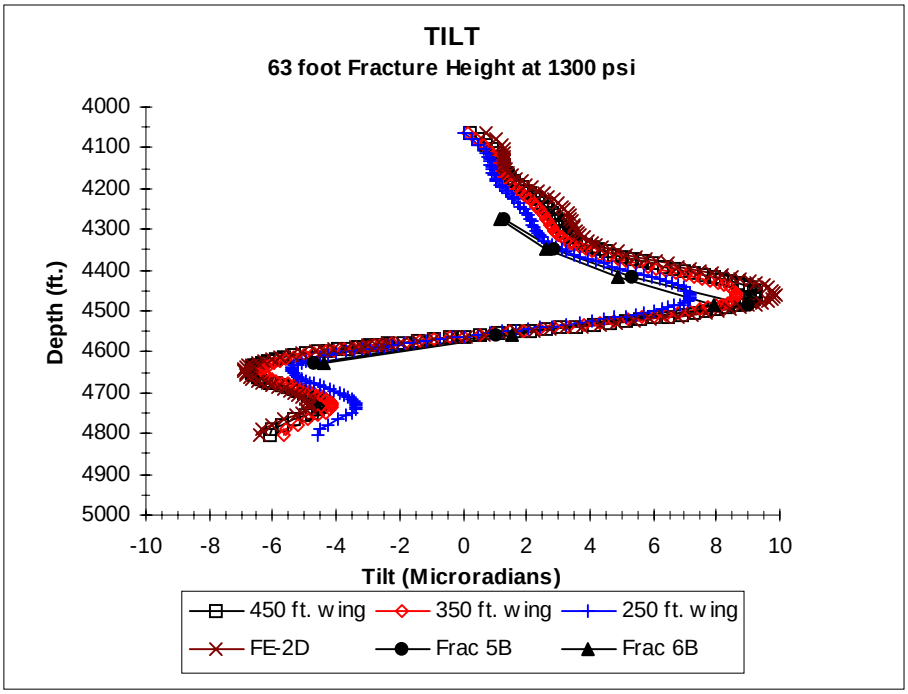

Figure 60. 3D wing length comparison.

6.92 Fracture Height Effects (3D)

The wing length for minifracs 5B and 6B, which were measured by the microseismic monitoring systems, grew to approximately 350 to 375 feet. When this length is used in the 3-D analysis, the peak tilt observed is about 8.7 microradians which is less than that measured in the field or predicted by the 2-D model. This reduction in peak amplitude can be regained by adjusting the fracture height slightly. The fracture height was adjusted from 63 feet to include 67 and 70 feet in the next models.

The previous Figures 56 and 57 show the results for the 63 foot fracture height, 1300 psi fracture pressure and 350 foot wing length. Figure 61 shows the crack width results and the parameters used in the 67 foot fracture height model while Figure 62 displays the resultant tilt.

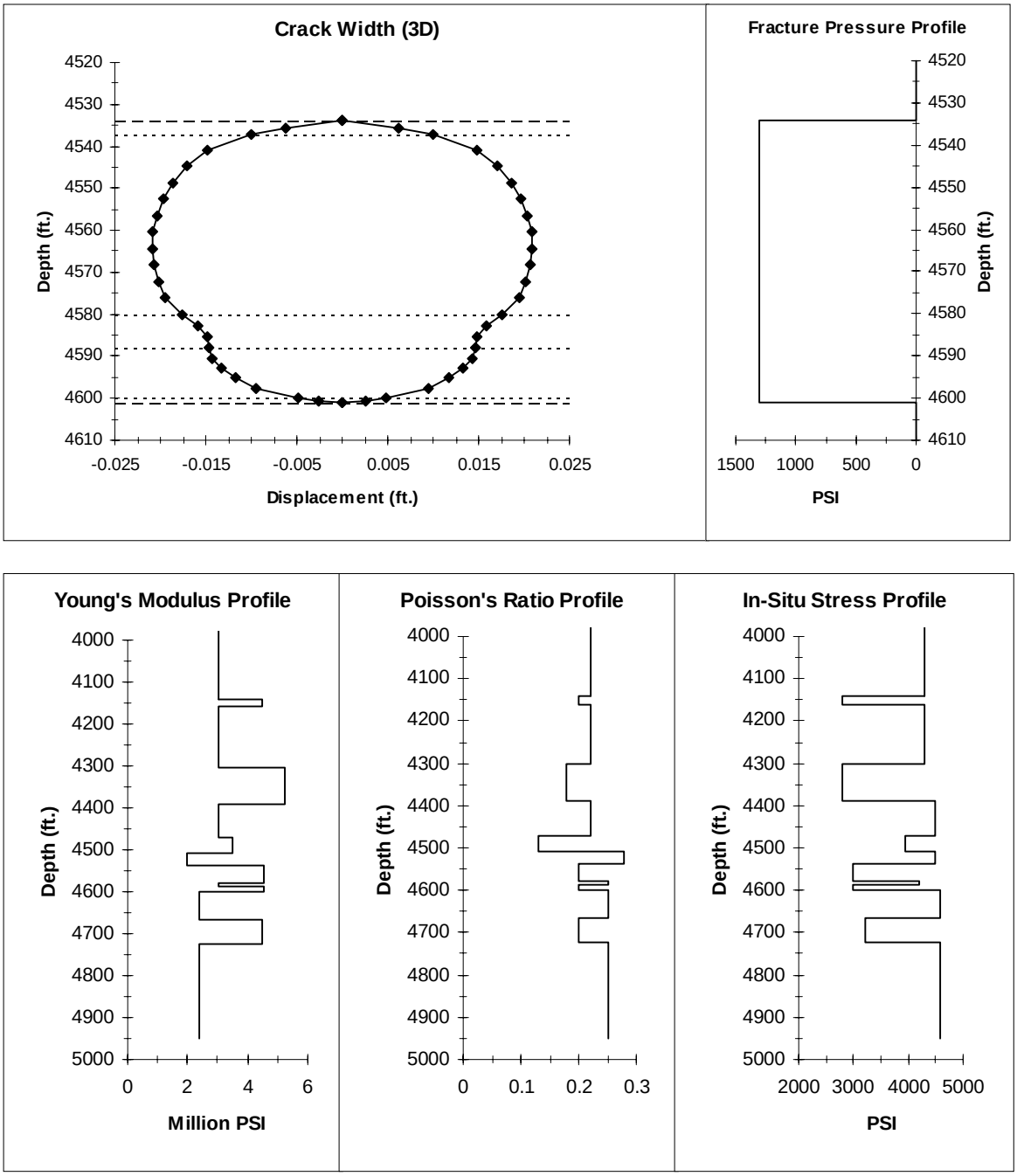

Figure 61. 67-foot fracture height, 350-foot wing length.

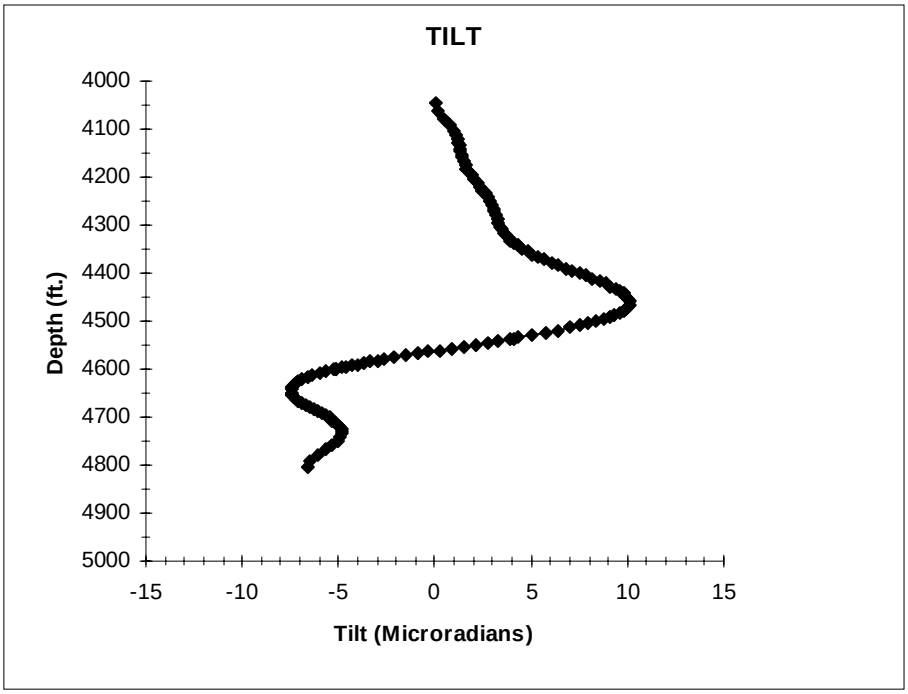

Figure 62. 67-foot fracture height, 350-foot wing length.

The crack width produced and the fracture parameters used for the 70 foot fracture height case is shown in Figure 63 with the tilt shown in Figure 64.

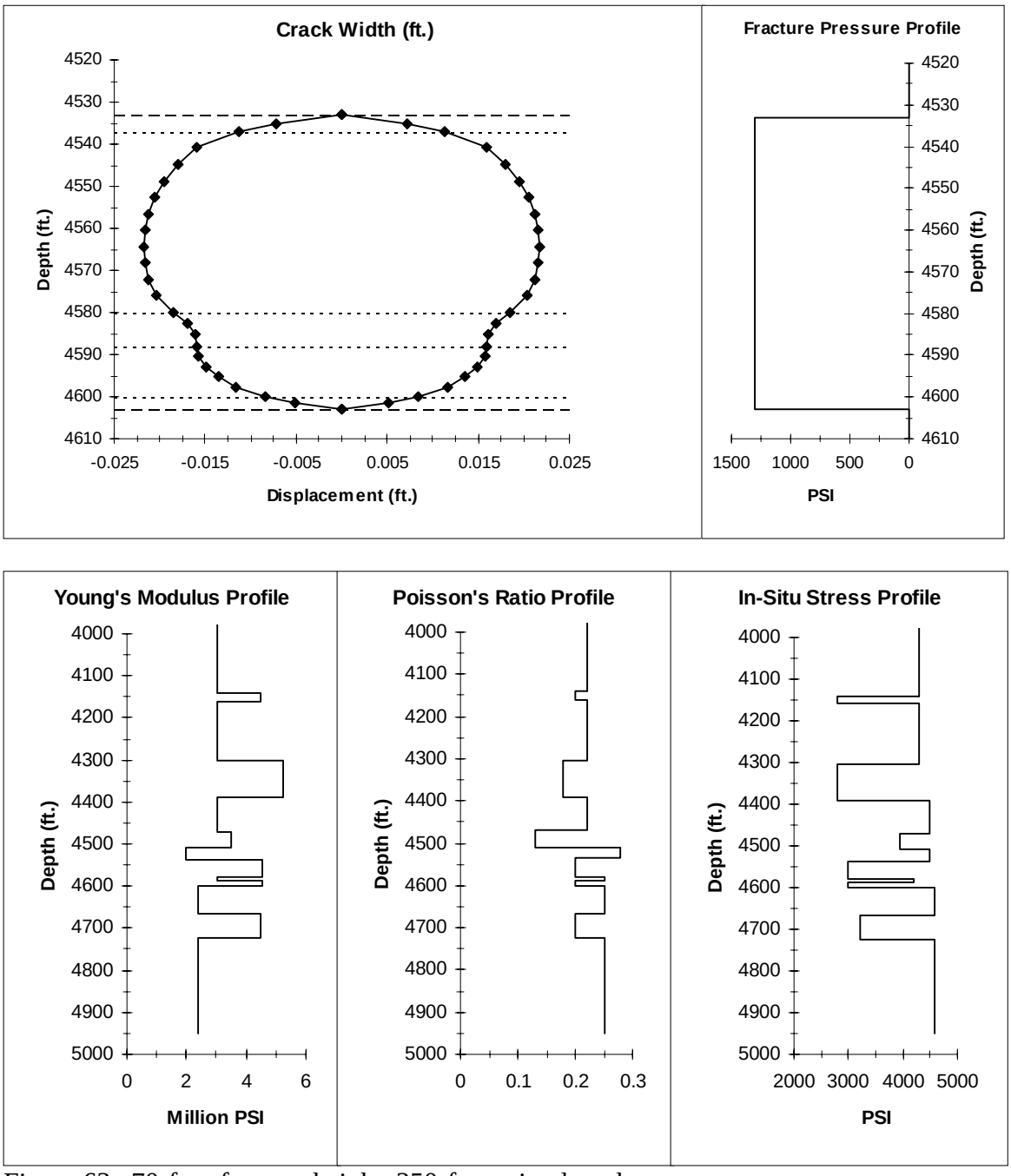

Figure 63. 70-foot fracture height, 350-foot wing length.

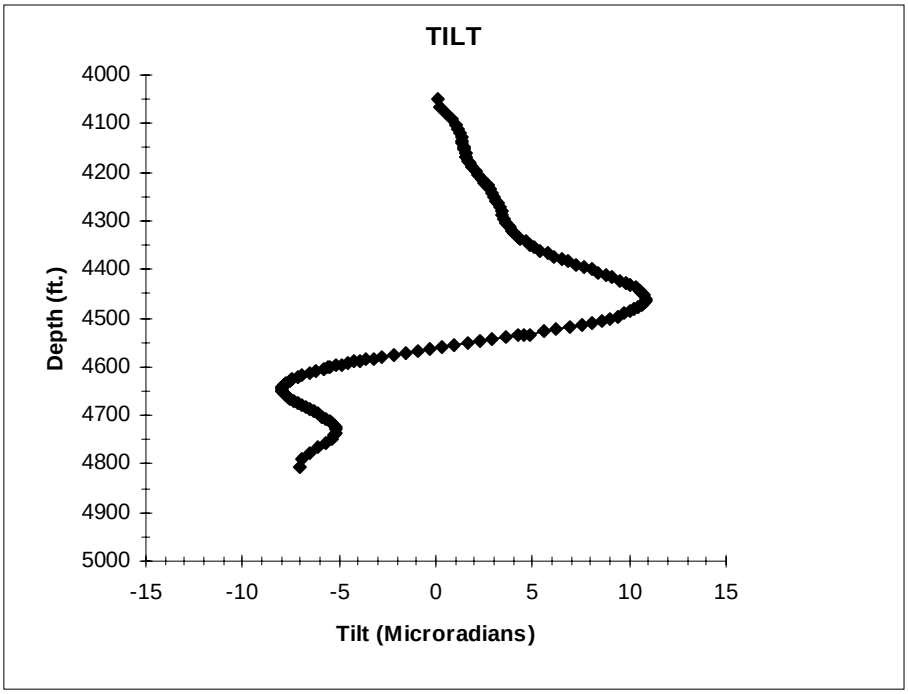

Figure 64. 70-foot fracture height, 350-foot wing length.

In Figure 65 the tilts produced by varying the fracture height slightly for a wing length of 350 feet are shown compared to the measured tilts from minifracs 5B and 6B. Indeed, by increasing the fracture height, the peak amplitude can be readjusted upwards to produce a better fit to the field tiltmeter data. For a wing length of 350 foot, the best fit appears to be a fracture with a height of 67 feet at a fracture pressure of 1300 psi. This case is considered to be the final fit of the 3-D modeled data for minifracs 5B and 6B.

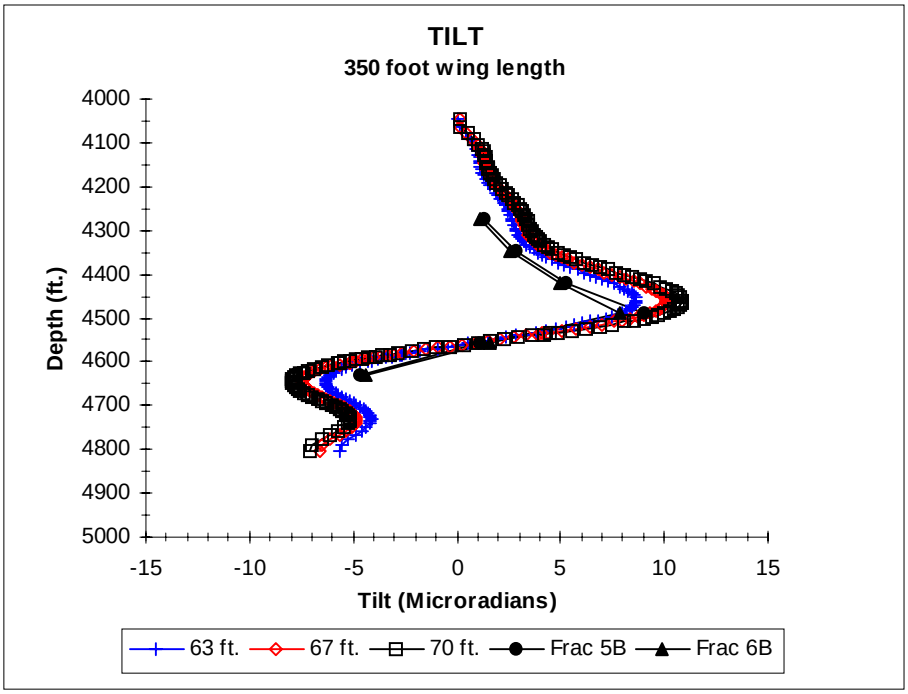

Figure 65. Fracture height variation - 350-foot wing length.

The two dimensional model could not produce as reasonable a fit to the treatment 7B field tiltmeter data as it did for the 5B and 6B minifracs. This is shown in Figure 66, in which the results previously obtained from the seven layer 2-D model are compared to the actual field data. The modeled results were produced by varying the fracture height for a fracture pressure of 2000 psi. The heights used were 40 feet, 55 feet, 63 feet, 100 feet and 150 feet. As the fracture height is increased there is a corresponding increase in the tilt produced. Notice that the best fit to the field data occurs utilizing a fracture height of around 63 feet while the seismic data indicates a near wellbore fracture height of 135 feet and a fracture height of approximately 80 feet for the remainder of the fracture wing.

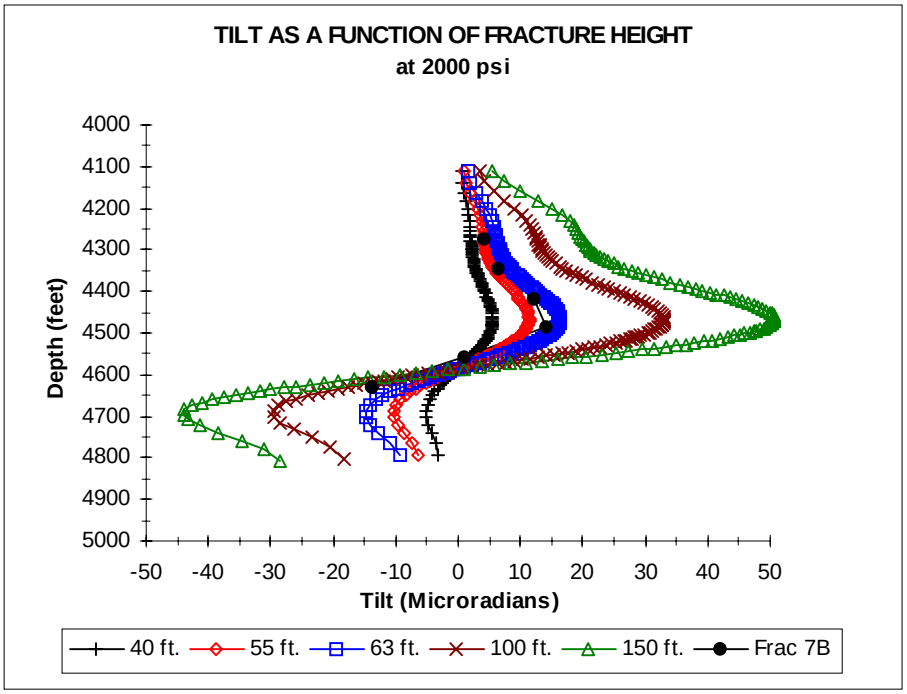

Figure 66. Tilt as a function of fracture height at 2000 psi.

In order to observe the effect of fracture pressure upon the tilt produced, the model was first updated to contain the final thirteen layers and then for a fracture height of 80 feet the fracture pressure was varied. The fracture pressures utilized here are 1000 psi, 1300 psi, 1700 psi and 2000 psi. As the fracture pressure increases there is a corresponding increase in the modeled tilt produced as shown in Figure 67. However when compared to the field data, the best fit is achieved for a fracture pressure of approximately 1400 - 1500 psi.

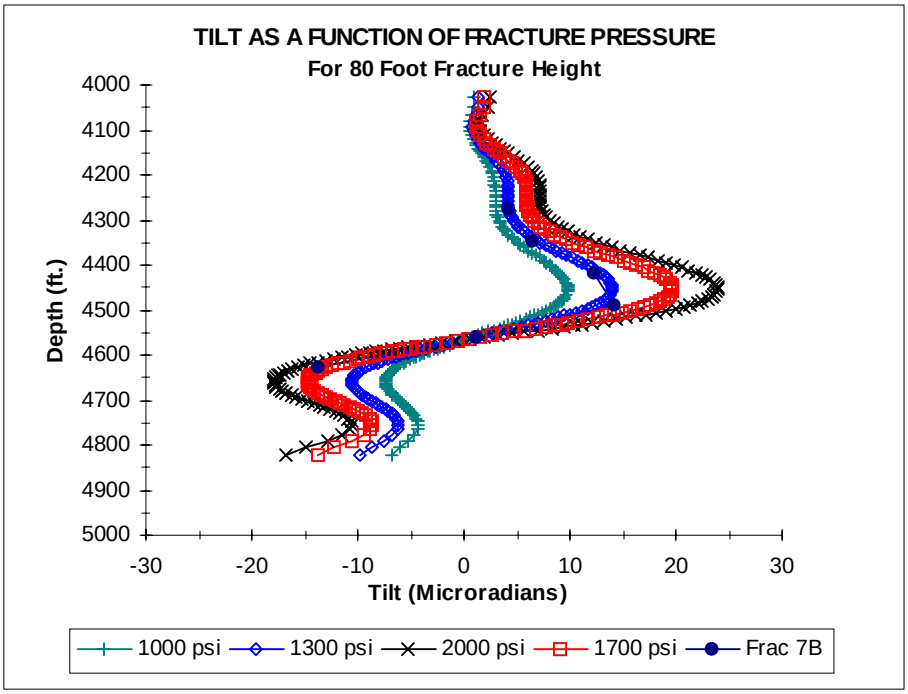

Figure 67. Tilt as a function of fracture pressure for a fracture height of 80 feet.

Thus, the two dimensional model suggests that the fracture pressure is actually lower than the measured net pressure of 2000 psi and that the fracture height appears to be less than 135 feet. Several possibilities could explain this discrepancy. One possibility may be that in 2-D space as the fracture grows and passes by the tiltmeter which is offset from the fracture plane, the height produced is effectively seen as an average. This input would vary as a function of cosine squared and calculates to a height of 71 feet. For the 2-D model the best fit for mini-frac 7B involves a fracture height of approximately 80 feet which agrees with the calculated average and a fracture pressure of 1500 psi. Another possibility involves a type of 3-D effect such as a near field pressure drop due to the use of the crosslinked-gel/sand slurry. However this type of effect cannot be modeled with the 2-D code where the application of the pressure is limited to be uniform in nature along the fracture length. Therefore the main thrust of the analysis for mini-frac 7B was modeled in 3-D space where these types of effects could be handled appropriately.

7.0 Fracture 7B (3D)

Injection 7B was a crosslinked-gel/sand frac that reached a net borehole fracture pressure of 2000 psi. The total wing length of this fracture as measured by the microseismic monitoring systems was 400 feet. However the fracture height produced was not consistent over the total wing length as in the previous minifracs. The initial fracture height was 135 feet for the first 150 feet, followed by a height of 80 feet for the next 250 feet. The current analysis has been based upon a fracture model in which the fracture height is constant for the length of the fracture. In the two dimensional model, the fracture is considered to have a specified height and be infinitely long with the pressure applied at the face of the fracture at the wellbore, whereas in the three dimensional model the fracture height and length are both specified with the pressure applied perpendicular to the face of the fracture plane. This pressure is presently applied in both cases uniformly across the modeled fracture plane.

Initially a few cases were analyzed in which the fracture pressure from the 2-D analysis (1500 psi) was incorporated directly into the 3-D model. The variable for these cases was the fracture height which was changed to provide a range of comparison to the measured fracture height of 135 feet. Figure 68 shows the crack width and fracture parameters used for the first analysis of a fracture height of 120 feet.

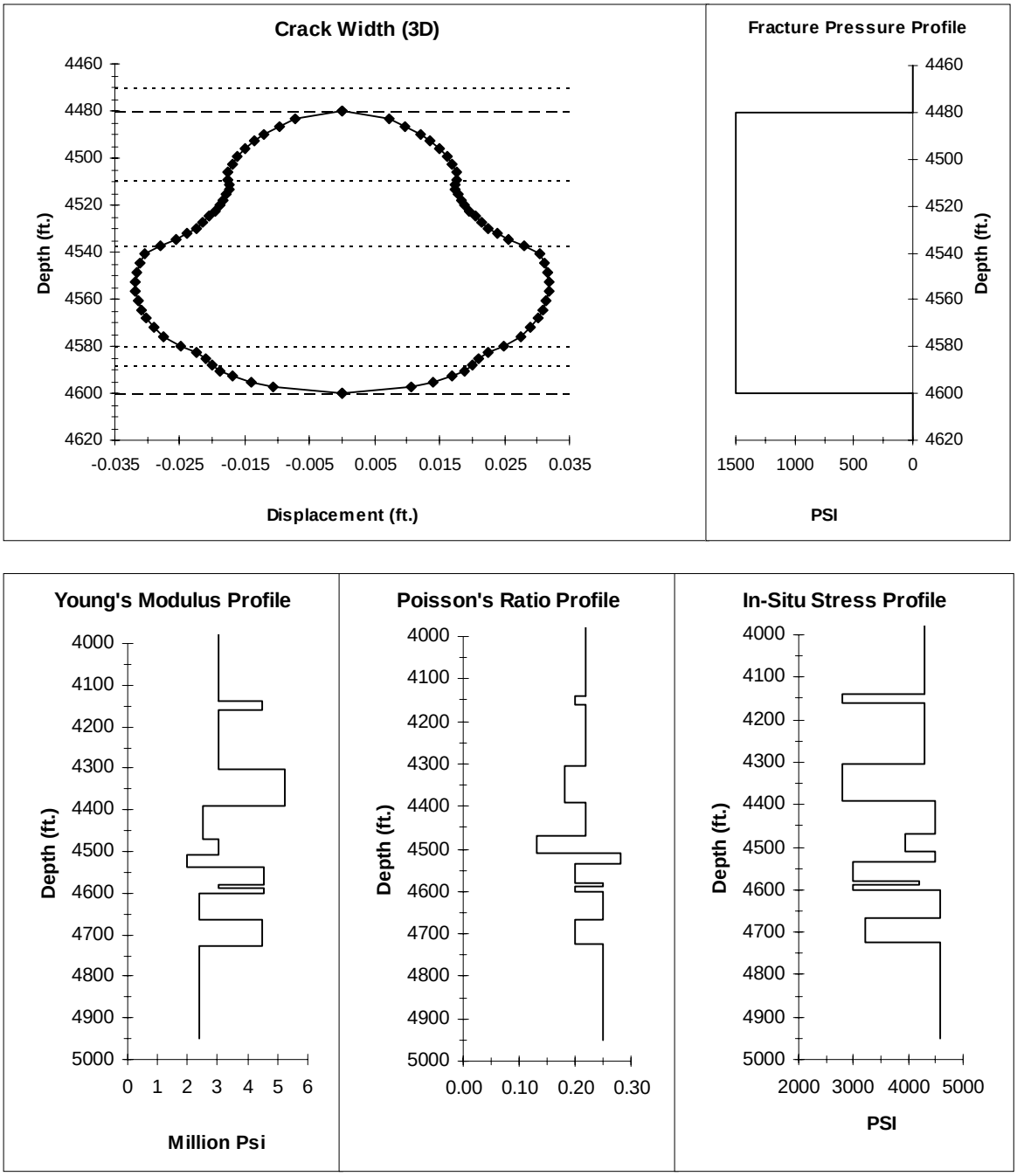

Figure 68. Initial fracture height of 120 feet.

In Figure 69, the crack width and fracture parameters are shown for the case were the initial fracture height was changed to 130 feet.

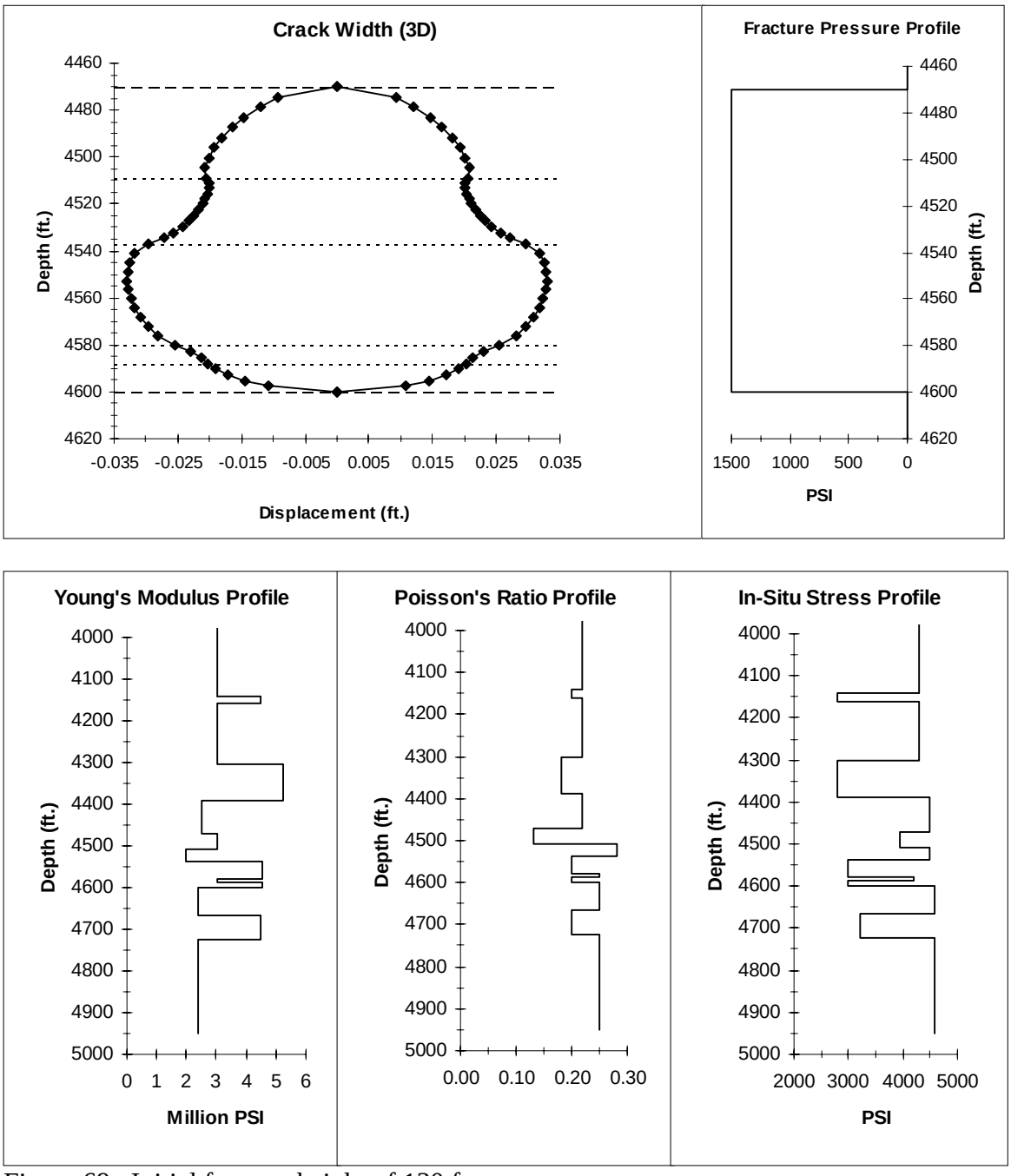

Figure 69. Initial fracture height of 130 feet.

Finally the crack width and fracture parameters for the case in which the initial fracture height was 135 feet is shown in Figure 70.

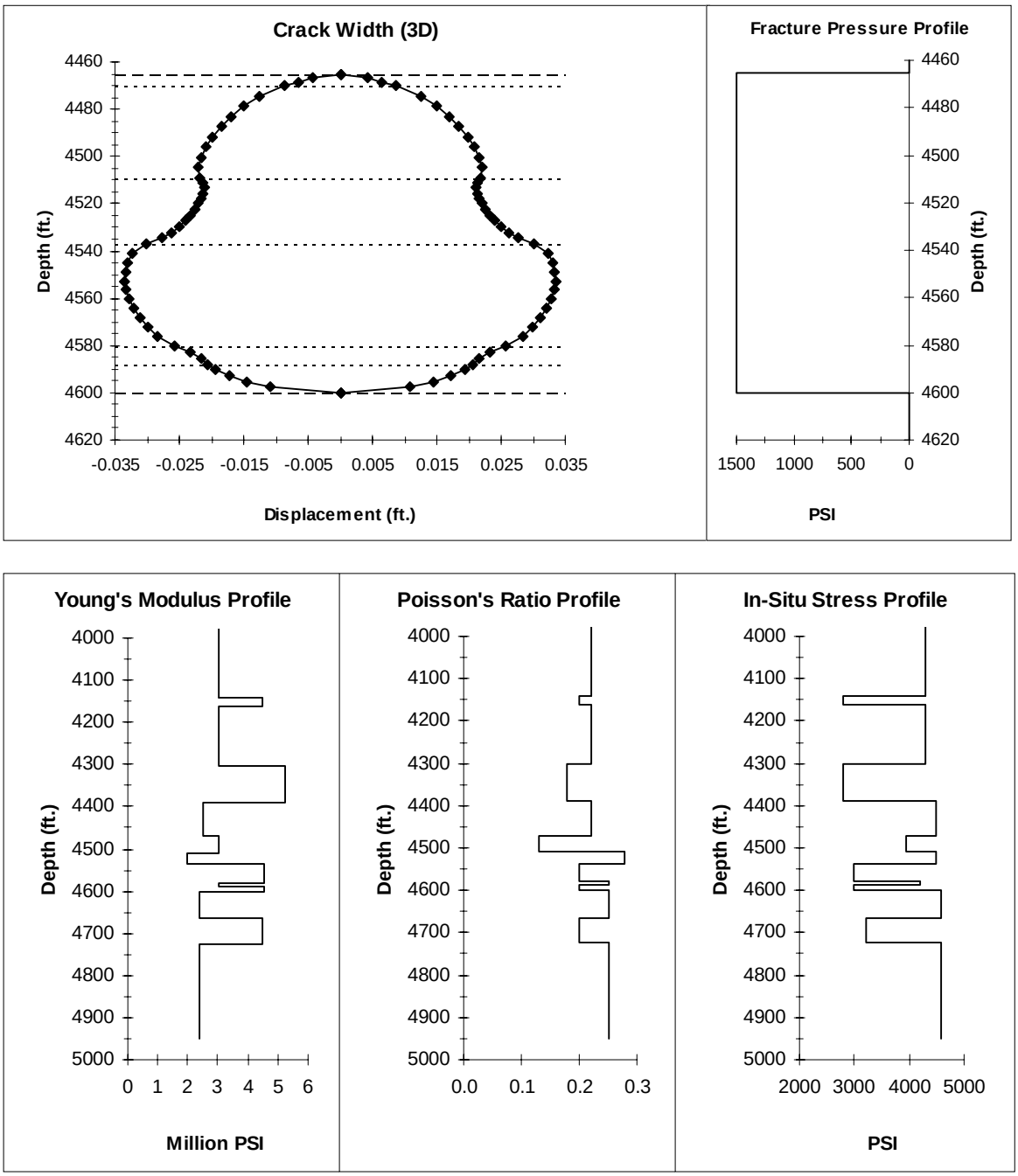

Figure 70. Initial fracture height of 135 feet.

The tilts produced for these three cases are compared to the tilt measured for the 7B treatment in Figure 71.

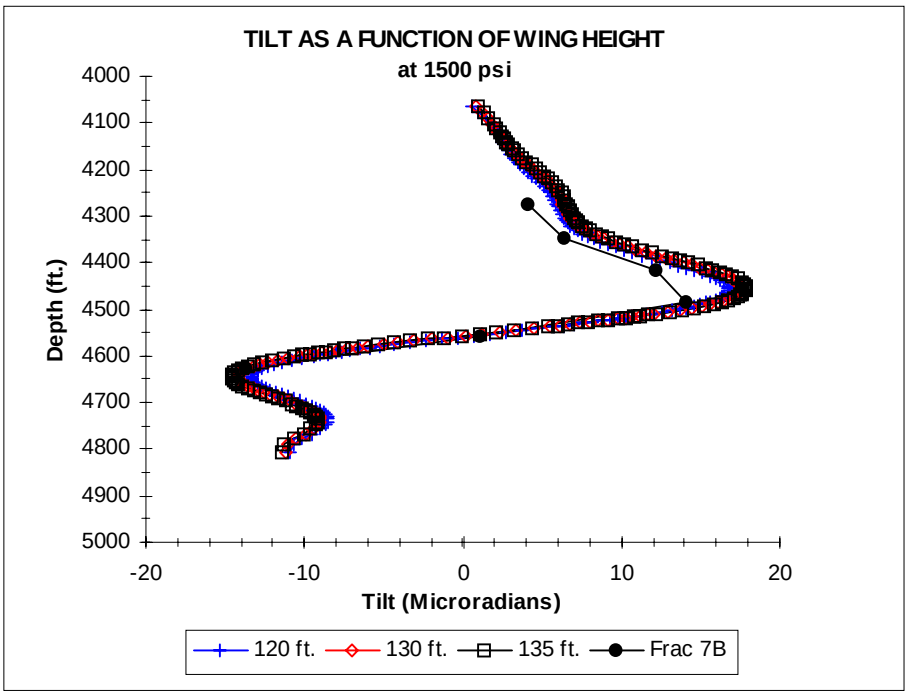

Figure 71. Tilt as a function of wing height at 1500 psi.

As the initial fracture height of the model decreases, there is a corresponding decrease in the tilt produced. The ten percent decrease in height results in a six percent decease in peak tilt amplitude, however, the decrease in other areas proves to be even less. Any of these three cases provides a good match with the tiltmeter field data. The overall slope characteristics, the zero point and peak amplitudes of the curves produced compare well with the field data. Therefore investigation into the match produced by decreasing the initial fracture height even further was not conducted at this time. Instead the focus was shifted to account for the difference between the modeled fracture pressure and the measured net fracture pressure.

To help get a feel for the size of the pressure difference that would have to be dealt with, an additional case was analyzed in which the initial fracture height was modeled at 120 feet with a fracture pressure of 1400 psi. The fracture parameters and crack width are shown in Figure 72. The comparison of the tilt produced for this fracture height of 120 feet as a function of the fracture pressure is shown in Figure 73. Again, with the decrease in the fracture pressure from 1500 to 1400 psi, there is also a decrease in the peak tilt amplitude. Upon close examination however the match with the field data at the peak amplitudes begins to degrade. This fracture pressure should be considered the minimum value.

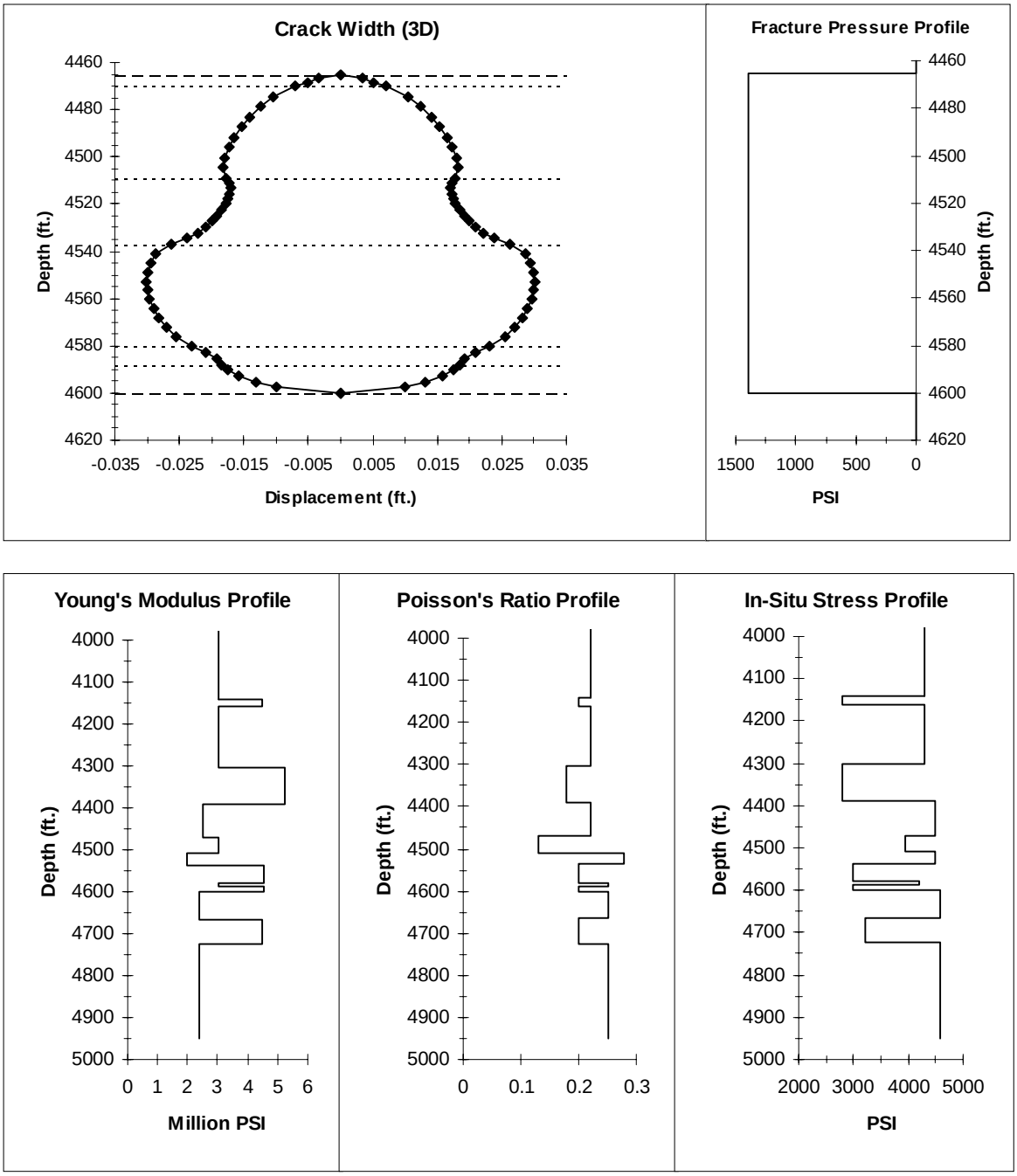

Figure 72. Initial fracture height of 120 feet at 1400 psi.

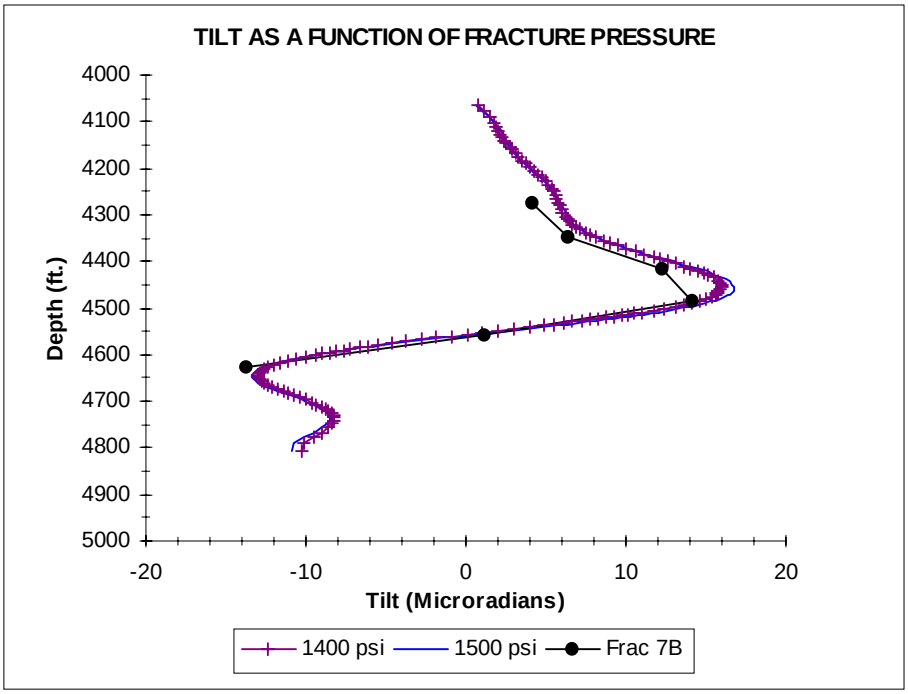

Figure 73. Tilt as a function of fracture pressure for fracture height of 120 feet.

With an acceptable fracture height range of 120 to 135 feet and a fracture pressure of approximately 1500 psi, the 3-D code was modified to include the application of a pressure drop over a specified near field distance. The distance would be determined by specifying the number of elements within the modeled mesh that are to be included in the pressure drop calculation. For this series of tests, the first two elements (17 feet) and the first three elements (29 feet) were chosen as the distances over which a pressure drop would be applied. The pressure drop was selected to be either 500 or 600 psi in addition to a constant 1500 psi fracture pressure resulting in a net pressure of 2000 psi. In all cases the initial fracture height was set at 135 feet for a length of 150 feet and then stepping down to a height of 80 feet for a length of 250 feet.

For the first case, a pressure drop of 500 psi was applied over the first two elements. The fracture parameters and the crack width are shown in Figure 74. The tilt produced in this case is indicated in Figure 75.

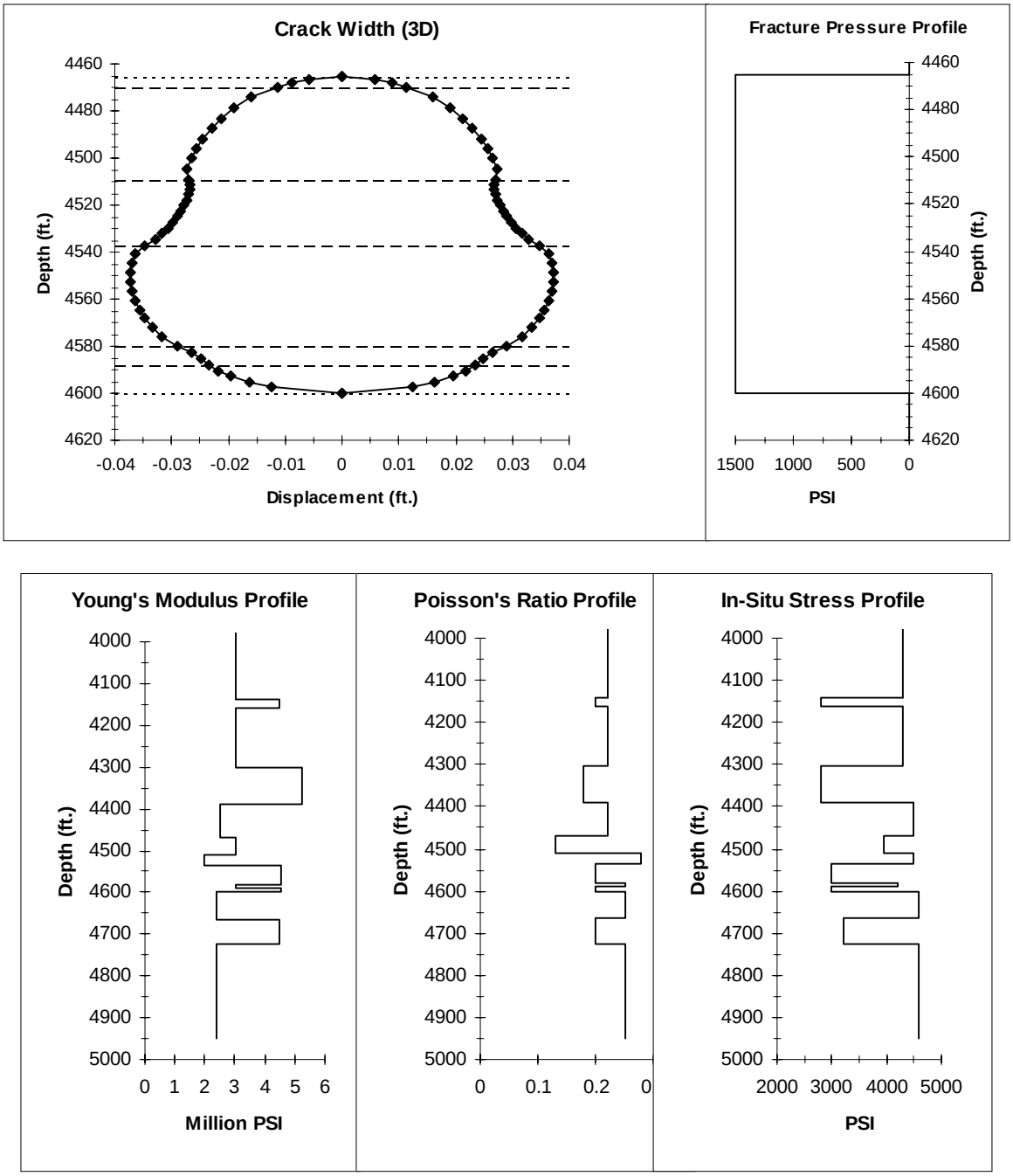

Figure 74. 500-psi pressure drop over 17 feet.

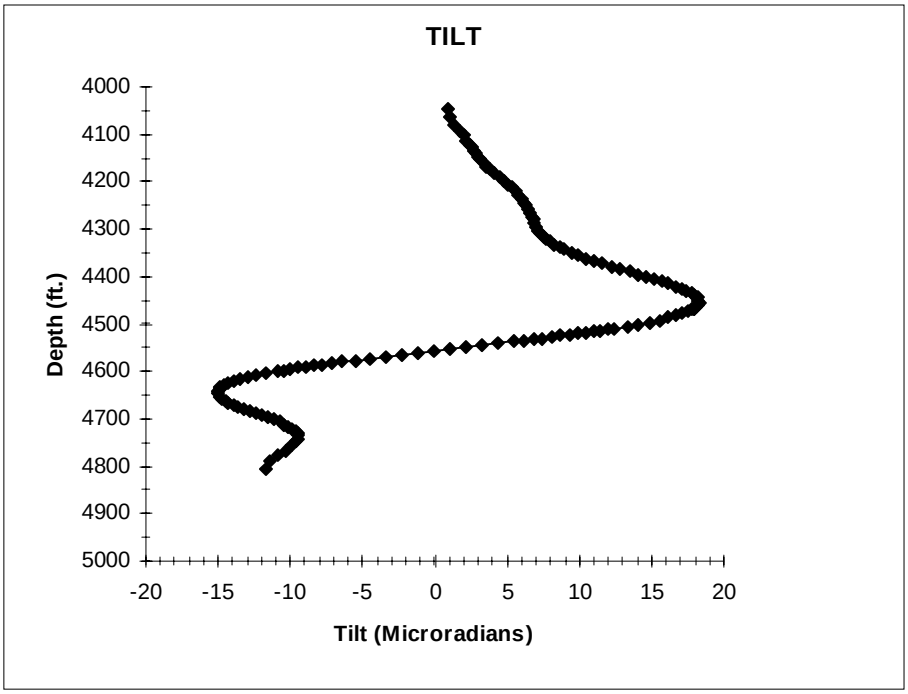

Figure 75. Tilt for 500-psi pressure drop over 17 feet.

Next a 600 psi pressure drop was applied over the first two elements. Figure 76 shows the parameters utilized and the crack width produced while Figure 77 shows the tilt produced.

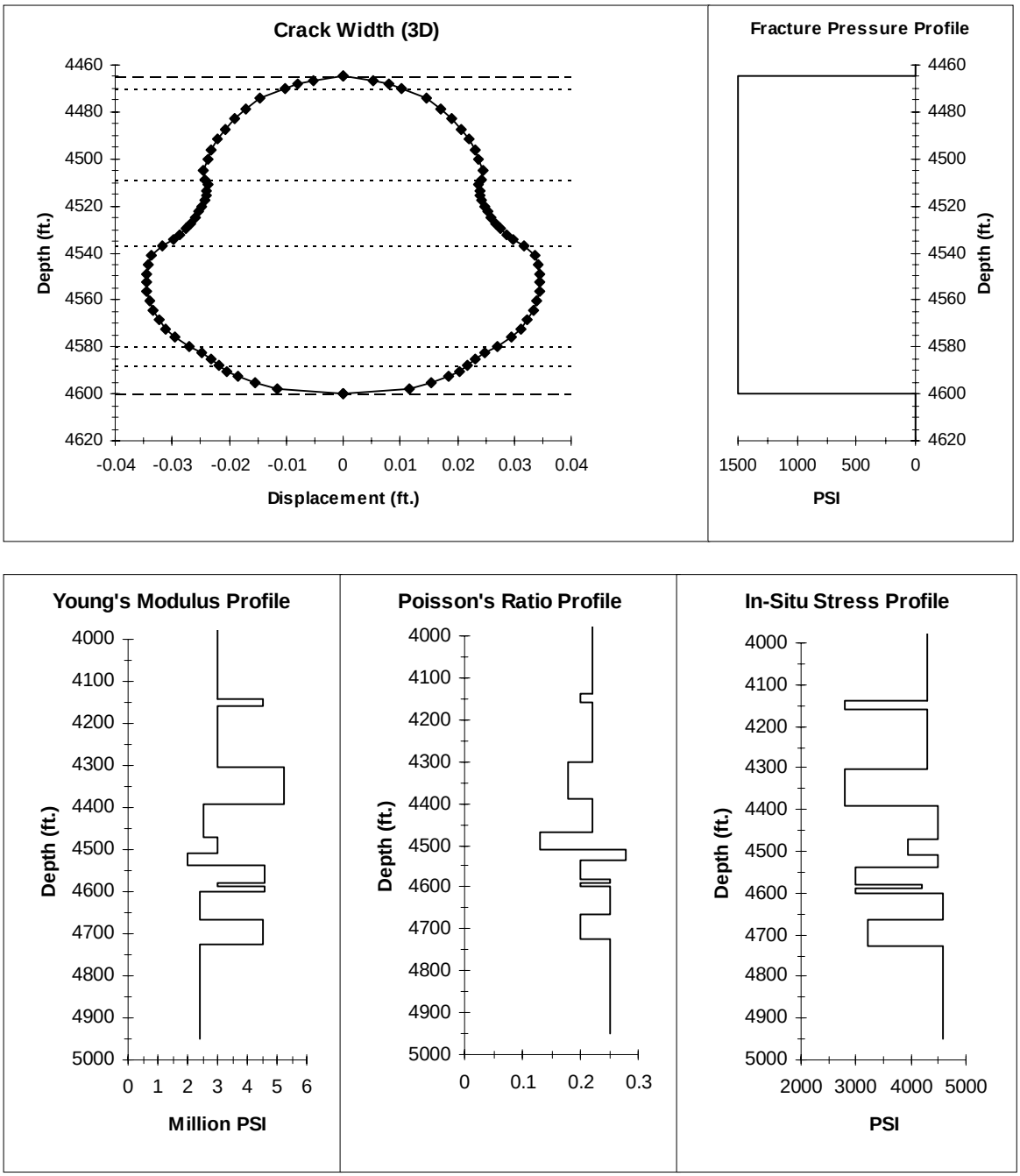

Figure 76. 600-psi pressure drop over 17 feet.

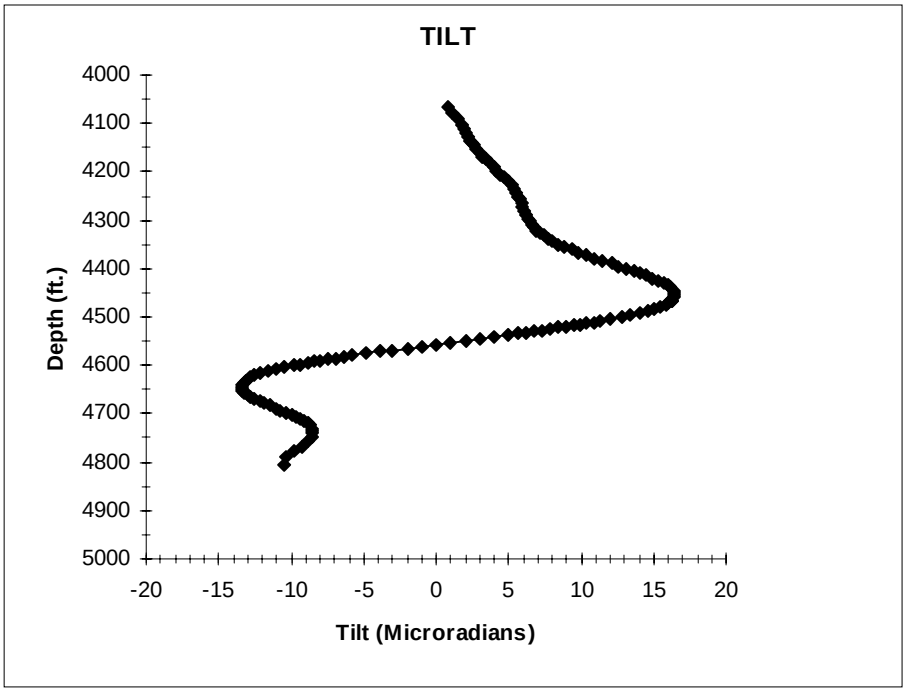

Figure 77. Tilt for 600-psi pressure drop over 17 feet.

Finally a 600 psi pressure drop was applied over the first three elements (29 feet). Figure 78 contains the crack width produced and the parameters utilized in the analysis. Figure 79 shows the resultant tilt produced in this case.

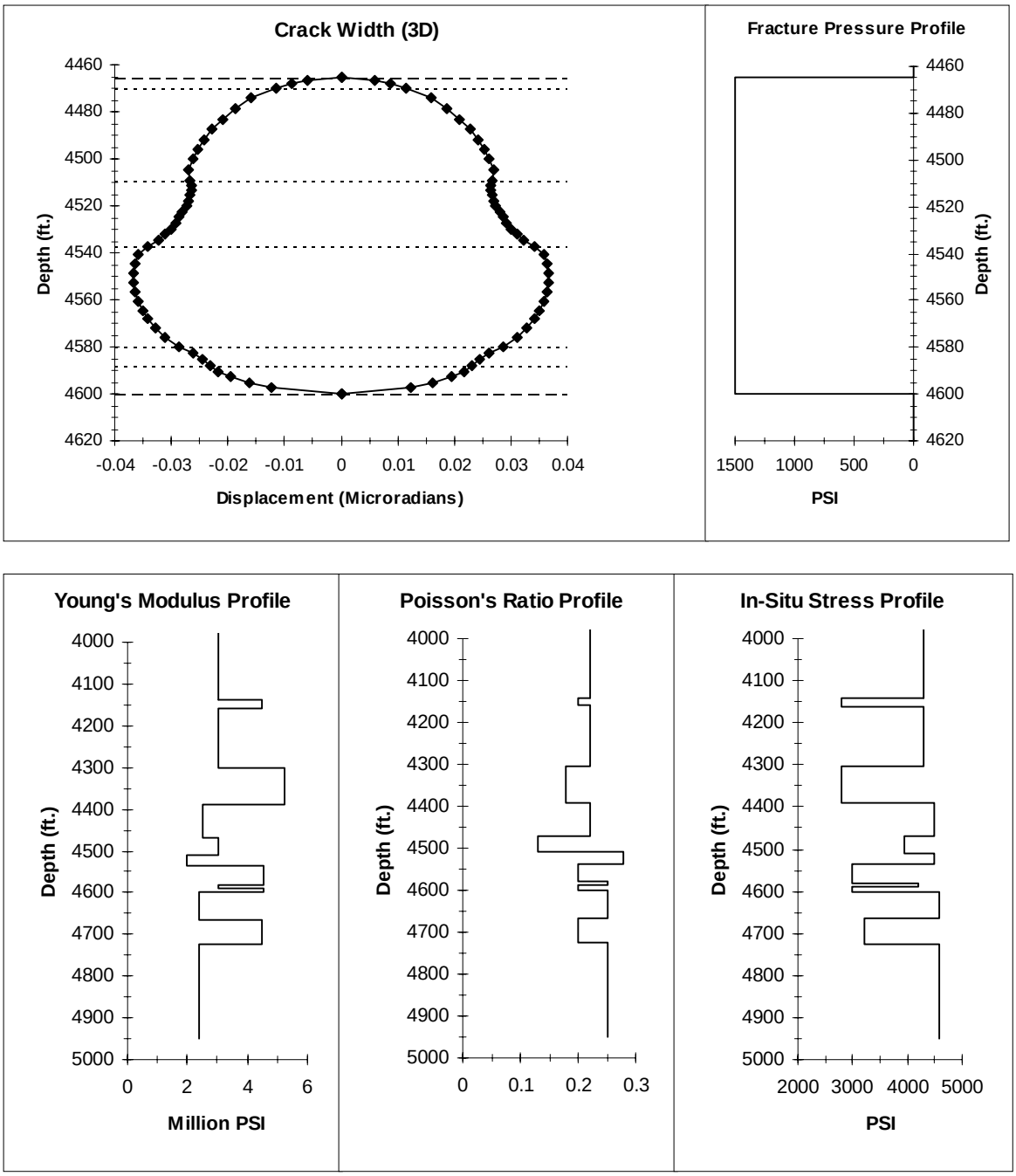

Figure 78. 600-psi pressure drop over 29 feet.

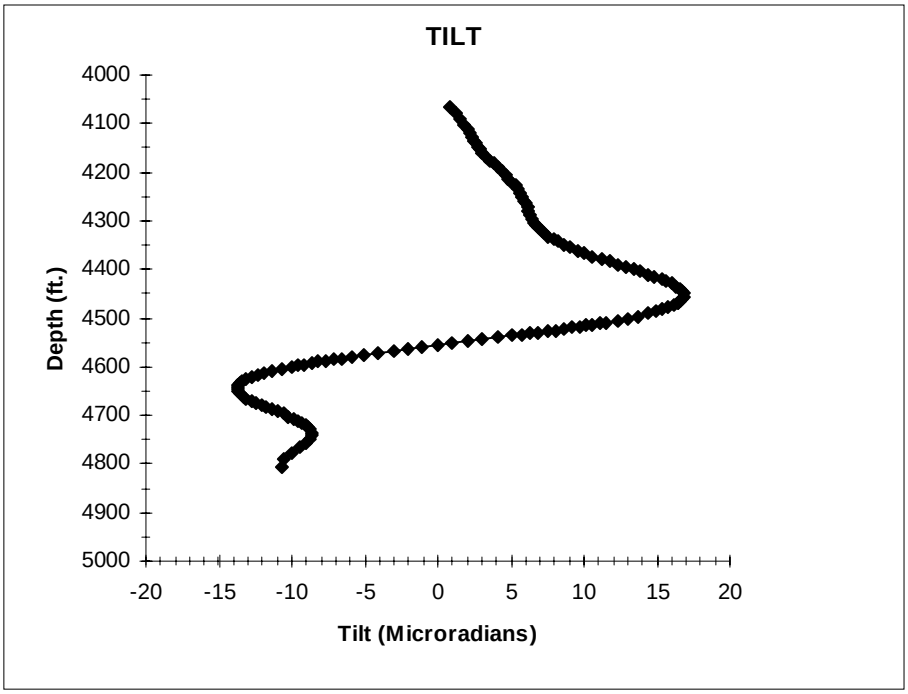

Figure 79. Tilt for 600-psi pressure drop over 29 feet.

Figure 80 compares the tilts produced in the preceding three cases with the measured tiltmeter results from injection 7B. The largest tilt was produced when the 500 psi pressure drop was used in the analysis and subsequently decreased when the pressure drop was increased to 600 psi. The change in the tilt produced is insignificant when the pressure drop distance was increased from 17 feet to 29 feet for the 600 psi pressure drop. By increasing the pressure drop distance, only the peak tilt value increases marginally. Thus the match could be adjusted further by increasing the pressure drop for these given distances, decreasing the distance over which the pressure drop is applied or a combination of the two. For this study the match is considered to be excellent overall for a 600 psi pressure drop over a distance of 29 feet.

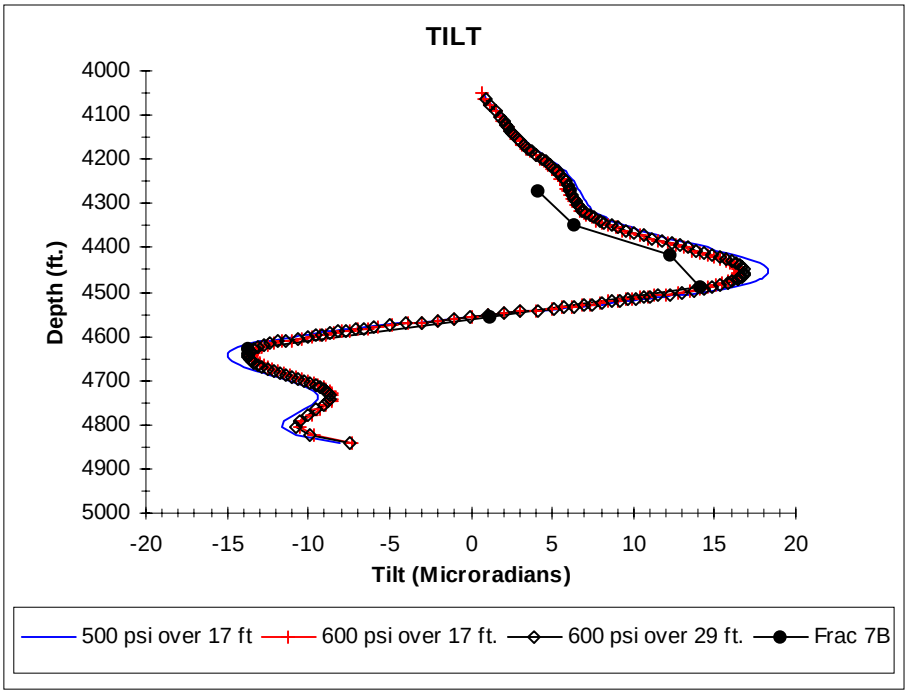

Figure 80. Pressure drop tilt comparison.

Finally, in Figure 81 the tilt produced with no pressure drop applied is compared to the analysis in which 600 psi was dropped over a distance of 29 feet. The larger tilt amplitude is associated with the case in which no pressure drop was applied. By modeling an applied pressure drop the match between the measured tiltmeter data and the finite element analysis model improves. It also shows that a large near-wellbore pressure drop would not significantly affect the inclination magnitudes as long as the appropriate far-field pressure is applied within the bulk of the fracture.

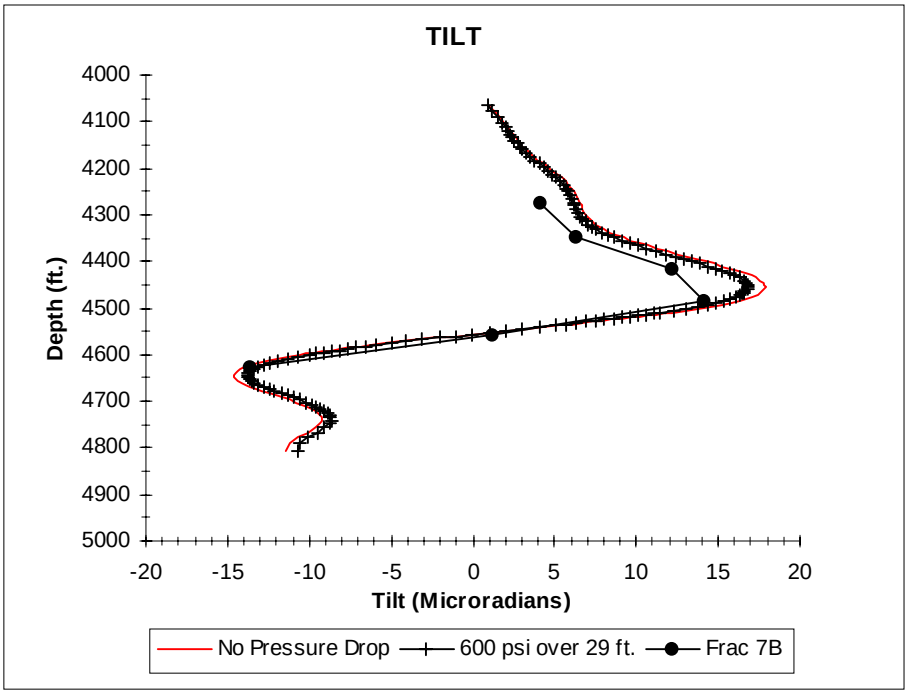

Figure 81. Pressure drop vs. no pressure drop.

8.0 DISCUSSION AND CONCLUSIONS

These results show that finite-element analyses of inclinometer results can provide significant enhancement in diagnostic information over the simple use of analytic models. In particular, the finite element models can accommodate layering effects and complex geometry effects that are not compatible with simple solutions.

Of primary importance for these tests were the effects of a layered structure with modulus differences on the order of 2-3. The initial testing showed that modulus is the single most important factor controlling the amplitude of the resultant tilt. While an average modulus value used in analytic calculations will generally fit the data, it has been shown that a detailed fit of model results can require modulus variations to adequately represent the "character" of the measured data. In these tests, the modulus variations caused the upper peak in the data to have a larger amplitude and narrower width than would be expected for a homogeneous material alone. In addition, the falloff of tilts above the peak was greater than would have been normally expected. Both of these features could be accommodated by using a 13-layer material model with an appropriately sized and placed fracture.

The second important use of the finite-element analysis was for evaluating a complex geometry. For most of the tests, the microseismic results showed limited fracture growth and nearly constant height along the length of the fracture. For these cases, both analytic and 2-D finite element models work quite well for evaluating fracture parameters. However, for the 7B injection (propped stimulation), the microseisms suggested that the fracture had a much more complex geometry with a height of about 135 ft over the first 150 ft of length and a reduced height of 80 ft over the remainder of the fracture. A 3-D finite element analysis was required to evaluate whether the microseismic geometry was plausible based on the measured inclinations. In this case, the measured microseismic geometry, when used in the 3-D simulator, gave inclinations in good agreement with the measured data, but only when the net pressure in the fracture was reduced. However, this reduction was based on many other aspects of the treatment behavior which suggested that the high net pressure was induced by some near-wellbore effect and did not extend far out into the body of the fracture.

The main objective of the inclinometer diagnostics array was to provide confirmation of the microseismic height as measured by multi-level downhole receiver arrays in two offset wells. Table 11 gives a comparison of the microseismic and inclinometer heights for the 5 tests where finite-element calculations were performed. The inclinometer heights are all based on full 3-D estimates of the fracture height given the 2-D length provided by the microseismic data. For the KCl injections and the minifracs, this additional piece of information allowed the incorporation of length effects from the fracture. Generally, however, the final 2-D and 3-D heights were within a few feet of each other (2-D fractures require slightly less height) and the corrections are minimal. Treatment 7B was the only exception to the process, as a 3-D model was required from the start, based on knowledge of the complex geometry from the microseisms. As noted

previously, injection 7B was modeled using the microseismic shape to assess whether the inclinometer data were in agreement. In all tests, the microseismic data were in excellent agreement with the inclinometer data, especially considering that microseisms have a vertical location error that is on the order of 5-10 ft depending on the array and the quality of the data.

Table 11 Comparison of microseismic and inclinometer heights

TEST	MICROSEISMIC HEIGHT	INCLINOMETER HEIGHT
3B	55	52
4B	55	52
5B	80	67
6B	75	67
7B	135/80	135/80

Previous results showed that the modulus variations have a significant effect on the induced inclinations. Poisson's ratio, on the other hand, had very little effect on the induced tilts in any layers. The various stresses in the layers had minimal effect as well, but this is primarily due to the limited height growth. The in situ stress works its effect at the point of deformation, that is, at the crack by reducing the level of net pressure opening its particular layer. If cracks do not contact many layers with different stresses, then little effect of the stress field will be noticed. Conversely, if there is extensive height growth and the fracture is in contact with many layers having different stress levels, then the inclinations will be considerably altered. Such was not the case for these B sandstone experiments.

The major problem found in performing these direct model runs was the selection of the net pressure within the fracture. The bottom-hole pressure during the treatments was measured with a down-hole gage, but this is a value at the wellbore and ignores any near-wellbore pressure losses (perforation friction, tortuosity, etc.) and any pressure drop down the length of the fracture. If the average pressure in the fracture is lower than the wellbore value, than proportionately greater fracture heights will be required to account for the measured tilts. This difficulty may explain why the inclinometer heights were typically less than the microseismic heights (Table 11).

One other difficulty in using finite element models is the question of how to handle complex fracture geometries. For a constant height fracture with a given net pressure, the methodology for estimating the height is straightforward, as the amplitude and locations of the peak values help to constrain the fracture height. In such a way, one can actually obtain a unique fracture height value, as was done here. For non-constant-height fractures, however, there is no unique solution as there are an infinite set of variable height geometries which can provide the same general tilt field. However, the approach taken here for injection 7B (the one case with complex geometry) was not to independently determine the fracture height profile, but rather to use the microseismically

generated one and determine if it was reasonable based on the tilt data. This is the type of analysis which would be required for any case where height growth is asymmetric.

Although the tiltmeters are bi-axial devices, only the orthogonal component of the tilt field was used in these calculations. The parallel component was also examined for information about fracture length and azimuth, but these data were even more complicated than the orthogonal component and were difficult to use other than in a general sense to show consistent trends. It is suspected that other mechanisms, such as poro-elastic perturbations, fissure opening, and secondary fracture strands may have complicated the parallel components sufficiently that their smaller signals (compared to the orthogonal component) were overwhelmed by the secondary effects. No complete analysis of the parallel components has yet been made.

Finally, these results and the results of previous studies [1-3] show that inclinometers can be an extremely valuable fracture diagnostic tool. They have great sensitivity for fracture height and width and can clearly show the timing of fracture opening and growth. These downhole tiltmeters are less sensitive to fracture length, but multiple arrays or better information from the parallel component could help improve length resolution from these devices.

REFERENCES

1. Branagan, P.T., Warpinski, N.R., Engler, B.P., Wilmer, R., “Measuring the Hydraulic Fracture-Induced Deformation of Reservoir and Adjacent Rocks Employing a Deeply Buried Inclinometer Array: GRI/DOE Multi-Site Project,” SPE 36451, SPE Annual Tech. Conf. & Exhibition, Denver, CO, Oct. 6-9, 1996.
2. Warpinski, N.R., Wright, T.B., Uhl, J.E., Engler, B.P., Drozda, P.M. and Peterson, R.E., “Microseismic Monitoring of the B-Sand Hydraulic Fracture Experiment at the DOE/GRI Multi-Site Project,” SPE 36450, proceedings, 1996 SPE Annual Tech. Conf. and Exhibition, Denver, CO, October 6-9, 1996.
3. Warpinski, N.R., Branagan, P.T., Engler, B.P., Wilmer, R., and Wolhart, S.L., ¨Evaluation Of A Downhole Tiltmeter Array For Monitoring Hydraulic Fractures,” Proceedings 36th U.S. Rock Mechanics Symposium, Columbia University, New York, NY, June 29-July 2, 1997.
4. Peterson, R.E., Wolhart, S.L., Frohne, K.-H., Warpinski, N.R., Branagan, P.T. and Wright, T.B., “Fracture Diagnostics Research at the GRI/DOE Multi-Site Project: Overview of the Concept and Results,” SPE 36449, proceedings, 1996 SPE Annual Tech. Conf. and Exhibition, Denver, CO, October 6-9, 1996.
5. Northrop, D.A. and Frohne, K-H., “The Multiwell Experiment - A Field Laboratory in Tight Gas Sandstone Reservoirs, *JPT*, Vol. 42, pp. 772-779, June 1990.
6. Myal, F.R. and Frohne, K-H., “Slant-Hole Completion Test in the Piceance Basin, Colorado,” SPE 21866, Rocky Mountain Regional/Low Permeability Reservoirs Symposium, pp. 611-622, Denver, CO, April 15-17, 1991.
7. Peterson, R.E., Warpinski, N.R., Wright, T.B., Branagan, P.T. and Fix, J.E., “GRI/DOE Multi-Sites Fracture Diagnostic Project: Monitor Well No. 1 Drilling, Data Analysis and Instrumentation Emplacement,” GRI-95/0045, Gas Research Institute Topical Report, Chicago, IL, February 1995.
8. Davis, P.M. (1983). Surface deformation associated with a dipping hydrofracture. *Journal of Geophysical Research*, **88:B7**, 5826.
9. Palmer, I.D., “Uplifts and Tilts at Earth’s Surface Induced by Pressure Transients from Hydraulic Fractures,” *SPE Production Engineering*, Vol. 5, pp. 324-332, August 1990.
10. Wright, C.A. and Conant, R.A. (1995). Hydraulic fracture reorientation in primary and secondary recovery from low permeability reservoirs. SPE 30484, SPE Annual Technical Conference & Exhibition, Dallas, TX, **Π**, 357-369.
11. Westergaard, H.M., “Bearing Pressures and Cracks,” *Journal of Applied Mechanics*, Vol. 6, pp. A49-A53, June 1939.
12. Sneddon, I.N. (1946). The distribution of stress in the neighborhood of a crack in an elastic solid. *Proceedings, Royal Society of London*, **187**, 229-260.
13. Green, A.E. and Sneddon, I.N. (1950) The distribution of stress in the neighbourhood of a flat elliptical crack in an elastic solid. *Proceedings Cambridge Philosophical Society*, **46**, 159-163.
14. England, A.H. and Green, A.E. (1963). Some two-dimensional punch and crack problems in classical elasticity. *Proceedings, Cambridge Philosophical Society*, **59**, 489-500.
15. Warpinski, N.R., "Interpretation of Hydraulic Fracture Mapping Experiments," paper SPE 27985, proc., Tulsa Centennial Petroleum Engineering Symp., Tulsa, OK, Aug. 1994, 291.

16. Biffle, J.H. and Blanford, M.L., “JAC2D-A Two-Dimensional Finite Element Computer Program for the Nonlinear Quasi-Static Response of Solids with the Conjugate Gradient Method,” SAND93-1891, Sandia National Laboratories Report, May 1994.
17. Biffle, J.H., “JAC3D-A Three-Dimensional Finite Element Computer Program for the Nonlinear Quasi-Static Response of Solids with the Conjugate Gradient Method,” SAND87-1305, Sandia National Laboratories Report, February 1993.
18. Multiwell Experiment Project Group, “Multiwell Experiment Final Report: IV. The Fluvial Interval of the Mesaverde Formation,” Volumes A and B, SAND89-2612, Sandia National Laboratories Report, January 1990.
19. Lama, R.D. and Vutukuri, V.S., “Handbook on Mechanical Properties of Rocks”, Volume II, Trans Tech Publications, Clausthal Germany, pp. 195-314, 1978.
20. Aldridge, D.F. and Oldenburg, D.W., “Two-Dimensional Tomographic Inversion With Finite-Difference Traveltimes,” *Journal of Seismic Exploration*, Vol.2, pp. 257-274, June 1993.